Control and scheduling of hybrid hydropower plants with batteries for enhanced flexibility in future power systems

Stefano Cassano

PSL
UNIVERSITÉ PARIS

THÈSE DE DOCTORAT
DE L'UNIVERSITÉ PSL

Préparée à Mines Paris-PSL

Contrôle et gestion optimale des centrales hybrides hydroélectriques couplées aux batteries pour une meilleure flexibilité dans les systèmes électriques du futur

Control and scheduling of hybrid hydropower plants with batteries for enhanced flexibility in future power systems

Soutenue par

Stefano Cassano

Le 27-09-2023

École doctorale n°621

Ingénierie des Systèmes, Matériaux, Mécanique, Énergétique

Spécialité

Energétique et Génie des Procédés

Composition du jury :

João Peças LOPES Full Professor, Faculty of Engineering of University of Porto, FEUP & INESC TEC	*Président*
Seddik BACHA Professeur, Grenoble Alpes University	*Rapporteur*
Mario PAOLONE Full Professor, École Polytechnique Fédérale de Lausanne - EPFL	*Rapporteur*
Elena VAGNONI Senior Scientist, École Polytechnique Fédérale de Lausanne - EPFL	*Examinatrice*
Weijia YANG Associate Professor, Wuhan University	*Examinateur*
Fabrizio SOSSAN Associate Professor, Haute École spécialisée de Suisse occidentale - HES-SO Valais-Wallis	*Examinateur*
Georges KARINIOTAKIS Directeur de Recherche, Mines Paris - PSL	*Directeur de thèse*

MINES PARIS | PSL

Abstract

The shift from conventional generation to renewable resources challenges the electric power grid. Decommissioning conventional generation units requires identifying new flexible assets for balancing the grid and providing ancillary services. Hydropower Plants (HPPs) are important sources of electricity production and supply critical ancillary services to the grids. However, increased regulation duties to balance the intermittency of renewables (e.g., frequency control and start-stop sequences) may lead to higher wear-and-tear and maintenance costs. Hybridizing HPPs with Battery Energy Storage Systems (BESSs) has been proposed as a possible solution to increase the plants' flexibility and reduce the wear-and-tear of the hydraulic components. A key challenge of operating a hybrid HPP is to design the power set-points for the hydraulic turbine and the BESS (i.e., the power set-point splitting problem). This Ph.D. thesis proposes a formal methodology based on Model Predictive Control (MPC) for controlling hybrid HPPs that models the mechanical stress on the hydraulic components with the objective of accounting for fatigue constraints in the power set-point splitting problem explicitly. The proposed methodology includes a real-time control and a scheduling layer. In order to derive a tractable formulation of the optimization problem underlying the MPC, this thesis also develops linearized models of HPPs. The application of the proposed methodology refers to reducing penstock fatigue in medium- and high-head HPPs and can be extended to other types of HPPs and conventional generation units.

Acknowledgements

I would like to express my heartfelt gratitude to the individuals who played a pivotal role in supporting me throughout this transformative journey.

Starting with my supervisors, Georges and Fabrizio, I extend my deepest appreciation for their unwavering guidance and the wealth of knowledge they imparted. I am particularly grateful to Fabrizio for generously sharing his passion, professionalism, and, most significantly, his dedication, commitment, and honesty in the pursuit of impactful research. Our evolving friendship and mutual respect over the years have been invaluable.

My time at Center PERSEE was enriched by the incredible individuals I had the privilege of meeting. My sincere thanks go to the companions of the legendary Bureau R009b: Kevin, Valentin, Fian, and Hongxin for their friendship and the memorable moments we shared, especially at plage des ondes.

I extend my gratitude to my colleagues from neighboring offices: Akylas, Shengfei, Biswarup, Jad, Riham, Kostas, Anaelle, Owen, and Luca whose company added beauty to my journey.

To my friends from Genoa: Tullio, Fabri, Ema, Matte, Lore, Vale, Manto, Gotte who have always believed in me and that I know I can count on them no matter what. Their friendship represents for me one of the most valuable things of my life.

A special acknowledgment goes to my girlfriend, Margherita, whose support has been a constant source of strength. Our journey together has been marked by mutual enrichment and personal growth, especially during the challenging years of distance and the global impact of the COVID-19 pandemic. The moments spent together in the chalet in Biot stand out as some of the best in my life, and I owe that joy to you.

I extend my thanks to Maryse, the landlord of the house in Biot, for the enjoyable moments we shared and the discussions on various themes of life. I will miss Filae.

Finally, I express my deepest gratitude to my parents and my sister, Daniela, for their unwavering support and the unconditional love that paved the way for me to achieve my objectives.

Contents

List of Figures

List of Tables

Nomenclature

Abbreviations

BEP	Best Efficiency Point
BESS	Battery Energy Storage System
BMS	Battery Management System
CC	Correlation Coefficient
CFD	Computational Fluid Dynamic
CFL	Courant–Friedrichs–Lewy
DFIM	Doubly Fed Induction Machines
EEC	Equivalent Electric Circuit
EGD	European Green Deal
EMF	Electromotive Force
EMS	Energy Management System
EPS	Electric Power System
FSFC	Full Size Frequency Converter
GV	Guide Vane
HPP	Hydropower Plant
HPPC	Hybrid Pulse Power Characterization
HSC	Hydraulic Short Circuit
IGBT	Insulated-Gate Bipolar Transistor
IGCT	Integrated-Gate Commutated Thyristor
Li-ion	Lithium-ion
LPF	Low-Pass Filter
MAE	Mean Absolute Error
MILP	Mixed-Integer Linear Program
MOC	Method of Charateristic
MPC	Model Predictive Control
OCV	Open-Circuit Voltage
ODE	Ordinary Differential Equation

PDE	Partial Derivative Equation
PFC	Primary Frequency Control
PI	Proportional Integral
PID	Proportional Integral Derivative
PRBS	Pseudo-Random-Binary-Signal
PSPP	Pumped Storage Power Plant
RDI	Relative Damage Index
RES	Renewable Energy Source
RoR	Run-of-River
SG	Synchronous Generator
SOC	State-Of-Charge
SOH	State-Of-Health
TTC	Two-Time-Constant
VLEO	Voltage-Limited Extrapolation
VLOR	Voltage-Limited Ohmic Resistance

Chapter 1

Introduction

1.1 Context

Decarbonizing energy production presents a major challenge for the European power grid in the coming years. The European Green Deal (EGD) establishes the objective of becoming climate neutral in 2050 [1]. This objective requires a reduction of greenhouse gases of 55% by 2030. To achieve this reduction, the current EU target of Renewable Energy Sources (RESs) share has been set to 45% in its communication on the Renewable Energy Directive, which would bring the total renewable energy generation capacities to 1236 GW by 2030 [2].

The integration of an increased proportion of RESs may hinder the future development and operations of the European Electric Power System (EPS). The intermittent and uncertain nature of RESs limits the provision of reliable and controllable electricity, thereby affecting the balance between supply and demand. Moreover, large-scale RES integrated system faces extremely low inertia due to the connection of the RESs through power electronic interfaces, resulting in a negative impact on the frequency stability.

Typically, dispatchable plants (e.g., thermal, nuclear and hydropower plants) are key for the grid stability. They are equipped with a synchronous rotating machine directly connected to the grid that is controllable in terms of output power and is capable of providing a suite of services to the power grid, such as inertia and power balancing. In addition, they are also responsible for the majority of grid ancillary services. Recent transformations of the European EPS consists of disconnecting and decommissioning traditional generating units, namely fossil fuel-fired power plants, as greenhouse gases emitters, accounting, in 2020, for about 36% of the European electricity share [3].

As the number of dispatchable plants decreases in favor of integrating RESs, it is crucial to enhance the flexibility of the EPS. In this context, the flexibility is defined as the ability of the power system to modify generation and consumption in response to expected and unexpected variability due to RES generation and forecast errors [4, 5]. This need has been recognized at the level of the European Union and supported in recent years by extensive research efforts aimed at investigating and enhancing the flexibility of future power systems, as, e.g., the research projects EU-SysFlex and OSMOSE [6, 7]. EU-SysFlex project [6] is an H2020 EU-funded project started in

2017 with the goal of identifying the technical lacks in the future power system with high penetration of renewables and providing a mix of flexibility and system services to support secure and reliable operations. The OSMOSE project [7], started in 2018, it is a H2020 EU-funded project aiming at increasing the techno-economic potential of a wide range of flexibility solutions, which can be used for a better integration of RES. The project proposes four TSO-led demonstrations (RTE, REE, TERNA and ELES) addressing different flexibility solutions and services such as: synchronisation of large power systems by multiservice hybrid storage, new hybrid and modular storage solution for multiple system services, cross-border sharing of flexibility sources and smart energy management system.

In summary, research efforts have pointed out the need to investigate new and effective methods to be incorporated into state-of-the-art technologies and optimize the use of resources. Among those, enhancing the EPS flexibility through more flexible power generation assets has a critical role. This thesis will focus on hydropower technology and, in particular, on a promising way to extend the flexibility of Hydropower Plants (HPPs): *Hybridization*. Before discussing it, the remaining part of this Section examines the current and future role of hydropower plants in sustaining the EPS.

1.1.1 The role of hydropower

In 2020, hydropower accounted for about 36% of the EU's total renewable capacity and provided 17% of the total power generation [8]. Hydropower is the leading renewable energy source in Europe, with 660 TWh generated across the continent this year. The total installed capacity is approximately 320 GW, of which 18% is pumped storage capacity [8]. While about half of Europe's hydropower potential has already been developed, some potential remains in certain countries. The forecast predicts an 8% increase in Europe's hydropower installed generation capacity (+18 GW) between 2021 and 2030 [9].

As illustrated in Fig. 1.1, hydropower plants are of several types according to the arrangement, gross head and capacity. Generally, we can identify three basic configurations:

- **Run-of-river (RoR) plants** harvest the energy from the natural flow rate of rivers to generate electricity. Typically, they have little or no storage facility, providing continuous electricity supply (base load) with some flexibility of operation for daily fluctuations in demand through water flow that the facility regulates. They are also referred to as "low-head HPPs", with typical capacity ranging from a few kW up to 25 MW.

- **Storage plants** are large plants that use a dam to store water in a reservoir. Electricity is produced by releasing water from the reservoir through a turbine, which activates the electric generator. Storage HPPs can provide both base and peak loads thanks to the ability to be shut down and started up at short notice to match power demand. This category includes medium- and high-head HPPs with a power capacity larger than 25 MW.

- **Pumped Storage Power Plants (PSPPs)** provide peak-load supply, harnessing water that is cycled between a lower and upper reservoir by pumps that use surplus energy from

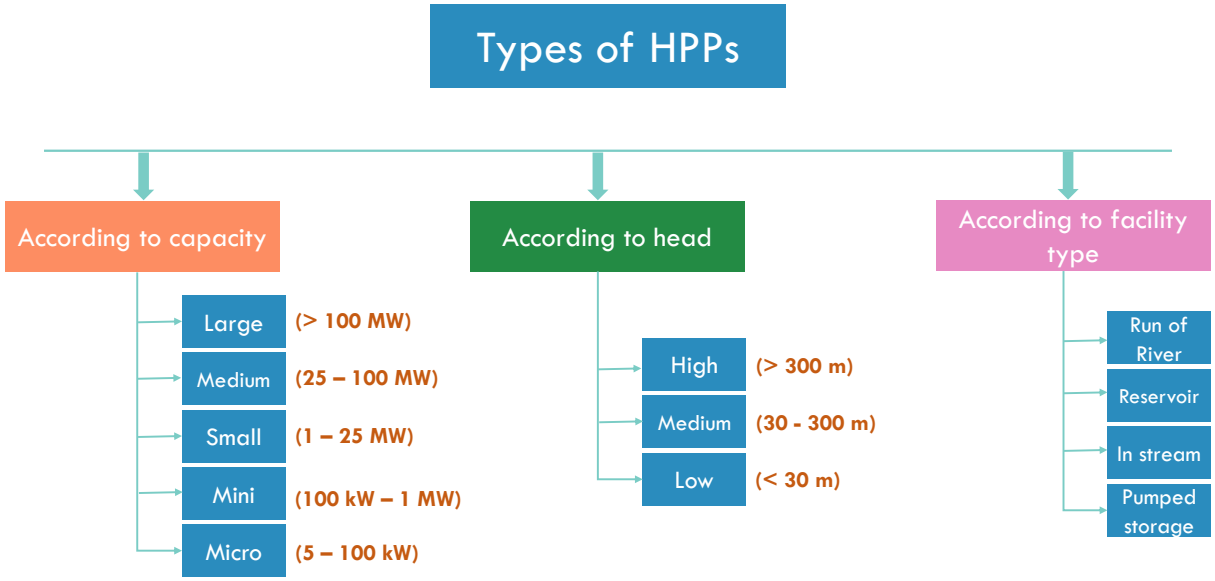

Figure 1.1: Hydropower plants classification.

the system during low-demand periods. During high-demand periods, water is released back to the lower reservoir through turbines to generate electricity.

HPPs play a crucial role in the EPS providing essential electricity generation and regulation services. As a controllable renewable energy source, HPPs can accommodate future challenges of the energy transition as they are very flexible and one of the few technologies capable of operating at all time scales. Some of the fundamental services provided by HPPs are:

- **Frequency regulation**. It consists of continuously balancing the frequency fluctuation in the grid with active power compensation. Participating in frequency regulation requires fulfilling specific tests (e.g., the ENTSOE pre-qualification tests [10]). HPPs have large ramping rates (around 15-20% nominal power per minute), making them eligible for this service.

- **Quick start capability**. Thanks to the lack of thermal constants, HPPs provide fast start-and-stop transitions within a few seconds. This capability is of great importance to manage peak demand periods and compensating for power fluctuations from variable sources. In addition, the quick start capability contributes to maintain the grid stability.

- **Black starting.** HPPs can black starting quickly and provide sufficient power to energize the transmission system during a widespread grid outage. The significant inertia of hydro generators and high ramping rates helps to stabilize the system frequency.

- **Spinning reserve**. HPPs contributes to the spinning reserve due to their online connection with rotating synchronous generators.

- **Reserve capacity and dispatch**. Especially PSPPs can provide reserve capacity for bottleneck situations and longer imbalances. Moreover, they can dispatch by adjusting their output power (in a positive or negative direction) to avoid grid congestion.
- **Voltage control**. HPPs can control reactive power by ensuring reactive power flow. This means voltage control is achieved by absorbing energy and releasing it back into the grid.

1.1.2 Future challenges for hydropower

The hydropower industry is facing new challenges in enhancing the flexibility of the EPS. Indeed, integrating a larger proportion of stochastic renewable generation will increase the need for regulation for conventional generation. These future flexibility requirements may lead to more frequent changes of power set-point that generate high levels of wear-and-tear of the mechanical components, ultimately leading to reduced operational efficiency due to higher maintenance costs and reduced plant availability [11]. HPP operators are particularly concerned with transient operations, such as startup, shutdown, load acceptance and rejection, and frequency regulation (primary, secondary, and tertiary). Typically, hydraulic turbines operate around their Best Efficiency Point (BEP) under a steady-state. Transient phenomena result from a change in the operating conditions of the system. Next, we discuss three examples of operations that might engender wear-and-tear in HPPs.

The first example are emergency shutdowns that represent a critical case for HPPs due to the maximum and minimum pressure induced in the piping system. Such situations can be caused by large frequency oscillations of the power grid or power lines failures. Fig. 1.2 shows a simulated emergency shutdown of a hydropower plant equipped with a Francis pump-turbine. The electromagnetic torque from the fully open guide vane is set to zero at t=10 s. At this point, the guide vane is closing and the turbine experiences a runaway speed while the torque and the discharge go to zero due to the guide vane closing. During the runaway, the operating point of the turbine goes from normal operation to the turbine brake (around 15 s, when the turbine has negative torque and positive speed). Sometimes the operating point can reach the reverse pumping mode. The sudden excursion from normal turbine operation leads to a large and fast discharge variation. It thus generates a high positive pressure wave in the enclosed conduit (i.e., penstock), known as *water hammer* effect, and a negative pressure wave in the draft tube that may create vortex ropes and cavitation, resulting in structural vibrations and overpressures [12, 13].

The second example is the load rejection and acceptance which refer to sudden load variations in the system that cause the generating equipment to be over or under frequency. The guide vanes opening regulates the hydraulic torque, limiting the turbine's rotational speed. This may induce water hammers and vortex formation leading to vibrations, unsteady pressure pulsation, and induced periodic oscillations, resulting in variation in output power [14].

The third example is frequency regulation where large changes in the guide vane opening may cause water hammer and pressure transients along the penstock that, due to fatigue limitations, might over-burden the piping system [15].

Currently, research on wear-and-tear in hydroelectric plants is predominantly focused on hydraulic turbines [16]. The main objective is to determine the optimal hydraulic layout of power plants and identify the most advantageous trajectories for the machines in order to reduce hydraulic

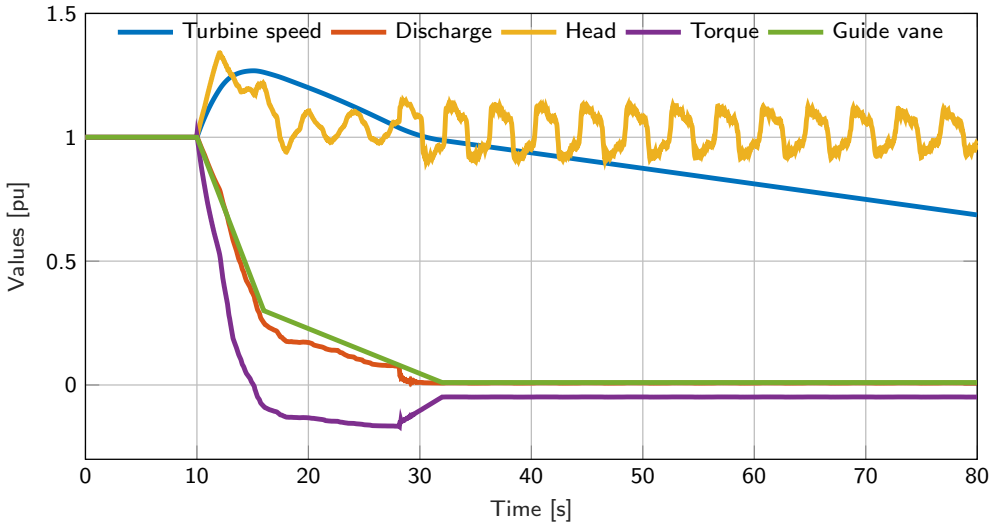

Figure 1.2: Emergency shutdown: heads, discharges and mechanical torques resulting from the loss of the electromagnetic torque in t=10 s and the corresponding guide vane closing by a bi-linear closure law.

transients. Typically, observations and computations on reduced-scale models are carried out to evaluate the performance of the hydraulic machines and the occurrence of hydraulic transients. For instance, the study of cavitation in hydraulic turbines involves performing tests on the reduced-scale model and taking measurements on real plants to identify the stable and "forbidden zones" in which to operate the turbine safely.

In contrast, there has been a paucity of research investigating other components that may emerge as critical for future operations. Specifically, limited attention has been given to stresses resulting from transient pressure waves caused by water hammers, which are less obvious than mechanical stresses arising from rotating torque [16]. In this context, maximum overpressures are constrained by setting limitations based on static loads. Notably, most hydropower plants in Europe were built between 1950 and 1980 and designed according to the maximal static pressure limit based on the system layout and hydraulic machine types. Given that these plants are aging and cannot support new operating conditions without modernization, there is a need for novel technological solutions and further research into fatigue reduction to ensure reliable plant operation and the continuity of the energy production system. The next section outlines some of these potential solutions.

1.1.3 Technologies for extending hydropower plants' flexibility

Current research on hydropower focuses on developing technologies capable of enhancing flexibility services, optimizing maintenance schedules, increasing availability, and maximizing their performance. At the European level, the XFLEX Hydro project [17] seeks to demonstrate novel technological solutions for hydropower plants that can significantly enhance the flexibility of the electric power system and improve the overall efficiency of hydroelectric machinery, leading to high availability and maximized performance.

Hardware upgrades to increase the flexibility of HPPs include: (i) implementing new technological solutions, (ii) installing sensory equipment and, (iii) developing advanced control. The latter treats data from sensors and makes informed decisions to extend the plant efficiency and reduce the need for maintenance by monitoring the wear-and-tear of critical components.

Concerning the technological solutions, the most promising are: variable speed technology, Hydraulic Short Circuit (HSC), and hybridization with Battery Energy Storage Systems (BESSs).

Variable speed refers to decoupling the speed of the turbine rotor from the grid frequency. By doing so, the operating range of the hydraulic machine is expanded, resulting in increased flexibility and efficiency. As mentioned in the previous section, hydraulic machines operate around their BEP under steady-state, which corresponds to the operating point that ensures the highest efficiency for rated working conditions. These are according to hydraulic and mechanical quantities such as the head (i.e., the pressure), the discharge, the rotational speed of the runner and the guide vane opening. The main advantage of variable speed technology is that it enables the machine to operate at conditions other than the rated ones while maintaining the rated efficiency [18]. In run-of-river HPPs, variable speed technology is particularly interesting due to the low head conditions that are often encountered. This is especially relevant in light of concerns regarding climate change and its potential impact on water levels in rivers. In such scenarios, the ability to operate at lower heads while maintaining rated efficiency is achieved by operating the machine at a lower speed, which is not possible in fixed speed units due to the need to maintain a fixed synchronous machine speed of 50 Hz for stable operation. In pumped-storage plants equipped with Francis pump–turbines, the benefit of variable speed is that a single hydraulic machine can operate in both pump and turbine mode at maximum efficiency. The reason for this is that Francis pump-turbines are typically designed as pumps, with optimal speeds higher than those for turbine mode [19].

Varying speed is enable by power converters employing power electronics to decouple the motor/generator from the grid in terms of reactive power, voltage and frequency. There are two primary types of variable speed technology currently available:

- Full Size Frequency Converter (FSFC) feeding the synchronous machine [20, 21]: the stator of the conventional synchronous machine is connected to the power network through a frequency converter offering a full flexibility for the rotating speed. However, the rated power of the converter is 100% of the motor-generator power, making it most suitable for relatively low power applications due to its high cost [22].

- Doubly Fed Induction Machines (DFIM)[23, 24]: the AC current is fed to the rotor of the asynchronous motor-generator through a frequency converter enabling a unit rotational speed variation of typically +/- 10%. The rated power of the frequency converter in this configuration is only 10% of the rated motor-generator power [22]. Voltage source inverters using IGBT (Insulated-Gate Bipolar Transistor) or IGCT (Integrated-Gate Commutated Thyristor) are used as frequency converter to enable fast response.

Hydraulic short circuit is a technique used to regulate the pumps in pumped storage power plants, which offers the primary advantage of extending the plants' regulating range. Typically, Pelton and Francis units are installed in pumped storage power plants. The turbines can vary their

output from full load down to part load, typically from 50 to 100% for Francis turbines and from 10 to 100% for Pelton turbines. On the other hand, the pumps operate at a fixed speed and a given head. As a result, their input power is fixed, and they can only operate if the grid provides the required input power. During HSC, both the turbines and pumps operate simultaneously, and a part of the pump flow may pass through the turbine and into the upper reservoir. The net power consumption from the grid is the difference between the pump input and turbine output power.

Hydraulic short circuit significantly extends the regulation range from 100% production down to maximum pump consumption by utilizing different setups of pumps and turbines in operation, thereby allowing the best overall efficiency of the plant. Hydraulic short-circuit operations offer potential benefits such as frequency regulation, thanks to the fast response of hydraulic turbines, and grid balancing, owing to the flexible control of production and consumption.

Hybridization forms a central theme of the this thesis, and as such, it is the focus of the next section.

1.2 Hybrid hydropower plants

Hybridization refers to adding a battery energy storage system in parallel with the electrical generator to increase the flexibility of the power plant. By injecting power into the system, the battery is expected to mitigate transient operations and reduce the mechanical stress on plant components.

The first part of this section discusses the motivation and objectives of hybridization. The second part describes the conventional plant regulator and points out the challenges of integrating the hybridization technology from a control perspective.

1.2.1 Battery energy storage systems and hybridization of hydropower plants

Battery energy storage systems are becoming of great interest for power grid applications. In particular, BESSs play an essential role in integrating the stochastic renewable sources, as they absorb excess energy during periods of high production and release it during periods of low production.

In the literature, BESS services have been grouped into three categories [25]:

1. provision of ancillary services (e.g., primary and secondary frequency regulation);
2. local objectives for the grid (e.g., voltage regulation, peak-shaving, congestion management, PV self-consumption);
3. energy arbitrage, which involves exploiting price differences by buying energy at a low price and selling it back to the grid at a higher price.

To allow the best exploitation of the battery from both an economical and technical point of view, control strategies able to provide simultaneously more than one of the services listed above have been widely proposed in the literature [26–32]. The reason for multiple service provisions is that the BESS energy capacity could remain unexploited when deploying a certain service due to the uncertainty of the stochastic resources to which BESSs are coupled. Therefore, the remaining energy can be used for a secondary service. In this sense, one important aspect is that different services

have different energy and power requirements. For instance, peak-shaving or energy arbitrage are *energy-intensive* applications that require a large amount of energy but low instantaneous power, whereas Primary Frequency Control (PFC) is a *power-intensive* service, that necessitates high levels of power but not a large amount of energy.

In recent years, Lithium-ion (Li-ion) batteries have substantially improved thanks to better electrochemistry, refined production processes, and lower costs [33, 34]. Li-ion batteries have technical and practical advantages over traditional lead-acid batteries due to their very high energy density resulting in the capacity to store more energy in less space. Moreover, the decreasing costs of Li-ion technology have accelerated its adoption in various applications.

A relatively new solution involves combining conventional power plants with a grid-connected BESS to leverage the mutual characteristics of the two units. For instance, batteries have very fast ramping rates but limited energy capacity, while conventional plants have slower responses but more available energy. The objective of this solution is to take advantage of these characteristics to optimize the performance and efficiency of the power grid.

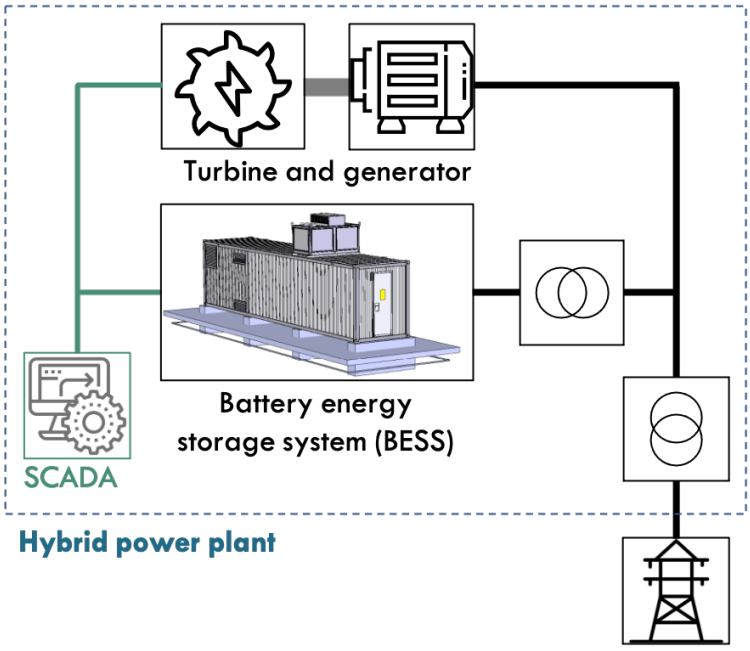

Figure 1.3: Schematic of a hybrid hydropower plant.

In the case of hydropower, the advantage of hybridization is sustaining the enhanced fast control requirements for balancing the future electric grid. Increasing the frequency regulation has a critical impact on the wear-and-tear of the mechanical components of the HPP [35]. Recent studies [16, 36] have highlighted that in medium- and high-head HPPs, the concern is the hydraulic pressurized conduit that feeds water to the turbine, the so-called *penstock*. Indeed, sudden variations of the guide vane due to changing the plant's power output result in abrupt changes in the water pressure that reflects back and forth in the penstock (water hammer effect). This phenomenon leads to increased mechanical stress on the penstock wall, damaging it in the long run due to fatigue [37]. In low-head HPPs, which are generally equipped with double-regulated Kaplan turbines, the wear-

and-tear concerns are mainly associated with the actuating mechanisms of the guide vane, which regulates the amount of water flowing to the turbine, and the Kaplan turbine's blades, which adjusts the efficiency [38, 39].

Hybridization has, therefore, two main operational **objectives**:

1. extending the overall regulation capacity of the system; and
2. reducing wear-and-tear thanks to avoiding operational patterns conducive to large levels of mechanical stress for the HPP component.

This results in increased lifetime and improved availability of the HPP, with less outage time due to maintenance. While from the BESS perspective, the hydropower unit can support the battery to operate continuously.

Fig. 1.3 shows the layout of a hybrid HPP. The battery is connected to a step-up transformer and coupled in parallel with the synchronous machine of the hydro unit. The advantage of installing a BESS at the plant location instead of elsewhere is of being connected to the local SCADA system, thus enabling the use of real-time measurements from the plant for more informed decision-making and better dynamic performance.

1.2.2 Conventional and hybrid controller

Fig. 1.4 shows the block diagram of a traditional control system for HPP. It includes a Proportional Integral Derivative (PID) speed governor with permanent speed droop for primary control and a power control loop enabling secondary control. The feedback loop on the rotor speed, denoted by ω_r, implements a frequency droop controller, where R is the droop coefficient, whose task is keeping the rotational speed of the machine near a design value, denoted by ω_0.

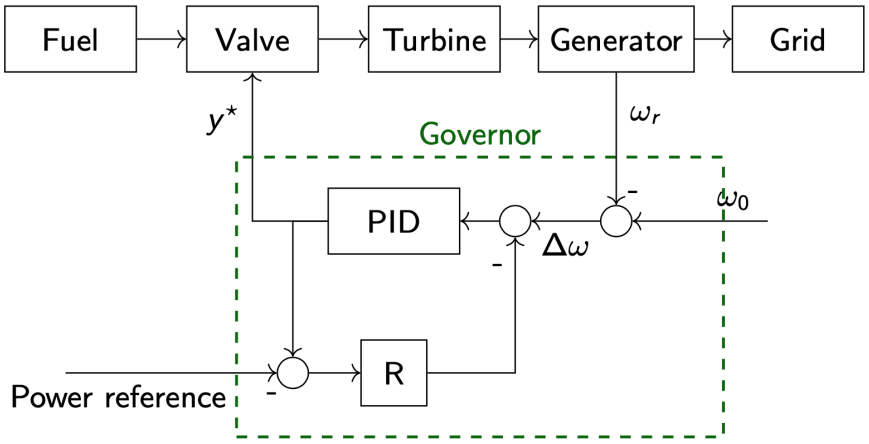

Figure 1.4: Standard regulation loop of a HPP.

The permanent speed droop conventionally adopted for HPPs is in the range of 2.5-5% [40]. The PID controller computes the position of the so-called guide vane, denoted by $y^\star$, which adjusts the flow of water to the turbine. The PID controller's parameters, which also include a ramp limiter, actuators' dynamics, and saturation limits, not shown here for compactness, are selected to fulfill

the response time requirements for grid frequency regulation. The input signal *Power reference* represents the speed changer setting that the operator uses to change the plant power set-point for, e.g., secondary frequency regulation set-points, rescheduling, etc. The guide vane computed by the governor $y^\star$ is tuned to respect the static design limits of the plant. To participate in regulation services, the controller's dynamic performance must comply with the frequency control qualification test [41, 42] (primary and secondary frequency control tests are described in Appendix A).

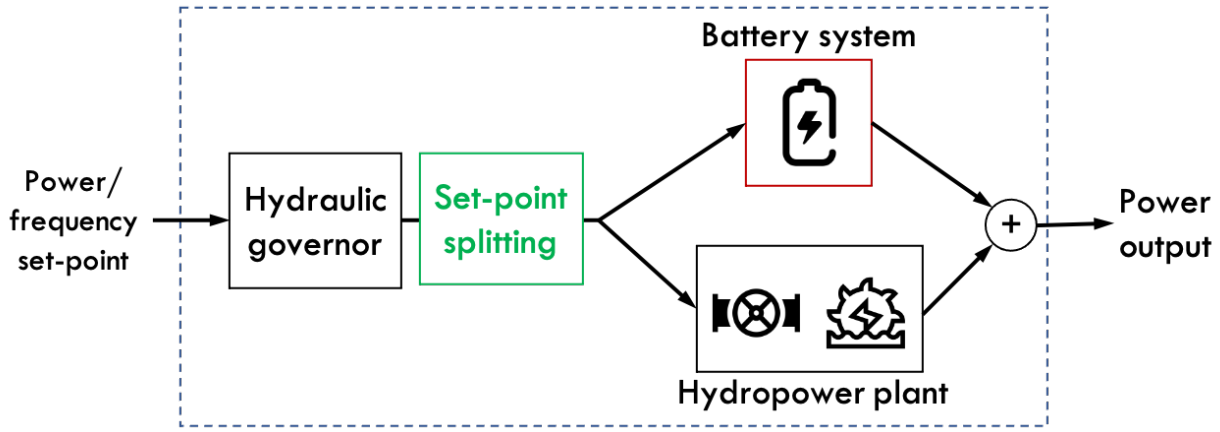

Figure 1.5: Control scheme of a hybrid hydropower plant.

While in a HPP the controllable element is generally one (i.e., the guide vane of the plant), in a hybrid HPP the operator has the problem of determining two set points: one for the HPP and one for the battery, as illustrated in Fig. 1.5. We call this the *power set-point splitting* problem, or *splitting* problem. More specifically, the controller, represented by the green box in Fig. 1.5, has to determine a new set-point that satisfies two crucial requirements:

1. it should not result in mechanical loads engendering fatigue;

2. it should preserve the original regulation duties of the plant and avoid excess curtailment of the regulation duties, which could result in economic penalties or disqualification from regulation services.

To the best of the author's knowledge, no prior research has attempted to tackle the control problem of a hybrid HPP. The closest related work is presented in [43], which focuses on modelling the combined system of a BESS and a hydropower plant to examine its capability to fulfill the PFC pre-qualification test.

1.3 State-of-the-art of hydropower fatigue reduction controllers

Designing a controller for hybrid HPPs is a relatively new research problem, which has been addressed in the literature with empirical models. Many of the proposed strategies tackle the problem of wear-and-tear reduction by diminishing (i) the distance of Guide Vane (GV) movement and (ii) the total number of movement direction changes. The movement distance impacts the wear of the

bearings of the GV servo mechanism [35, 44], while direction changes can lead to load cycles on the turbine runner, potentially increasing fatigue on the mechanical component of the turbine's servo motor [14, 45]. During GV movements, servomotor forces must overcome the hydraulic and friction torque, which act in opposite directions depending on whether the GVs are opened or closed. In Kaplan turbines, blade movements may also cause failures of the runner servo mechanism, thereby posing additional wear-and-tear concerns [39, 46]. In this section, we present the theoretical background of two state-of-the-art methods to reduce wear-and-tear: low-pass and dead-zone filters.

1.3.1 Low-pass filters

A commonly proposed approach for reducing fatigue in mechanical components is to employ low-pass filters on the frequency set-point and transmit the filtered signal to the governor for actuation. However, this method is grounded on two underlying assumptions: first, that high-frequency variations of the power set-point are the primary cause of mechanical component fatigue; and second, that a formal procedure exists for translating fatigue requirements into the cut-off frequency of the filter. These assumptions are hard to justify and realize in practice [47]. A potential solution for determining the appropriate cut-off frequency to mitigate pressure transients on the penstock during frequency regulation is presented in [48]. In this method, the natural frequencies of the penstock are identified by applying a Pseudo-Random-Binary-Signal (PRBS) to a detailed plant simulation model. The transfer function obtained between the frequency set-point and the pressure at the penstock end displays several critical frequencies corresponding to the penstock modes. The first natural frequency of the penstock produces maximum pressure amplitudes at the penstock end by disregarding pressure fluctuations resulting from the mass oscillation period between the surge tank and the upper reservoir [49].

The analytical determination of the first natural frequency of a penstock, represented by f_0, can be expressed by the equation:

$$f_0 = \frac{a}{4L}, \tag{1.1}$$

where a denotes the average wave speed in the penstock, and L corresponds to the length of the aforementioned component. The resulting frequency f_0 serves as the cut-off frequency of the low-pass filter.

1.3.2 Dead-zone frequency filter

Dead-zone (or dead-band) filters are widely used in hydropower plants for PFC [50]. The fundamental idea behind the dead-zone concept is to filter out frequency fluctuations that fall below a certain threshold to prevent minor movements of the governor GV from causing wear-and-tear. Typically, the frequency fluctuations in the power grid are predominantly below 0.1 Hz and can cause significant GV movements with small amplitudes [35, 44]. These small GV movements can lead to output power fluctuations and induce vibrations in the plant. The selection of the dead band represents a compromise between reducing wear-and-tear and maintaining effective regulation. The working principle of the filter is expressed by the following equation [51] and represented

in Fig. 1.6:

$$\Delta\omega = \begin{cases} 0 & -z \leq \omega_r - \omega_0 \leq z \\ \omega_r - \omega_0 - z & \omega_r - \omega_0 > z \\ \omega_r - \omega_0 + z & \omega_r - \omega_0 < -z \end{cases} \tag{1.2}$$

where ω_r and ω_0 are the rotor and grid frequencies, respectively, and $(-z, z)$ is the frequency dead band.

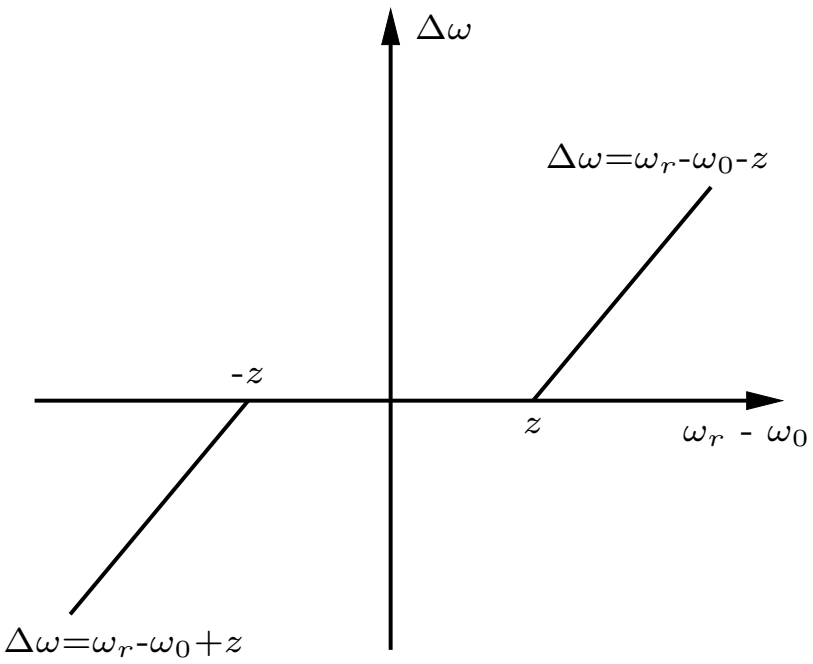

Figure 1.6: The frequency band of the dead-zone filter.

As per Eq. (1.2) and Fig. 1.6, three distinct zones are evident. In the first zone, the difference between the rotor and grid frequency remains within the frequency dead band. This zone is characterized by an output of the filter $\Delta\omega$, which equals zero. In the second zone, the difference $\omega_r - \omega_0$ exceeds the upper bound of the dead band, z. Consequently, the filter output becomes the difference between the rotor and grid frequency, reduced by z. Finally, in the third zone, when the difference between rotor and grid frequency is lower than the dead band's lower bound, $-z$, the output is the frequency difference plus z. The output of the filter, $\Delta\omega$, is utilized as the input of the hydraulic governor's PID, shown in Fig. 1.4.

In [52], the authors present a comparison of the performance of the low-pass filter and the dead-zone filter with regards to wear reduction and frequency quality. The low-pass filter outperforms the dead-zone filter in terms of frequency quality and simultaneously reduces the distance and magnitude of GV movement. However, the use of the low-pass filter may result in system instability.

On the other hand, the dead-zone filter effectively reduces the distance of GV movement but exhibits the worst frequency quality of the two filters. Moreover, the dead-zone filter is not particularly effective in reducing the amount of GV movements.

In summary, current controllers for hybrid HPPs adopt oversimplified wear process models, which often result in conservative or incorrect fatigue level estimates and excessive BESS utilization. This thesis aims to address this gap by introducing an explicit fatigue model into the control process, as elaborated in the subsequent section.

1.4 Challenges and contributions

The development of an effective controller for hybrid power plants require to satisfy the operational requirements of both the battery and HPP, while minimizing the fatigue on the critical components. Plant operators are often concerned about the wear-and-tear phenomena on the mechanical components of the plant, leading to overly cautious decisions about the regulation to provide, potentially resulting in reduced grid support and profits from electricity regulation markets. The hybrid controller aims to determine feasible control trajectories for the BESS and hydropower unit to improve the dynamic response of the hybrid plant.

The existing controllers are not adequate as they are configured to ensure that the plant operates within nominal limits, without providing any explicit mechanisms to model and reduce mechanical loads' long-term impact on fatigue.

This thesis targets medium- and high-head HPPs. In such plants, increased provision of primary and secondary frequency regulation can increase penstock fatigue by a factor of 10 [16]. This can have significant implications for the penstock's service life, the critical component of the plant. The manuscript aims to address three primary challenges.

Challenge 1: Tractable modelling of medium-head HPPs. The first challenge of this work is to develop linear models that accurately describe the hydraulic quantities involved in the hydropower plant. These models will be used in a Model Predictive Control (MPC) framework to explicitly model hydraulic components' mechanical stress and formulate constraints for fatigue reduction. This approach stems as an alternative to existing control approaches, which do not account for fatigue in the control problem explicitly. The advantages of using linear models are related to achieving a convex (and tractable, e.g., in terms of computation speed for real-time implementation) formulation of the MPC's optimization problem.

Challenge 2: Designing a real-time control for hybrid medium-head HPPs to reduce penstock fatigue. The second challenge is to design a real-time control strategy that can effectively adjust the set-point of the HPP in order to limit the fatigue on the critical component of the plant while determining the optimal set-point for the battery to provide the required regulation. This control strategy should ensure fast computation of the set-point to meet the real-time requirements.

Challenge 3: Scheduling the BESS operations for fatigue reduction service. The third challenge focuses on the development of a scheduling strategy for BESS operations that targets fatigue reduction service in hybrid medium-head HPPs. The scheduler, acting as the high-level controller, is responsible for managing the BESS's charging and discharging operations to ensure sufficient energy reserves for providing the required service. The scheduler takes inputs such as the current State-Of-Charge (SOC) of the BESS and forecasts to predict the power and

energy needed for regulation over subsequent periods. However, conventional energy scheduling techniques have been shown to have limited effectiveness in reducing fatigue as the BESS operates in a power-intensive mode for the subscribed service.

The thesis presents several significant contributions, which are summarized as follows:

C.1. derivation and validation of reduced-order models for model-based control strategies. Specifically, the work proposes linear models of the HPP using the electrical analogy and validates them using real measurements (as presented in Appendix A). The development of these models is critical for formulating linear control strategies based on convex optimization;

C.2. development of an MPC framework for fatigue reduction. While MPC is a widely used controller in industrial processes, this thesis presents an original approach by formulating a control problem that incorporates stress constraints of the mechanical components of HPPs and battery power computation. This contribution provides a significant contribution to the field of MPC, as it represents an innovative and applicable solution to a relevant control problem;

C.3. formulation of a scheduler for power-intensive application. While schedulers based on convex optimization have been studied for various applications and at different levels of system complexity, this thesis offers a significant contribution by incorporating SOC-dependant power constraints in the optimization problem formulation. This contribution is particularly relevant given the power-intensive nature of the fatigue reduction service, and it provides an innovative and applicable solution to a relevant optimization problem.

1.5 Structure of this thesis

This section outlines the structure of the thesis, providing a brief overview of each chapter. The first chapter has presented a comprehensive overview of the role, challenges, and current research in the field of hydropower technology. The primary focus of this thesis is on hybrid HPPs, and specifically, on optimizing the control of the plant and battery to enhance flexibility and availability while reducing fatigue on mechanical components. A research gap in the existing controllers for HPPs has been identified, namely, the poor approximations and oversimplification of the wearing process due to the lack of explicit modelling of the mechanical loads and fatigue on components. To address this research gap, three challenges have been identified, and the following chapters aim to tackle them.

Chapter 2 deals with Challenge 1 by developing linear models to estimate the mechanical loads on the penstock and the power production of the hydro unit.

Chapter 3 addresses Challenge 2. The MPC is presented and compared to benchmark controllers to evaluate its performance.

Chapter 4 focuses on Challenge 3, showing the design of a scheduler for power-intensive applications.

Finally, Chapter 5 provides concluding remarks along with a summary of the results, thesis contributions, and future perspectives.

Each chapter concludes with a summary in French.

Fig. 1.7 provides an overview of the thesis structure, challenges, and contributions.

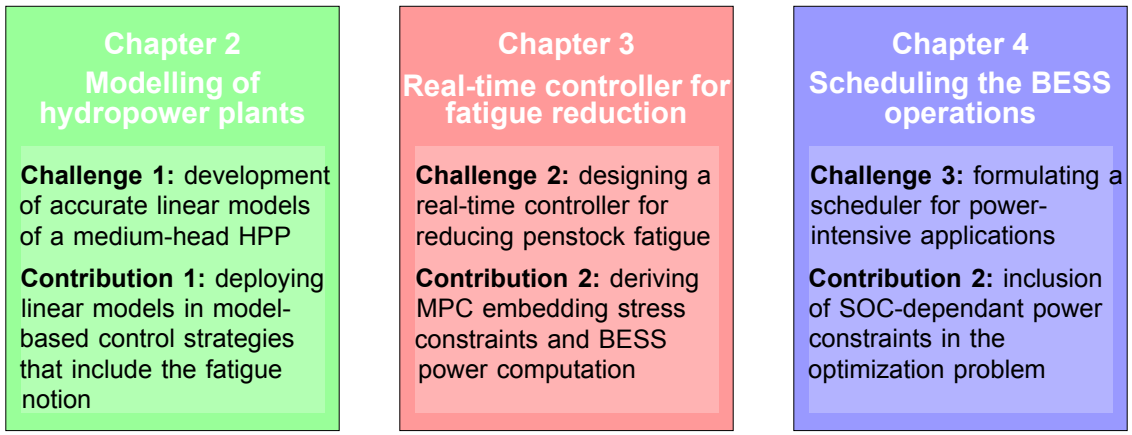

Figure 1.7: Overview of the structure of the thesis, challenges and contributions.

1.6 List of publications

The present thesis led to the following publications:

Peer-reviewed journals:

1. **S. Cassano** and F. Sossan, *"Stress-informed control of medium- and high-head hydropower plants to reduce penstock fatigue,"* Sustainable Energy, Grids and Networks, vol. 31, p. 100688, 2022., https://doi.org/10.1016/j.segan.2022.100688 https://hal.archives-ouvertes.fr/hal-03782709v1

2. **S. Cassano** and F. Sossan, *"Model predictive control for a medium-head hydropower plant hybridized with battery energy storage to reduce penstock fatigue,"* Electric Power Systems Research, vol. 213, p. 108545, 2022, https://doi.org/10.1016/j.epsr.2022.108545 https://hal.archives-ouvertes.fr/hal-03782724

3. **S. Cassano** and F. Sossan, *"Scheduling BESS operations for power-intensive applications: the case of fatigue reduction in medium-head hybrid hydropower plants,"*. Journal paper in preparation.

International conferences:

1. **S. Cassano**, C. Laundry, C. Nicolet, F. Sossan, *"Performance Assessment of Linear Models of Hydropower Plants,"* 2021 IEEE PES Innovative Smart Grid Technologies Europe (ISGT Europe), 2021, pp. 01-06, 10.1109/ISGTEurope52324.2021.9639912 https://hal.archives-ouvertes.fr/hal-03511960/

2. **S. Cassano**, C. Nicolet, F. Sossan, *"Reduction of Penstock Fatigue in a Medium-Head Hydropower Plant Providing Primary Frequency Control"*. 2020 55th International Universities Power Engineering Conference (UPEC), 2020, pp. 1-6, 10.1109/UPEC49904.2020.9209857 https://hal.archives-ouvertes.fr/hal-02956055/document

Chapter 2

Modelling of Hydropower plants

This chapter develops and validates linear models of HPPs for application to the MPC described in the following chapters. It discusses 1-D models for a medium-head HPP with a Francis turbine and a low-head RoR with a Kaplan turbine, where the hydraulic and electric components are combined using an Equivalent Electric Circuit (EEC). The chapter addresses the non-linearities of the models and presents linearization techniques for deriving linear models of the HPPs. Finally, it concludes with an evaluation of the performance of the proposed linear models in estimating the head along the penstock and the torque of the turbine. In the following of this thesis, these two quantities will be used to estimate the mechanical stress on the penstock and the power output of the HPPs.

2.1 Résumé en français

Ce chapitre se concentre sur la modélisation, le développement et la validation de modèles linéaires de centrales hydroélectriques dans le contexte de la prise de décisions basée sur des modèles. Les centrales hydroélectriques convertissent l'énergie potentielle et cinétique de l'eau en énergie électrique, avec des composants hydrauliques et électriques. Les machines hydrauliques, classées en machines à réaction et à impulsions, jouent un rôle clé. Le chapitre se divise en trois sections principales: les approches de modélisation appropriées, le développement de modèles non linéaires des composants hydrauliques et électriques, et enfin, la proposition de techniques de linéarisation pour faciliter la mise en œuvre de contrôles efficaces. Des modèles non linéaires de HPPs, notamment une centrale à chute moyenne et une centrale au fil de l'eau, sont présentés et validés. Les modèles linéaires sont introduits comme alternative plus pratique pour la mise en œuvre du contrôle prédictif basé sur l'optimisation convexe, avec des performances évaluées par rapport aux modèles non linéaires. En conclusion, le chapitre offre une contribution originale avec la proposition de modèles linéarisés, offrant une alternative plus gérable pour le contrôle des centrales hydroélectriques.

2.2 Introduction

Hydropower plants convert the potential and kinetic energy of the water into electrical energy. Regardless of the type of hydropower plant, the water starts to flow due to its potential energy.

This potential energy is converted into kinetic energy, which drives the turbine runner and is transformed into mechanical energy. Finally, an electrical generator connected to the turbine shaft produces electricity. The schematic representation of a typical hydropower plant with a dam is depicted in Fig. 2.1. The plant can be categorized into two parts from a modelling standpoint: the hydraulic and electrical parts. The hydraulic part comprehends the hydraulic circuits and machines. The hydraulic circuits are generally composed by these components:

- upstream and downstream reservoirs where the water is stored;
- hydraulic conduits to transport water. These are the water intake, tunnels, the penstock, the draft tube and the tail race;
- surge tanks, shafts and air vessels used to mitigate pressure transients in the hydraulic circuits and protect the plants against the so-called water hammer.

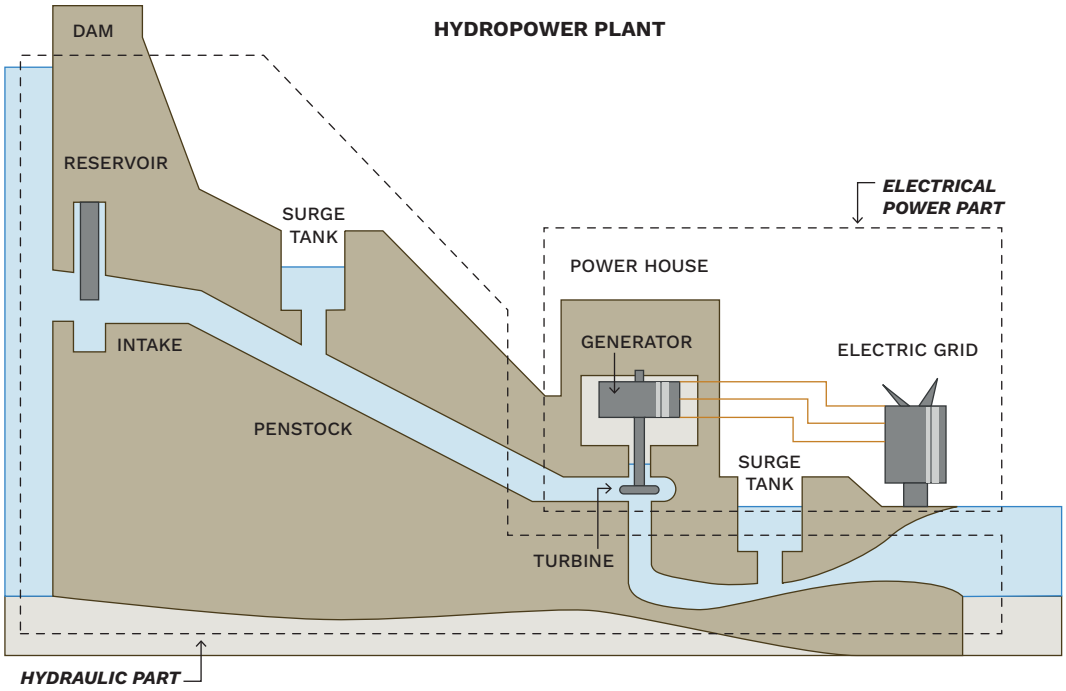

Figure 2.1: Example of hydropower plant with a dam.

Hydraulic machines can be classified according to the operating principle, the direction of the flow, the water head and the specific speed, as shown in Fig. 2.2. Based on the operating principle, we distinguish into impulse and reaction machines. The difference between the two is the way they convert the energy of a fluid into mechanical work [53].

Impulse machines work by directing the fluid to the turbine's blades at high velocity through a nozzle. The resulting change in momentum generates a force on the machine blades. The blades

are typically bucket-shaped to capture the fluid and facilitate the most efficient transfer of energy from the fluid to the machine. During its motion, the fluid flowing over the rotor blades experiences nearly constant pressure. Impulse turbines are often employed in high-head applications, which can reach up to 1000 meters. An example of an impulse machine is the Pelton turbine.

Reaction machines operate by reducing the pressure of the water flowing over the runner blades, causing an increase in velocity. Consequently, the change in pressure creates a reaction force on the moving blades. Usually, the blades design in reaction machines is more challenging than in impulse machines due to the complex fluid dynamics involved. As a result, reaction machines are more complex and expensive. Reaction turbines are used in low and medium-head applications. Specifically, Kaplan turbines are suitable for low-head applications, while Francis turbines are used in medium-head hydropower plants.

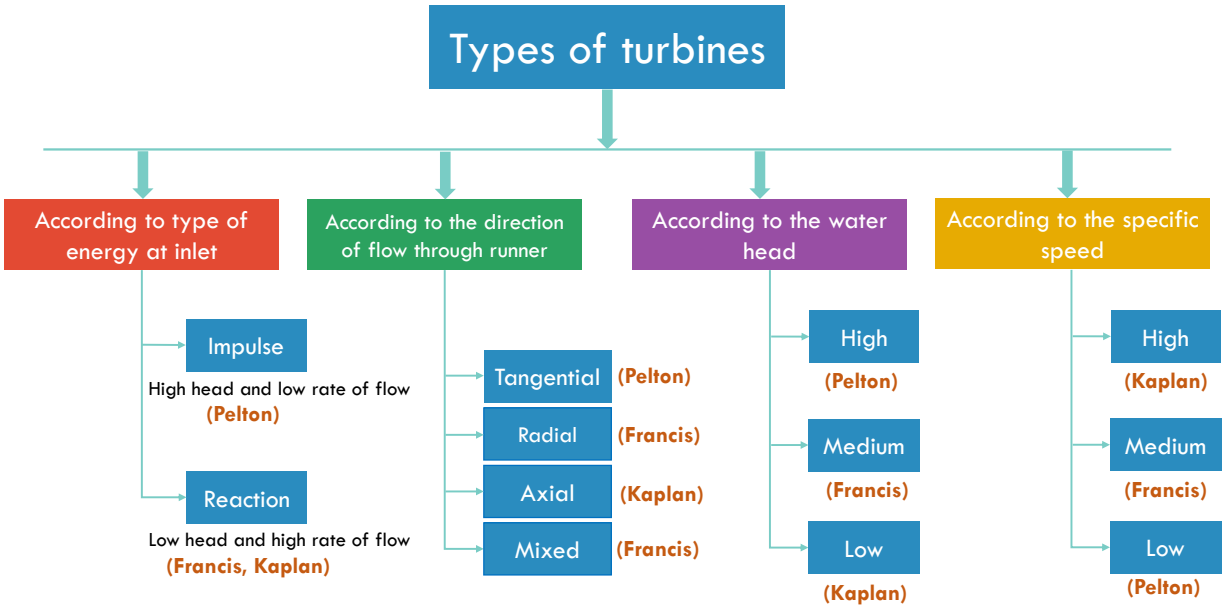

Figure 2.2: Hydraulic turbines classification.

The electrical part of a hydropower plant includes the synchronous generator used for electricity production, the exciter, the transformer, circuit breakers, switchgears, and protections.

Depending on the type of HPP, the number and size of components changes. For instance, high-head HPPs may have one or more surge tanks and different types of hydraulic machines, especially if the plant serves as a pumped-storage hydropower plant. In medium-head HPPs, surge tanks may not be present. In low-head HPPs, penstocks are generally short, and the hydraulic conduits mostly consist of low-pressure pipes.

This chapter focuses on developing and validating models of HPPs to support model-based control decision-making. Specifically, the chapter presents non-linear models of a medium-head hydropower plant and a run-of-river hydropower plant, which have undergone validation against a commercial software called SIMSEN. The objective of the models is to accurately reproduce

hydraulic transients and include them in a control framework that considers the physics of the phenomena and accounts for fatigue on critical components.

The process of developing a suitable model framework for control applications involves two main steps: (1) developing non-linear models of the HPP that accurately reproduce hydraulic quantities of interest, and (2) deriving linear models for efficient control implementation. Specifically, linear models enable a convex formulation of the optimization problem for the MPC (presented in Chapter 3), which is tractable and guarantees the discovery of a global optimum. However, linear models require adequate accuracy, which is why the linear estimation performances have been evaluated against non-linear models.

The chapter is organized as follows: Section 2.3 discusses appropriate modelling approaches for control applications. Then, the modelling of the main components of the hydraulic and electrical parts of the medium-head and low-head plants is developed to build complete non-linear models in Section 2.4. Finally, Section 2.5 proposes a linearization technique to deal with non-linearities in hydropower plant models and shows the performance evaluations of the linear models. Appendix A presents the validation of the models against SIMSEN.

2.3 Numerical models for control applications

Modelling is crucial to study the phenomena that may affect the good functioning of the system and its interactions with the power grid. Numerical models are at the base of this investigation. Selecting an appropriate model is typically a trade-off between accuracy and computation time, and it should be done based on the specific purpose or application. In the hydropower domain, hydraulic transient modelling is achieved using three-dimensional, two-dimensional, and one-dimensional models. All three approaches solve the fundamental equations that govern the flow movement, namely the conservation of mass and momentum.

Computational Fluid Dynamic (CFD) models are numerical methods that solve the fundamental equations of fluid dynamics iteratively on a discretized mesh in two or three dimensions. These models are applicable to various shapes and sizes, rendering them a powerful tool to study complex phenomena with high accuracy, including cavitation, vortex ropes, and other instabilities as a function of the geometry of the system. However, their main limitation is their high computational cost.

In contrast, one-dimensional (1-D) models utilize simple lumped elements to mesh the geometry and can describe the fluid flow and pressure in a single dimension, i.e., along the flow direction. Therefore, these models are best suited for configurations where the geometry consists of lines and intersection points, such as pipelines and tanks.

As this thesis focuses on models applied to model predictive control of HPPs, the primary requirement is to achieve tractable properties for real-time optimization. For this reason 1-D models are used. The developed models require a multi-physics approach as they include the hydraulic circuit, the mechanical inertia, the electrical installation, and regulation systems. For such applications, 1-D models offer the best trade-off between computational effort and accuracy, as reported in [54].

2.4 1-D models of hydropower plants

This section focuses on 1-D models of HPPs. The models of the main components of hydropower plants, namely the penstock, the turbine and the electric generator are combined in an Equivalent Electric Circuit (EEC) [54, 55]. EECs are based on the analogy between hydraulic and electrical quantities. In particular, pressure and discharge are treated as voltage and current of an electric circuit. The choice of the EEC method is justified by its excellent tractability, accuracy, and low computational cost in numerical simulations [54–56].

Fig. 2.3 shows the EEC of a medium-head HPP equipped with a Francis turbine, where the plant's components are modelled as follows:

- the upstream and downstream reservoir are modelled by the two voltage sources at the far ends of the circuit, H_r and H_d, respectively;
- the penstock is modelled by discretizing the conduit in a finite number of elements, say I, where each element is modelled as a third-order RLC circuit, with the index $i = 1, \ldots, I$. The voltage h_i is the water head (or static pressure) in the central part of the penstock element, whereas Q_i and Q_{i+1} is the water flow in the receiving and sending end of it;
- the hydraulic turbine is modelled as a controlled voltage source H_t and the inertia of the water closure within the turbine is represented by an equivalent inductance L_t in series to the turbine model [57].

The next sections present the detailed model of the penstock, the turbine and the electric generator.

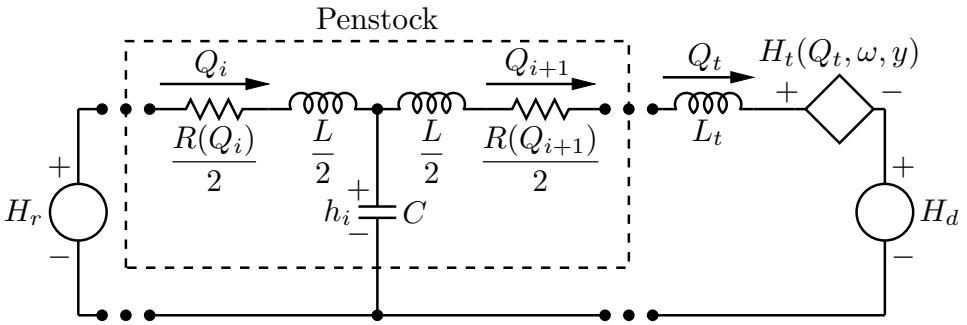

Figure 2.3: Equivalent circuit model of the hydraulic components of a medium-head hydropower plant.

2.4.1 Penstock

Penstocks are enclosed pipes that guide water from the upstream reservoir to the hydraulic turbine. The potential difference between the inlet and outlet of the penstock is the main source of the water's mechanical power. Penstocks are designed to withstand the internal pressure of water. Therefore, in the penstock model, the elasticity of water is considered as a critical factor [**?**].

The penstock model is a set of Partial Derivative Equations (PDEs) derived from the laws of mass and momentum conservation. The momentum equation embodies the equilibrium of forces exerted on a fluid volume, whereas the mass conservation equation describes the mass balance of a fluid flowing through a finite volume element.

Assuming one-dimensional flow through the penstock, the mass and momentum equations applied to a control volume of length dx are expressed as follows [54]:

$$\begin{cases} \dfrac{\partial h}{\partial x} + \dfrac{1}{gA}\dfrac{\partial Q}{\partial t} + \dfrac{\lambda Q|Q|}{2gDA^2} = 0 \\ \\ \dfrac{\partial h}{\partial t} + \dfrac{a^2}{gA}\dfrac{\partial Q}{\partial x} = 0. \end{cases} \tag{2.1}$$

where Q is the hydraulic discharge, h the piezometric head of water flowing in the pipe, A the cross-section of the penstock, D the pipe diameter, g the acceleration of gravity, a the wave speed in m/s and λ the Darcy-Weisbach friction factor. Notably, the absolute value of the discharge ensures that a dissipative term is always present.

Eq. (2.1) corresponds to a system of hyperbolic equations. When a disturbance is applied to the initial values of the equations, it is not felt simultaneously by every point in the space. The solutions of hyperbolic equations are waves that propagate at a finite speed relative to a fixed time coordinate [58]. The solution of Eq. (2.1) can be achieved with state-of-the-art methods as the Method of Charateristic (MOC) [59, 60], transfer functions [40, 61], and the EEC method leveraged in this work.

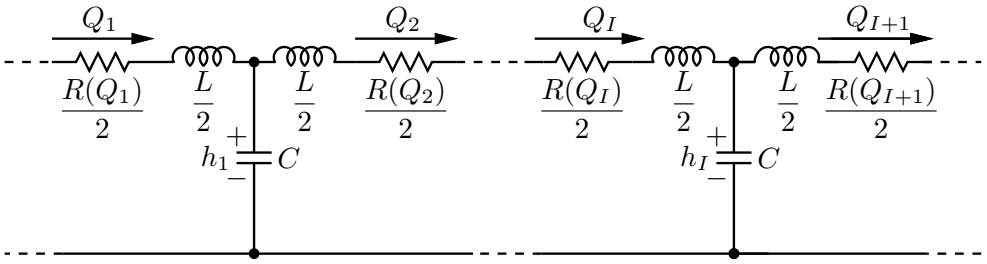

Figure 2.4: Equivalent circuit model of the penstock.

Eq. (2.1) is converted into Ordinary Differential Equations (ODEs) by discretizing the penstock into a finite number of elements $i = 1, \ldots, I$, each with a length of $dx = l/i$, where l is the total length of the penstock.

Fig. 2.4 shows the EEC model of the penstock, where each penstock element is modelled as a third-order RLC circuit described by the following set of equations:

$$\frac{dQ_i}{dt} = -\frac{R(Q_i)}{L} \cdot Q_i - \frac{2}{L} \cdot h_i + \frac{2}{L} \cdot h_{i-1} \tag{2.2a}$$

$$\frac{dQ_{i+1}}{dt} = -\frac{R(Q_i)}{L} \cdot Q_{i+1} + \frac{2}{L} \cdot h_i - \frac{2}{L} \cdot h_{i+1} \tag{2.2b}$$

$$\frac{dh_i}{dt} = \frac{1}{C} \cdot (Q_i - Q_{i+1}). \tag{2.2c}$$

where the hydraulic resistance R, inductance L and capacitance C are related, respectively, to energy losses, inertia, and storage effects and are defined as:

$$R(Q_i) = \frac{\lambda \cdot |Q_i| \cdot dx}{2g \cdot D \cdot A^2}, \quad L = \frac{dx}{g \cdot A}, \quad C = \frac{g \cdot A \cdot dx}{a^2}, \tag{2.3}$$

Eqs. (2.2a),(2.2b), (2.2c) correspond to the application of Kirchhoff's law to the electrical circuit of Fig. 2.4.

In order to numerically solve the system, it is advantageous to express the set of differential equations in the form of a state-space model representation:

$$\dot{x} = A\left(Q_i\right) \cdot x + B \cdot u. \tag{2.4}$$

The matrix form of (2.2a),(2.2b), (2.2c) is given by:

$$\frac{d}{dt} \cdot \begin{bmatrix} Q_i \\ Q_{i+1} \\ h_i \end{bmatrix} = \begin{bmatrix} -R/L & 0 & -2/L \\ 0 & -R/L & 2/L \\ 1/C & -1/C & 0 \end{bmatrix} \cdot \begin{bmatrix} Q_i \\ Q_{i+1} \\ h_i \end{bmatrix} + \begin{bmatrix} 2/L & 0 \\ 0 & -2/L \\ 0 & 0 \end{bmatrix} \cdot \begin{bmatrix} h_{i-1} \\ h_{i+1} \end{bmatrix} \tag{2.5}$$

The state variables of the system are:

- the discharge at the inlet of the control volume i: Q_i
- the discharge at the outlet of the control volume i: Q_{i+1}
- the piezometric head in the middle of the control volume i: h_i

The inputs of the system are:

- the piezometric head at the inlet of the control volume i: h_{i-1}
- the piezometric head at the outlet of the control volume i: h_{i+1}

More generally, for a penstock made by I-pipe elements, the $[A]$ and $[B]$ matrix become:

$$[A] = \begin{bmatrix} -R\left(Q_1\right)/L & 0 & 0 & 0_{(1,I+1)} & -2/L & 0 & 0 & 0 & \dots & 0_{(1,2I+1)} \\ 0 & -R\left(Q_2\right)/L & 0 & 0 & 1/L & -1/L & 0 & 0 & \dots & 0 \\ 0 & 0 & \ddots & 0 & 0 & \ddots & \ddots & 0 & \dots & 0 \\ 0 & 0 & 0 & -R\left(Q_{I+1}\right)/L & 0 & 0 & 1/L & -1/L & \dots & 0 \\ 0_{(I+1,1)} & 0 & 0 & 0 & 0 & 0 & 0 & 2/L & \dots & 0 \\ 1/C & -1/C & 0 & 0 & 0 & 0 & 0 & 0 & \dots & 0 \\ 0 & \ddots & \ddots & 0 & 0 & 0 & 0 & 0 & \dots & 0 \\ 0_{(2I+1,1)} & 0 & 1/C & -1/C & 0 & 0 & 0 & 0 & \dots & 0 \end{bmatrix} \tag{2.6}$$

$$[B] = \begin{bmatrix} 2/L & 0 \\ 0 & 0 \\ 0 & 0 \\ 0_{(I,1)} & -2/L \\ 0 & 0 \\ 0_{(I+1,1)} & 0 \end{bmatrix} \tag{2.7}$$

where the notation $(1, I+1)$ denotes the 1st row and the (I+1)th column of element of the matrix. The state vector x and input vector u are:

$$x = \begin{bmatrix} Q_1 & \dots & Q_{I+1} & h_1 & \dots & h_I \end{bmatrix}, ^\top \tag{2.8}$$

and

$$u = \begin{bmatrix} h_0 & h_{I+1} \end{bmatrix}. ^\top \tag{2.9}$$

Observing the given state-space model, it can be noted that:

- the A matrix has dimension $(2I+1) \cdot (2I+1)$ and operates on the state vector x of dimension $(2I+1) \cdot 1$. The state vector has $I+1$ discharges (Q_1 to Q_{I+1}) and I piezometric heads (h_1 to h_I);
- the B matrix has dimension $(2I+1) \cdot 2$ and operates on the inputs vector u of dimensions $2 \cdot 1$. The input vector comprises of inlet and outlet heads h_0 and h_{I+1}.

The selection of the number of penstock elements, I, is a trade-off between computational complexity and modelling accuracy. The set of ordinary differential equations is numerically integrated using standard algorithms such as 4th order Runge-Kutta, under the convergence condition imposed by Courant–Friedrichs–Lewy or "CFL" criteria [62]. The CFL criteria ensures the causality of the system because the information cannot transit faster than the wave speed [54] and it has the following form:

$$dt < \frac{a}{dx} \tag{2.10}$$

where dx and dt are the space and time discretization and a is the wave speed.

2.4.2 Hydraulic machines

For power grid simulations, hydraulic turbines are typically modelled using the “quasi-static” approach. This approach assumes that the behavior of hydraulic machines can be simulated as a sequence of different steady-state conditions during the transition between different operating points

[63]. The method preserves acceptable levels of accuracy to model dynamic interactions with the power grid and is computationally tractable [54]. By using characteristic curves the quasi-static approach links all operational variables of a turbine, namely its torque T_t, rotational speed N, head H_t, and flow Q_t. These curves are typically determined experimentally and formulated in terms of unit variables:

$$N_{11} = \frac{N \cdot D_n}{\sqrt{H_t}}, \quad Q_{11} = \frac{Q_t}{D_n^2 \sqrt{H_t}}, \quad T_{11} = \frac{T_t}{D_n^2 H_t} \tag{2.11}$$

where D_n is the diameter of the turbine. There are two characteristic curves, one for expressing the discharge factor Q_{11}, and the other for the torque factor T_{11}. Both are a function of the speed factor N_{11} and the controllable inputs, which are, for Francis turbines, the guide vane y, and, for Kaplan turbines, the guide vane y and the blade pitch β.

Francis turbine

Fig. 2.5 shows the characteristic curves of a Francis turbine with a specific speed of $\upsilon = 0.217$. The discharge and torque unit variables are plotted as a function of the speed unit for different guide vane openings y, with the values referenced to the best efficiency point value.

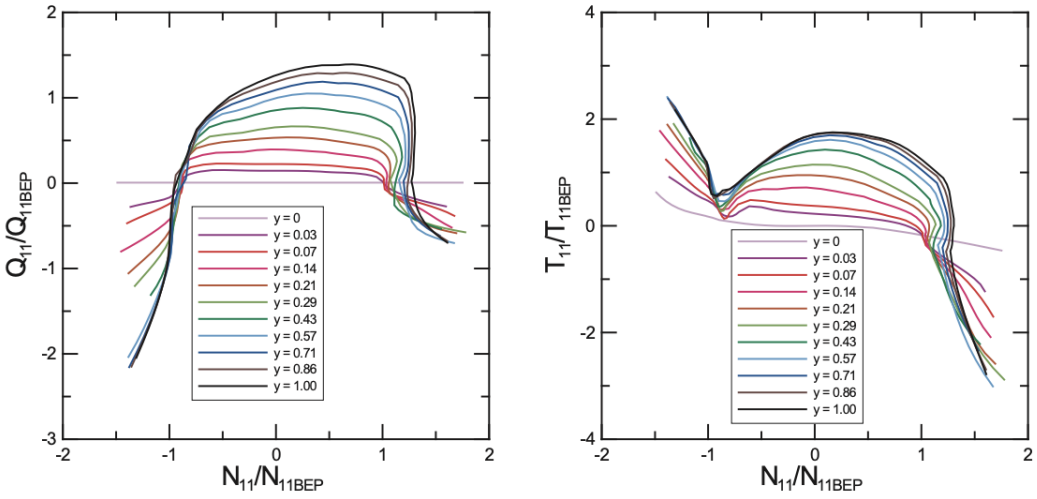

Figure 2.5: Characteristic curves of a Francis turbine with $\upsilon = 0.217$ [54].

The S-shape of some curves in Fig. 2.5 can cause numerical troubles in certain regions, specifically in the 1st and 4th quadrants [64]. To address this issue, we use the polar representation of the turbine characteristic, which preserves the similitude law [65].

In Fig. 2.6, the multiple value problem and the definition of the polar coordinates are illustrated. The polar angle θ is given by:

$$\theta = \operatorname{atan}\left(\frac{Q_{11}/Q_{11BEP}}{N_{11}/N_{11BEP}}\right). \tag{2.12}$$

The radial coordinate $r(\theta)$ is defined as the square root of the sum of the squares of the discharge and speed unit variables, normalized by their respective best efficiency point values as:

$$r(\theta)^2 = (Q_{11}/Q_{11BEP})^2 + (N_{11}/N_{11BEP})^2. \tag{2.13}$$

The head parameter $W_H(\theta)$ and the torque parameter $W_B(\theta)$ are introduced as follows :

$$W_H(\theta) = \frac{1}{r(\theta)^2} = \frac{H_t/H_{tBEP}}{(Q_{11}/Q_{11BEP})^2 + (N_{11}/N_{11BEP})^2}, \tag{2.14a}$$

$$W_B(\theta) = W_H(\theta) \cdot \frac{T_{11}}{T_{11BEP}} = \frac{T_t/T_{tBEP}}{(Q_{11}/Q_{11BEP})^2 + (N_{11}/N_{11BEP})^2}. \tag{2.14b}$$

Fig. 2.5 shows the polar representation of the Francis turbine characteristic of Fig. 2.7.

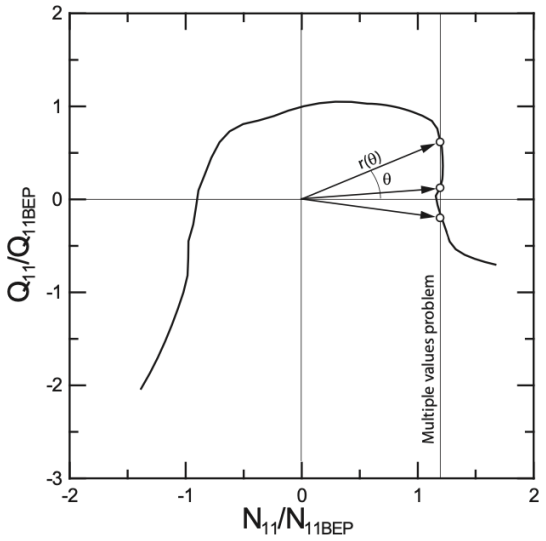

Figure 2.6: Multiple value problem and definition of the polar representation [54].

The electrical analogy entails the Francis turbine to be modelled as a pressure source $H_t = H_t(Q_t, N, y) = H_t(W_H, \theta, y)$ whose values are derived from the head characteristic $W_H(\theta)$.

The momentum equation applied to the rotational inertia yields the rotational pulsation:

$$T_t - T_{em} = J \cdot \frac{d\omega_m}{dt}, \tag{2.15}$$

The rotational pulsation ω_m can be related to the rotational speed N as $\omega_m = 2\pi N/60$, where 60 is used to convert from minutes to seconds. Therefore, Eq. 2.15 can be rewritten in terms of N as:

$$T_t - T_{em} = J \cdot \frac{d}{dt}\left(\frac{2\pi N}{60}\right) = \frac{2\pi J}{60} \cdot \frac{dN}{dt}. \tag{2.16}$$

The electromagnetic torque T_{em} is related to the electrical power output P_e of the generator as $T_{em} = P_e/\omega_m$. Therefore, the overall system equation can be written as:

$$T_t - \frac{P_e}{\omega_m} = \frac{2\pi J}{60} \cdot \frac{dN}{dt}. \tag{2.17}$$

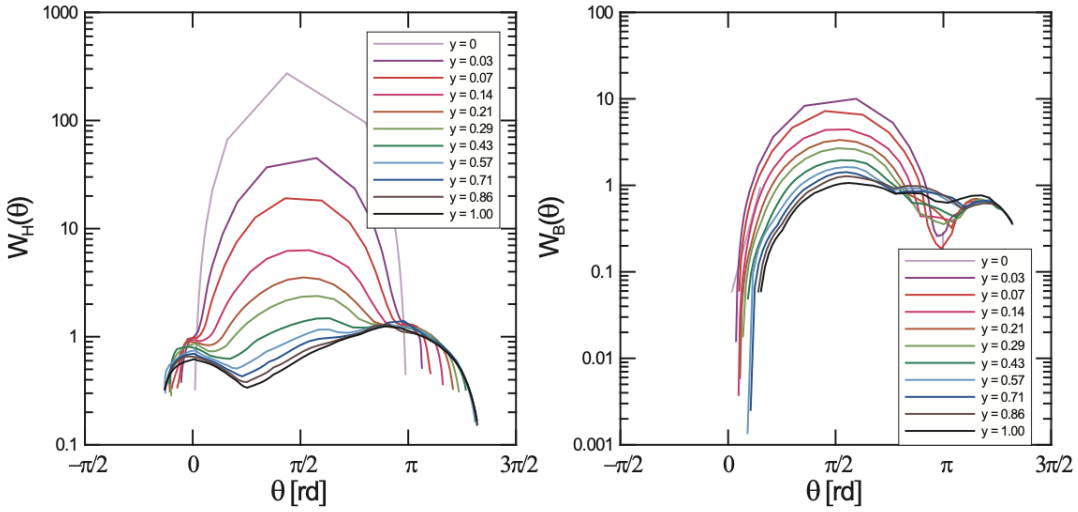

Figure 2.7: Polar representation of the Francis turbine of Fig.2.5, [54].

This equation relates the mechanical torque of the turbine T_t, the electrical power output of the generator P_e, the rotational speed N, and the total inertia of the rotating part J. It can be used to simulate the behavior of the hydropower plant and study its response to different operating conditions.

The electrical equivalent circuit of the Francis turbine is shown in Fig. 2.3, which includes the equivalent inductance L_t to account for the inertia effect of the water in the turbine. The value of L_t is given by:

$$L_t = \int_{I_{in}}^{I_{out}} \frac{dx}{g \cdot A(x)} = \frac{l_{eq}}{g \cdot A_{mean}}, \tag{2.18}$$

where I_{in} and I_{out} represent the inlet and outlet of the turbine, respectively. The integral is evaluated over the length of the turbine, and g is the gravity acceleration. $A(x)$ is the cross-sectional area of the turbine at a distance x along its length. l_{eq} is the equivalent length of the turbine and A_{mean} is the average cross-sectional area of the turbine.

Kaplan turbine

The characteristic curves $W_H(\cdot)$ and $W_B(\cdot)$ of Kaplan turbines depend not only on the flow rate, head and rotational speed but also on the blade pitch angle β. The polar representation of the Kaplan turbine is given by a family of characteristics $W_H(\theta, y, \beta)$ and $W_B(\theta, y, \beta)$ corresponding to different values of β. To obtain polar characteristics corresponding to blade angles not provided in the characteristic curves, linear interpolation is used between two given blade angles β_1 and β_2, as shown in Fig. 2.8.

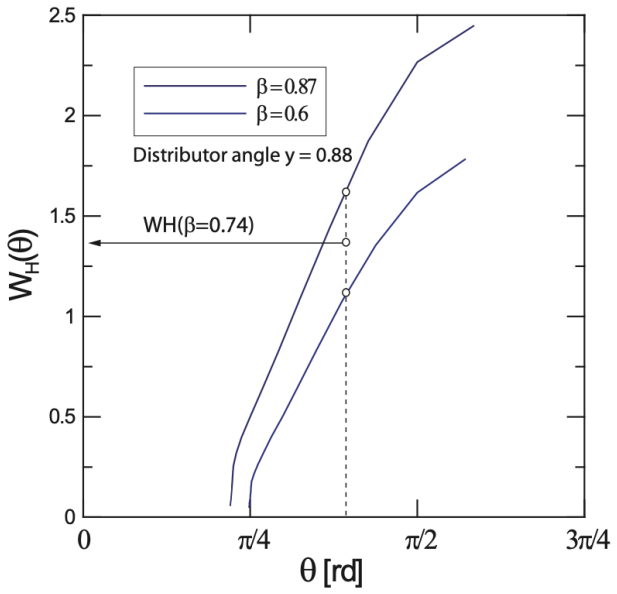

Figure 2.8: Linear interpolation of W_H between 2 different blade angles β for a given guide vane opening y, [54].

2.4.3 Synchrounous generator

Synchronous Generators (SGs) transform the mechanical energy from the hydraulic turbine into electric energy. This thesis leverages the "classical model" of SGs, a second-order dynamic model that captures the dynamics of the machine's phase and angular speed. The classical model targets the time scale associated with electromechanical dynamics and the influence of the turbine and the generator control systems.

The equation of motion of an SG is referred to as *swing equation*, since it represents the swing of the rotor (or power) angle δ during a disturbance [40]. The swing equation takes the common form:

$$M\frac{d\Delta\omega}{dt} = P_m - P_e, \tag{2.19a}$$

$$\frac{d\delta}{dt} = \Delta\omega, \tag{2.19b}$$

where $\Delta\omega$ is the rate of change of the angular acceleration, P_m is the mechanical power, P_e is the electrical power generated by the machine, δ is the rotor angle and M is the inertia coefficient. The inertia coefficient represents the ratio of the kinetic energy stored in the machine to the rate of change of its angular speed and is equal to:

$$M = \frac{2HS_n}{\omega_e}, \tag{2.20}$$

with S_n as the machine rating in MVA, ω_e as the synchronous pulsation in electrical radians per second and H as the inertia constant, representing the combined inertia of the generator and the turbine. Typical values of H for hydraulic units are between 2 and 4 seconds [40].

The electric power P_e generated by the machine is a function of the rotor angle δ and is given by (for round-rotor generators):

$$P_e(\delta) = \frac{E_q V_s}{x_d} \cdot \sin(\delta), \tag{2.21}$$

where E_q is the quadrature-axis Electromotive Force (EMF), V_s is the reference voltage and x_d is the synchronous reactance.

Eqs. (2.19a),(2.19b),(2.21) are combined in the state-space form:

$$\dot{x} = A \cdot x + B \cdot u(x), \tag{2.22}$$

where the states and the inputs are defined as follows:

$$x = \begin{bmatrix} \Delta\omega & \delta \end{bmatrix}, ^{\top} \tag{2.23}$$

and

$$u = \begin{bmatrix} P_m - P_e(\delta) & 0 \end{bmatrix}. ^{\top} \tag{2.24}$$

The state-space model of the system is then:

$$\frac{d}{dt} \cdot \begin{bmatrix} \Delta\omega \\ \delta \end{bmatrix} = \begin{bmatrix} 0 & 0 \\ 1 & 0 \end{bmatrix} \cdot \begin{bmatrix} \Delta\omega \\ \delta \end{bmatrix} + \begin{bmatrix} 1/M & 0 \\ 0 & 0 \end{bmatrix} \cdot \begin{bmatrix} P_m - P_e(\delta) \\ 0 \end{bmatrix}. \tag{2.25}$$

The model is non-linear due to the sinusoidal function, $\sin(\delta)$, which introduces a non-linear relationship between the angle δ and the power.

2.4.4 State-space representation

The state vector for the circuit depicted in Fig. 2.3, which consists of a 1-element penstock, Francis turbine, and generator, is given by:

$$x = \begin{bmatrix} Q_1 & Q_t & h_1 & \Delta\omega & \delta \end{bmatrix}^{\top} \tag{2.26a}$$

where Q_1 is the water flow in the penstock's first element, Q_t is the turbine discharge, $\Delta\omega$ the rotor speed deviation in electrical radians per second and δ is the power angle, and $^{\top}$ denotes transpose. The input vector is:

$$u(Q_t, N, y, \delta) = \begin{bmatrix} H_r \\ H_t(Q_t, N, y) - H_d \\ P_m(Q_t, N, y) - Pe(\delta) \\ 0 \end{bmatrix} \tag{2.26b}$$

where H_r is the reservoir head, H_d the downstream head, P_e the electric power of the generator as in (2.21), H_t and P_m the turbine head and hydraulic power from the characteristic curves in (2.14a)-(2.14b). They both depend on the state components Q_t and N, and guide vane opening y. The non-linear state-space model is:

$$\dot{x} = A(Q_i)\, x + Bu(Q_t, N, y, \delta). \tag{2.26c}$$

The state and input transformation matrices are:

$$A(x) = \begin{bmatrix} \frac{R(Q_1)}{L} & 0 & -\frac{2}{L} & 0 & 0 \\ 0 & \frac{R(Q_t)}{L} & \frac{2}{L} & 0 & 0 \\ \frac{1}{C} & -\frac{1}{C} & 0 & 0 & 0 \\ 0 & 0 & 0 & 0 & 0 \\ 0 & 0 & 0 & 0 & 1 \end{bmatrix}, B = \begin{bmatrix} \frac{2}{L} & 0 & 0 & 0 \\ 0 & -\frac{2}{L} & 0 & 0 \\ 0 & 0 & 0 & 0 \\ 0 & 0 & \frac{1}{M} & 0 \\ 0 & 0 & 0 & 0 \end{bmatrix} \tag{2.26d}$$

The hydroacoustic resistance in Eq. (2.3) depends on the flow in the penstock and turbine discharge, which results in the dependence of matrix A on these quantities. If the penstock is modelled using I elements, the state vector will include $(2I + 3)$ elements, comprising of $I + 1$ discharges, I heads, 1 speed deviation, and 1 power angle. Additionally, the model for the Kaplan turbine accounts for the impact of blade angle β on H_t and P_m.

2.5 Linearized models of the hydropower plant

1-D models presented above are non-linear. This section presents how they can be linearized.

The first part discusses how to tackle the main non-linearities of the HPP. Nevertheless, linearization unavoidably introduces some error, as the linear models are approximations of the true non-linear system.

Therefore, the second part of this section investigates the performance of linearizated models in estimating the hydraulic and mechanical quantities of interest. The estimations are compared with the outputs of a validated hydraulic model of medium- and low-head HPPs. Thus, this section exclusively focuses on the linearization of hydro-mechanical components, while excluding the linear model of the synchronous generator from the current analysis.

2.5.1 Dealing with HPP's non-linearities

The state-space model described in (2.26) exhibits non-linearities with respect to both the state and controllable input variables. The first non-linearity arises from the dependence between the hydroacoustic resistance R and the discharge Q as presented in (2.3). By assuming small variations of the operating point, the discharge, thus R, can be approximated as a constant, leading to a linear and time-invariant formulation of the penstock model. The second non-linearity stems from the turbine's characteristic curves. These curves are typically derived from experimental measurements and cannot be linearized analytically. Therefore, a numerical linearization based on a first-order Taylor expansion is proposed.

To illustrate the approach, the linear model of the head $\hat{H}$ is:

$$\begin{aligned} \hat{H}_t(Q_t, \omega, y) \approx H_t(Q_{t_0}, \omega_0, y_0) + d_Q^H \cdot (Q_t - Q_{t_0}) + \\ + d_\omega^H \cdot (\omega - \omega_0) + d_y^H \cdot (y - y_0). \end{aligned} \tag{2.27}$$

where the coefficients d_Q^H, d_ω^H, d_y^H are the partial derivatives of $H_t(Q_t, \omega, y)$ calculated at an operating point Q_{t_0}, ω_0, y_0. These coefficients are computed numerically by differentiating the head

characteristic as:

$$d_Q^H := \left.\frac{\partial H_t}{\partial Q_t}\right|_{Q_{t_0}} = \frac{H_t(Q_{t_0}+\epsilon) - H_t(Q_{t_0}-\epsilon)}{2\epsilon}, \tag{2.28a}$$

$$d_\omega^H := \left.\frac{\partial H_t}{\partial \omega}\right|_{\omega_0} = \frac{H_t(\omega_0+\epsilon) - H_t(\omega_0-\epsilon)}{2\epsilon}, \tag{2.28b}$$

$$d_y^H := \left.\frac{\partial H_t}{\partial y}\right|_{y_0} = \frac{H_t(y_0+\epsilon) - H_t(y_0-\epsilon)}{2\epsilon}, \tag{2.28c}$$

where constant quantities have been omitted from the argument list for compactness. After linearizing as in (2.27), the model in Fig. 2.3 becomes linear and time invariant.

Similarly, the turbine's torque can be approximated as a linear combination of the same inputs as [66]:

$$\begin{aligned}\hat{T}_t(Q_t, \omega, y) \approx T_t(Q_{t_0}, \omega_0, y_0) + d_Q^T \cdot (Q_t - Q_{t_0}) + \\ + d_\omega^T \cdot (\omega - \omega_0) + d_y^T \cdot (y - y_0),\end{aligned} \tag{2.29}$$

where the values of the coefficients d_Q^T, d_ω^T, d_y^T are computed using the same method of numerical differentiation as described in (2.28) but applied to the torque characteristics.

Under these assumptions, the model in (2.26c) can be written as the following continuous time linear state-space (the notation $\hat{\cdot}$ refers to continuous-time state-space matrices):

$$\dot{x}\left(\hat{t}\right) = \hat{A}x(\hat{t}) + \hat{B}_y y(\hat{t}) + \hat{B}_z \begin{bmatrix} H_u(\hat{t}) \\ \mu - H_d(\hat{t}) \end{bmatrix} \tag{2.30}$$

or, more compactly as

$$\dot{x}(\hat{t}) = \hat{A}x(\hat{t}) + \hat{B}_y y(\hat{t}) + B_z z(\hat{t}) \tag{2.31}$$

where $\hat{A} \in \mathbb{R}^{(2I+1)\times(2I+1)}$ is the system matrix, x is the time-varying state vector in (2.26), $\hat{B}_y \in \mathbb{R}^{(2I+1)\times 1}$ the input matrix for the controllable input (i.e., guide vane y), $\hat{B}_z \in \mathbb{R}^{(2I+1)\times 2}$ the input matrix for the uncontrollable inputs in $z(t)$, (i.e., the head of the up- and down-stream reservoir) and μ is an input coefficient that follows from the linearization procedure.

The values of $\hat{A}$, $\hat{B}_y$, $\hat{B}_z$, and μ are determined using the plant's characteristics and the linearization point, as outlined in [66], and are considered as inputs to the problem. The upstream and downstream head values, H_u and H_d, are also inputs that are obtained from measurements. As the focus is on providing frequency regulation services with time dynamics in the range of seconds to minutes, it is assumed that the water levels in the reservoirs remain constant.

2.5.2 Performance evaluation of HPP linear models

To evaluate the performance of the linear models, time domain simulations are conducted by comparing their output with that of the non-linear models. The evaluation procedure consists of three steps:

- **Step 1:** a linear model is computed for each given operating point. The operating point is specified by the guide vane opening, net head, and rotational speed. Nine different points are considered, with guide vane openings ranging from 0.2 pu to 1 pu in increments of 0.1 pu, representing the typical operating range of a power plant. The net head is assumed constant at its nominal value, and the rotational speed is set to 50 Hz to represent steady-state synchronous operations. For the low-head HPP with a Kaplan turbine, the blade pitch is chosen as a function of the guide vane according to the on-cam curve;
- **Step 2:** each linear model is used to simulate operations for a stepwise change of the guide vane. Twenty different stepwise changes, ranging from -0.5 pu to 0.5 pu in increments of 0.025 pu, are considered. All the combinations resulting in unfeasible guide vane openings (e.g., guide vane 0.2 and stepwise change of 0.5) are excluded. In this way, a total of 41 x 9 (minus the unfeasible combinations) simulations are performed. For the Kaplan turbine, each guide vane deviation determines a deviation of blade angle according to the on-cam curve;
- **Step 3:** for each simulation, the estimation error is calculated as the difference between the linear model and the ground-truth model.

We analyze estimates of:

1. the turbine torque, relevant in the context of characterizing the mechanical and electric power of the plant;
2. the spatially averaged head in the penstock for the medium-head HPP and the head at the turbine for the low-head plant, relevant to assess mechanical load levels, and fatigue, of HPPs.

2.5.3 Medium-head plant with Francis turbine

Figs. 2.9 and 2.10 show the transient and steady-state Mean Absolute Error (MAE) of torque and head, respectively, for the medium-head HPP with Francis. Based on these results, the following findings can be drawn:

- **Finding 1:** the reliability of linear estimates is higher for the head than for the torque. This is because the torque model exhibits more pronounced non-linearities.
- **Finding 2:** the estimation performance deteriorates with larger step-wise variations of the guide vane for a given opening. This is expected because linear models are first-order approximations of non-linear models, and small deviations from the linearization point result in better local approximations.
- **Finding 3:** the steady-state MAE for linear head estimates (maximum error: 1%) is lower than the transient MAE (maximum error: 10%). However, the torque model performs similarly in both cases.
- **Finding 4:** for guide vane variations smaller than 0.1 pu, torque estimation errors are less than 10% (except for guide vane 0.7 and less than 0.4), and head estimation errors are less than 1%.

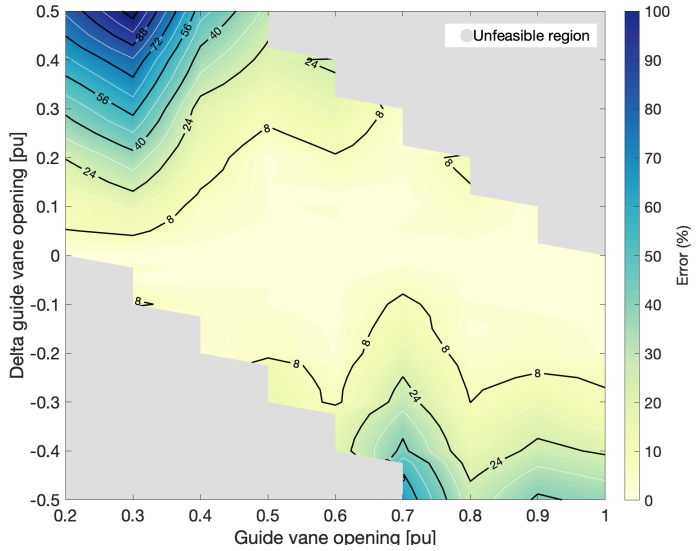

(a)

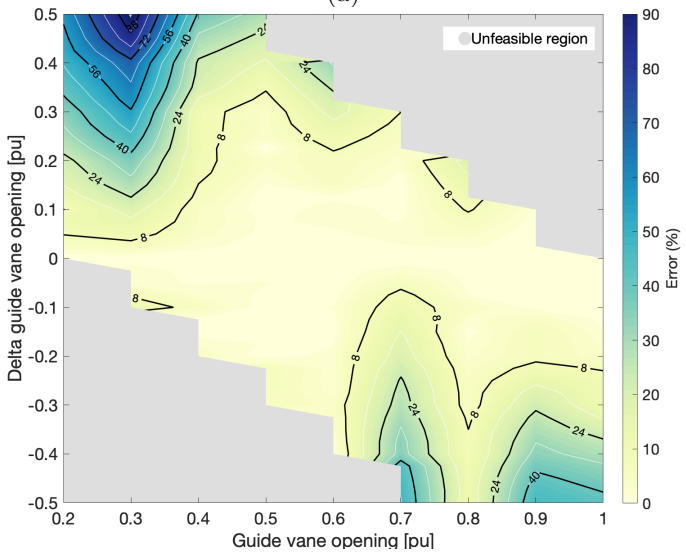

(b)

Figure 2.9: Francis medium-head HPP, turbine torque: MAE of the linear estimations in transient (a) and steady-state (b) conditions.

In the light of Finding 4, it can be concluded that the use of linear models is justified in small-signal applications and where these error levels are acceptable. Linear models provide computationally tractable models that can be utilized in optimization problems, including convex optimization problems for optimal decision-making.

2.5.4 Low-head plant with Kaplan turbine

Transient and steady-state performance of torque and head estimations are respectively shown in Figs. 2.11 and 2.12. Similar observations to those for the medium-head HPP with Francis can be drawn. In particular:

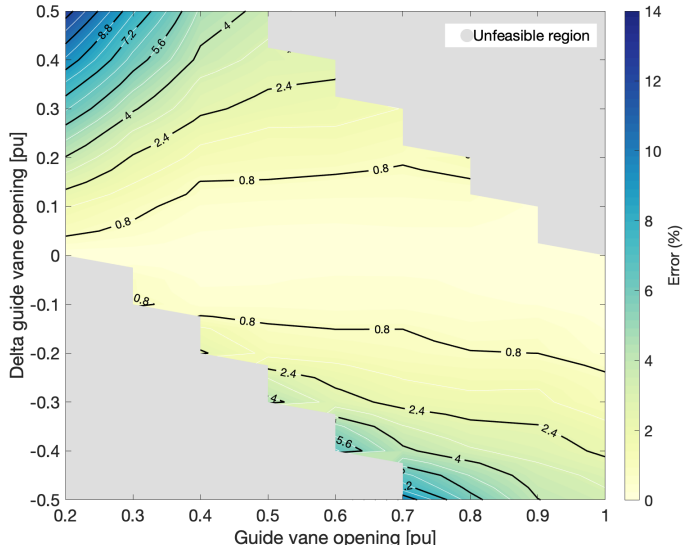

(a)

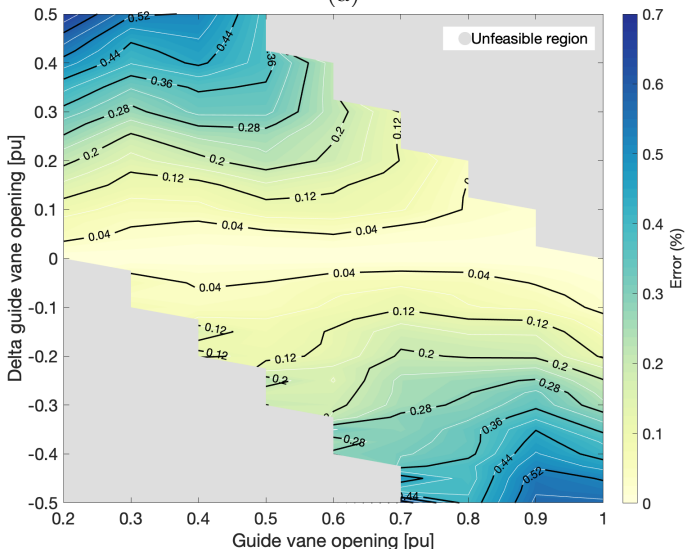

(b)

Figure 2.10: Francis medium-head HPP, spatially averaged head in the penstock: MAE of the linear estimations in transient (a) and steady-state (b) conditions.

- **Finding 1:** linear head estimations are more accurate than those for torque.
- **Finding 2:** smaller step-wise variations result in smaller estimation errors.
- **Finding 3:** in steady-state conditions, head estimates are significantly more reliable than during transients, with errors less than 0.1% and 30%, respectively. For the torque, there is no significant difference between the two cases.
- **Finding 4:** for small signal variations (e.g., ±0.1 pu of the guide vane), torque errors are approximately within a 10% band, and head errors within 0.8%. These results suggest that the linear models are suitable for small-signal applications with relatively small errors, which

can be useful for implementing computationally tractable models in optimization problems for decision-making.

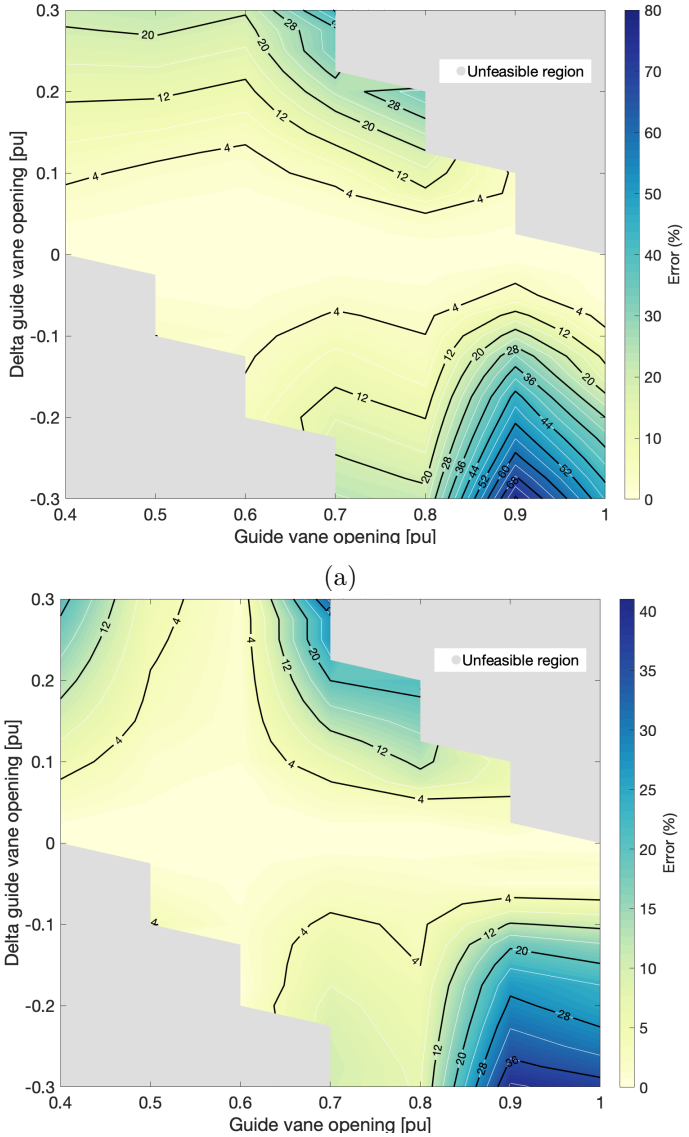

Figure 2.11: Kaplan low-head HPP, turbine torque: MAE of the linear estimations in transient (a) and steady-state (b) conditions.

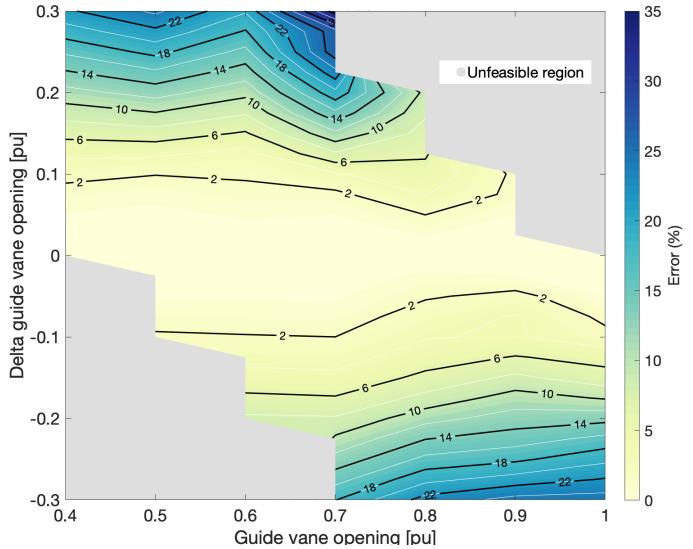

(a)

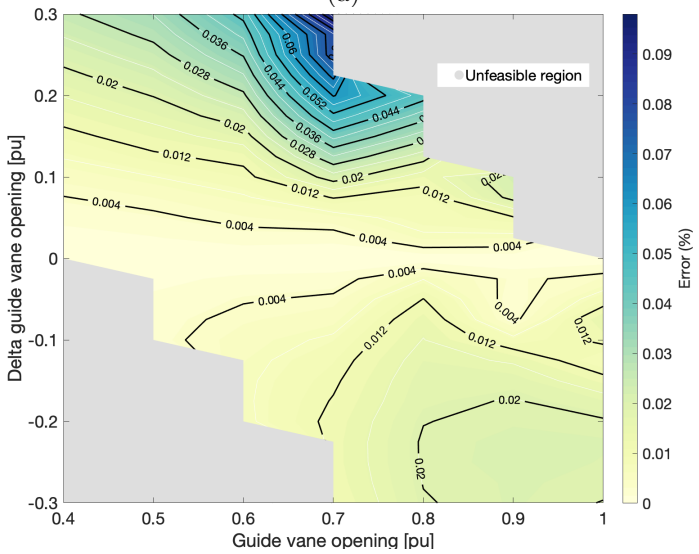

(b)

Figure 2.12: Kaplan low-head HPP, head at the turbine inlet: MAE linear estimations in transient (a) and steady-state (b) conditions.

2.6 Conclusions

This chapter has focused on 1-D models of a medium- and a low-head HPP. The models have been formulated using the EEC method. The penstock has been represented as a series of T-shaped RLC branches, while the hydraulic turbines have been modelled with the quasi-static approach. On the electric side, the synchronous generator was modelled using a second-order dynamic model to capture the electromechanical dynamics of rotor speed and power angle. The resulting model is non-linear due to the dependency between the hydroacoustic resistance R and discharge Q, and the characteristic curves of the hydraulic machines.

As an original contribution of this thesis, linearized models have been proposed. The lineariza-

tion involved:

1. assuming that the hydroacoustic resistance is independent of the flow; and
2. modelling the turbine with a first-order Taylor expansion around the operating point.

Linear estimates of the turbine torque and head in the penstock were compared against the non-linear model to evaluate the performance of medium- and low-head HPPs equipped with Francis and Kaplan turbines, respectively.

The results showed that the linear estimates of the head are more reliable than those of the torque. Moreover, for variations of the controllable input in a ± 0.1 pu range, the relative mean absolute error of the linear estimates was less than 10% for the torque and less than 1% for the head. These error levels are considered acceptable in small signal applications, making the linear models a more tractable alternative to the non-linear models. This opens up the possibility of developing efficient model predictive control based on convex optimization, as shown in the next section.

Chapter 3

Model predictive control of a medium-head hydropower plant for stress reduction

This chapter develops a receding horizon MPC to reduce the mechanical stress on the penstock of medium- and high-head HPPs and presents the methodology adopted to assess fatigue. The MPC leverages linear models presented in the previous chapter to reproduce hydraulic phenomena related to the mechanical stress in the penstock accurately. The results show that the MPC reduces penstock stress and damage, outperforming existing controllers. The proposed MPC is then used to derive a power set-point splitting strategy for a hybrid HPP. The hybrid HPP controller's formulation reduces fatigue in the penstock while maintaining the same provision of primary frequency control as the case without MPC.

3.1 Résumé en français

Ce chapitre se penche sur les possibles défaillances par fatigue des conduites forcées (penstocks) dans les centrales hydroélectriques de tête moyenne, attribuées à l'augmentation des services auxiliaires [16, 36]. Les conséquences critiques de ces phénomènes sont illustrées dans la Figure 3.1, montrant une augmentation des dommages liés à la régulation de fréquence. La défaillance des penstocks peut entraîner des événements catastrophiques, entraînant des temps d'arrêt prolongés et des coûts de maintenance accrus. Le chapitre propose une approche de contrôle visant à réduire la fatigue mécanique des penstocks en ajustant de manière appropriée le point de consigne des pales directrices.

Le concept clé d'éviter les cycles de stress au-delà de la limite de fatigue a été utilisé pour développer le MPC. Ce dernier reçoit le point de consigne des pales directrices du gouverneur de la centrale et calcule de nouvelles pales directrices qui n'induisent pas de fatigue. Le MPC utilise des modèles linéaires de la centrale pour estimer les contraintes et les maintenir en dessous de la limite de fatigue en résolvant un problème d'optimisation convexe.

Le contrôleur parvient ainsi à fournir une puissance régulatrice similaire à la centrale d'origine

tout en réduisant considérablement les dommages aux conduites hydrauliques. De plus, un stockage d'énergie par batterie (BESS) est inclus dans la stratégie de contrôle pour compenser la puissance régulatrice manquante de la centrale.

La structure du chapitre se décompose comme suit : la Section 3.3 aborde le phénomène de la secousse hydraulique, la Section 3.4 présente la méthodologie d'évaluation de la fatigue des penstocks, la Section 3.5 développe le contrôle prédictif basé sur le modèle pour la réduction de la fatigue, la Section 3.6 évalue les performances du contrôleur et la Section 3.7 explore l'implémentation d'une BESS dans l'algorithme de contrôle.

Les résultats de simulation obtenus avec un modèle de circuit équivalent non linéaire d'une centrale de tête moyenne ont démontré que :

- les modèles linéaires fournissaient des estimations suffisamment précises de la charge des penstocks pour appliquer efficacement les contraintes de stress;
- le MPC réduisait les dommages aux penstocks par rapport aux contrôleurs standard de centrales et aux filtres passe-bas de référence ;
- la formulation convexe proposée du problème MPC était computationnellement efficace, se résolvant rapidement (en dizaines de millisecondes) et adaptée à une mise en œuvre dans des contrôleurs en temps réel.

En conclusion, le chapitre aborde également le contrôle d'une centrale hybride équipée d'une batterie. Les résultats montrent que la contribution de la BESS nécessaire pour réduire la fatigue des penstocks était une petite fraction de la puissance nominale, ce qui pourrait avoir des implications positives pour les besoins de dimensionnement et de dégradation de la BESS.

3.2 Introduction

Possible fatigue failures of penstocks due to increased provision of ancillary services have been identified as critical phenomena in medium-head HPPs [16, 36]. Fig. 3.1 shows the damage along the penstock length in four cases. During case A and B, no ancillary services are provided by the plant. In case C, only Secondary Frequency Control (SFC) is provided. In case D, both primary and secondary frequency regulation are active. As visible, providing frequency regulation increases the damage along the penstock up to ten times compared to case A. The failure of the penstock can result in catastrophic events [15, 67], leading to prolonged downtimes and increased maintenance costs. Furthermore, the lack of effective solutions for monitoring the health of penstocks exacerbates the problem.

The cause of penstock damage is hydraulic transients (or water hammers) due to rapid variations of the power plant's set-point. With reference to Fig. 1.4, the governor of the plant processes the grid frequency and the power set-point (i.e., *Power reference*) and adjusts the guide vane opening to control the turbine's power output. This can cause hydraulic transients along the penstock, resulting in fatigue damage.

This chapter proposes a controller to reduce mechanical fatigue in the penstock by properly "tapping" the guide vane set-point. This controller explicitly formulates the mechanical loads on

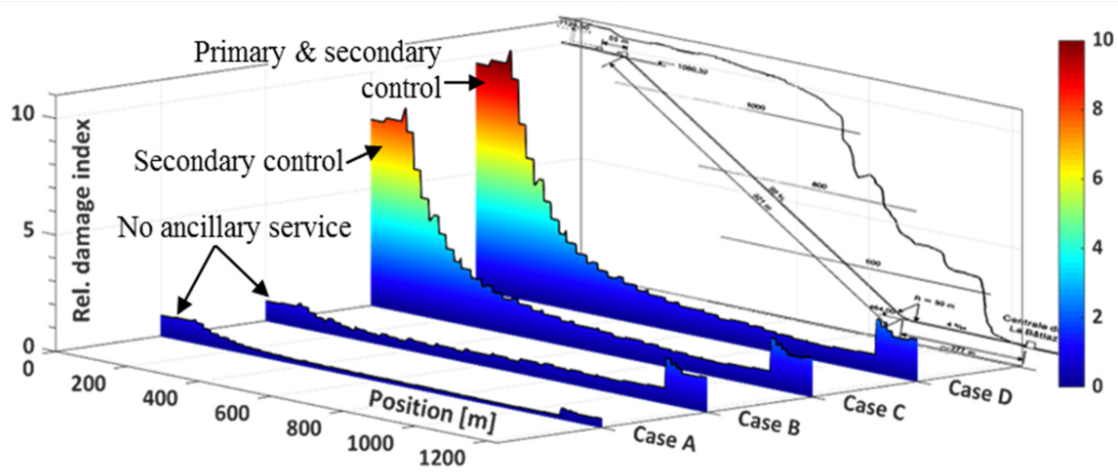

Figure 3.1: Increased penstock damage due to regulation duties [16].

the penstock by using the models developed in Chapter 2 to remove these components of the power set-point that contribute to excess penstock fatigue. By doing so, the controller can deliver similar regulating power to the original HPP while significantly reducing damage to the hydraulic conduits. Additionally, a BESS is included in the control strategy to compensate for the missing regulating power from the HPP.

The chapter is structured as follows: Section 3.3 describes the water hammer phenomenon. Section 3.4 presents the methodology for penstock's fatigue evaluation. Section 3.5 develops a model predictive control for fatigue reduction. Section 3.6 evaluates the performance of the MPC controller in reducing penstock fatigue in a medium-head HPP by comparing it to a benchmark Low-Pass Filter (LPF) and the fatigue-aware filter (discussed in Appendix B), which was a preliminary contribution to fatigue reduction control, developed before the MPC. Finally, Section 3.7 shows the implementation of the BESS in the control algorithm and compares the conventional HPP with its hybrid counterpart.

3.3 Water hammer effect

Water hammer arises from the dynamic changes in flow velocities within pipes. It typically occurs when a valve is closed rapidly, resulting in high-pressure waves propagating through the pipes. The vibrations generated in the pipes produce a distinctive banging noise, which is why the term "water hammer" is used.

The water hammer phenomenon is now explained. Fig. 3.2 shows an upstream reservoir at a piezometric head H_0 that pushes the fluid through a horizontal pipe with length L, diameter D, and friction coefficient λ, and a valve that regulates the velocity C of the water.

The magnitude rise of the water hammer pressure can be calculated using the Joukowsky equation [68]. The equation is derived by applying mass and momentum conservation law to a

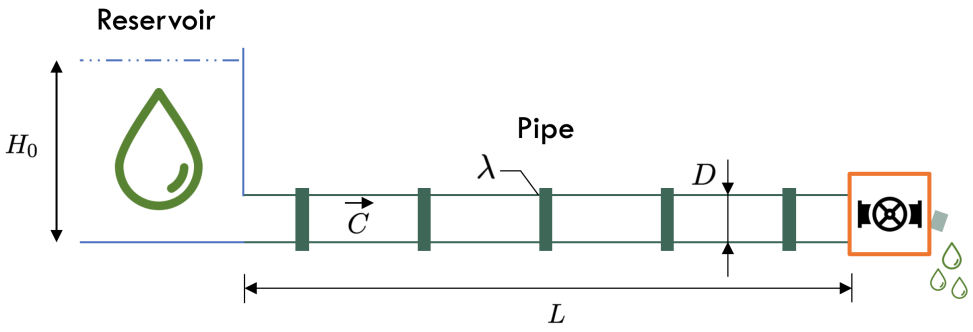

Figure 3.2: Schematic of a pipe connected to a upstream reservoir and a valve.

control volume of the pipe, and it expresses the overpressure as a function of the velocity change:

$$\Delta p = \rho \cdot a \cdot \Delta C, \tag{3.1}$$

where ρ is the density of the fluid, a is wave speed and ΔC is the velocity change of the fluid. The overpressure in terms of the head is given by:

$$\Delta H = \frac{a \cdot \Delta C}{g}. \tag{3.2}$$

The maximum overpressure is achieved when the valve passes from open to fully closed, with a maximum change in fluid velocity $\Delta C = C_0$:

$$H_{max} = \frac{a \cdot C_0}{g}. \tag{3.3}$$

The wave speed a is the speed of sound in the pipe and is determined by a modified Hook's law formula, which takes into account the fluid and pipe wall's stiffness:

$$a = \sqrt{\frac{1}{\rho \cdot [\frac{1}{K} + \frac{D}{E \cdot e}]}}, \tag{3.4}$$

where $K = 2.19 \cdot 10^9$ Pa is the bulk modulus of the fluid when it has no air bubbles, E is the Young's modulus of pipe material and e is the wall thickness of the pipe.

The presence of bubbles in the water can significantly reduce the value of the bulk modulus, and, thus, the wave speed. The stiffness of the system is affected by Young's modulus, which depends on the material, and as it decreases, so does the wave speed.

3.3.1 Valve closure time and wave reflection

To understand the dynamics of the water hammer effect, four phases of the phenomena are defined, as shown in Fig. 3.3:

1. **Phase 1.** When the valve position passes from open to closed, the fluid's velocity in the proximity of the valve suddenly becomes zero, causing a pressure wave that propagates up the pipe with a velocity of a. As a result of this wave propagation, the flow velocity along

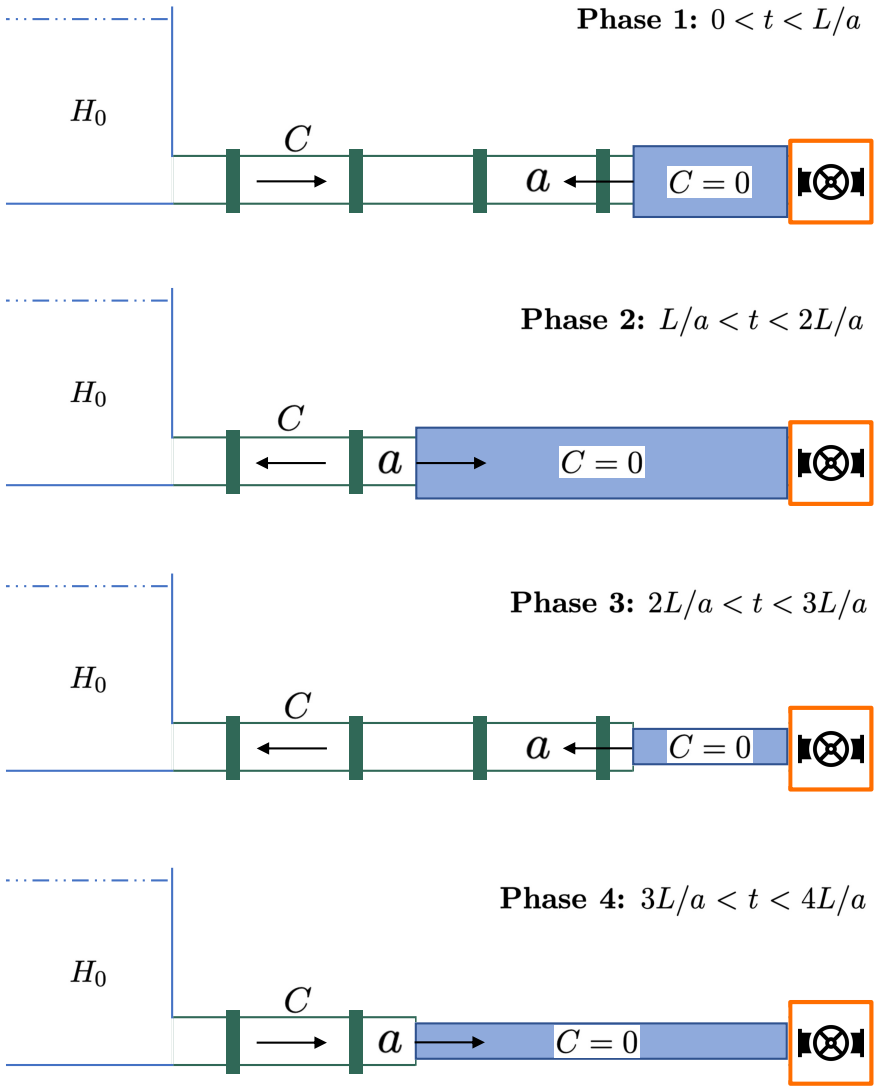

Figure 3.3: Water hammer phases

the pipe changes from its initial value C to zero. The amplitude of the overpressure can be determined using the Joukowsky equation [68]. The pressure wave reaches the upstream reservoir at $t = L/a$. At this time, the entire pipeline pressure has increased by $\rho \cdot a \cdot \Delta C$, and the fluid velocity along the pipe is zero. However, the overpressure at the inlet of the pipe is an unsteady condition as the pressure at this point is set by the head of the reservoir H_0. To respect this boundary condition, the fluid must move from the high-pressure pipe back to the valve, thereby inducing the first wave reflection.

2. **Phase 2.** The pressure wave now travels down the pipe. According to the reverse direction of the flow, the pipe experiences a drop in pressure across the wavefront, with amplitude $\rho \cdot a \cdot \Delta C$, where ΔC is, now, negative. At the time $t = 2L/a$, the pressure wave reaches the closed valve. Again, an unsteady condition exists as the flow is supposed to be zero at that

point. This causes a second wave reflection.

3. **Phase 3.** Since the fluid is still flowing from the pipe to the reservoir, the pressure drop across the wavefront will be negative. When the pressure wave reaches the inlet of the pipe at time $t = 3L/a$, the whole pipeline pressure has been reduced, and the fluid velocity would be zero. Similarly to phase 1, an unsteady pressure condition exists at the pipe's inlet because of the reservoir. However, the fluid must move through the pipe to the valve this time because H_0 is higher than the pipe pressure, inducing the third reflection.

4. **Phase 4.** The pressure wave travels down the pipe as the fluid flow. At time $t = 4T/a$, the wave reaches the valve position, and the same condition as phase 1 occurs. This means the process is repeated with a period of $4L/a$. However, the fluid's velocity will be lower than the initial velocity, C_i, due to the pipe's friction ([1]).

As previously mentioned, the water hammer effect is only generated when the valve is closed rapidly. The critical time of the valve closure corresponds to the time the overpressure reaches its maximum value, and it occurs at $2L/a$. This is because, during phase 1, the pressure in the pipe increases due to the flow velocity change. According to the Joukowsky equation, if the valve remains open when the pressure wave reaches the reservoir, the pressure in the pipe would be lower than the maximum pressure since the flow experiences a change in speed that is less than the largest speed variation (i.e., from C_i to zero). The wave is then reflected, causing a pressure drop in the pipe. However, at the end of the pipe, there is no knowledge of what is happening upstream, so the pressure continues to rise until the wave pressure reaches the end of the pipe. Therefore, the full water hammer effect is achieved if the valve is closed before the pressure wave undergoes the second reflection.

3.3.2 Modelling of the hydraulic system for water hammer study

The water hammer phenomenon is now simulated by using the electrical analogy presented in Chapter 2. To model the hydraulic elements in the system shown in Fig. 3.2, the following electrical components are used:

- the upstream reservoir is represented by a pressure (voltage) source H_0,
- the pipe is modelled by a series of I T-shaped RLC branches of length dx,
- the valve is represented as a variable resistance R_v.

The resulting equivalent scheme is shown in Fig. 3.4:

The full water hammer is simulated by closing the valve (i.e., increasing the value of R_v) faster than its critical time $t_{crit} = 2L/a$. The case study is a 600-meter-long pipe with an average wave speed of 1200 m/s. Fig. 3.5 shows the time evolution of the per unit values of the head at the valve (i.e., the head corresponding to the last penstock element h_I over its nominal value H_0) and the

[1] during the process, the wave speed could also change due to the changes in pressure that can cause cavitation and the reduction of the bulk modulus of the fluid, ultimately leading to a reduction in wave speed.

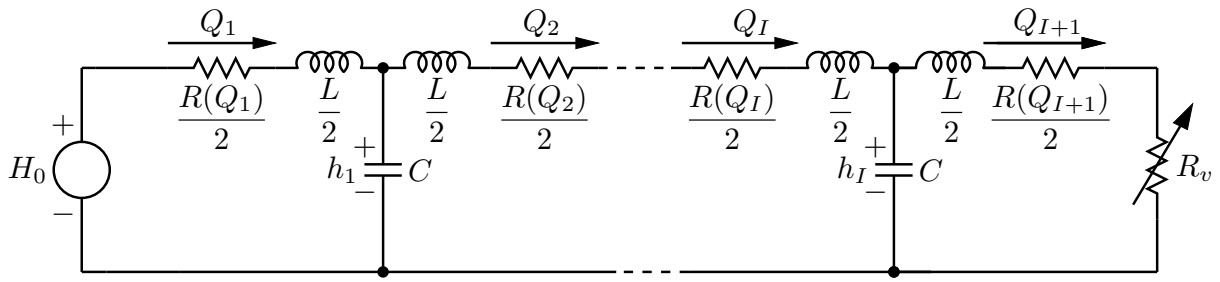

Figure 3.4: Equivalent electric circuit of Fig. 3.2

discharge at the valve Q_{I+1}/Q_0 resulting from a valve closure in 1 second. The valve starts closing at time $T_{start} = 1$ s and then is fully closed at $t = T_{start} + t_{crit}$. The discharge at the valve decreases to zero within the valve closure time while the head at the valve reaches its maximum amplitude of $3 \cdot H_0$ at the time $T_{start} + 2L/a$. The pressure wave propagates with a period of $4L/a$, reducing at each reflection due to the pipe's wall friction.

To conclude, water hammers can generate large pressure transients, potentially harming the penstock in the long run. Designing pipes that can withstand the maximum amplitude of water hammers for many cycles is expensive and impractical as they may require thick and heavy pipes. To mitigate the effects of water hammer pulses, surge tanks, accumulators, and other features are used to reduce the pressure transients. However, these features are not always included in the plant's layout.

The following section will discuss the methodology for evaluating the stress on penstocks due to pressure transients and estimating the fatigue.

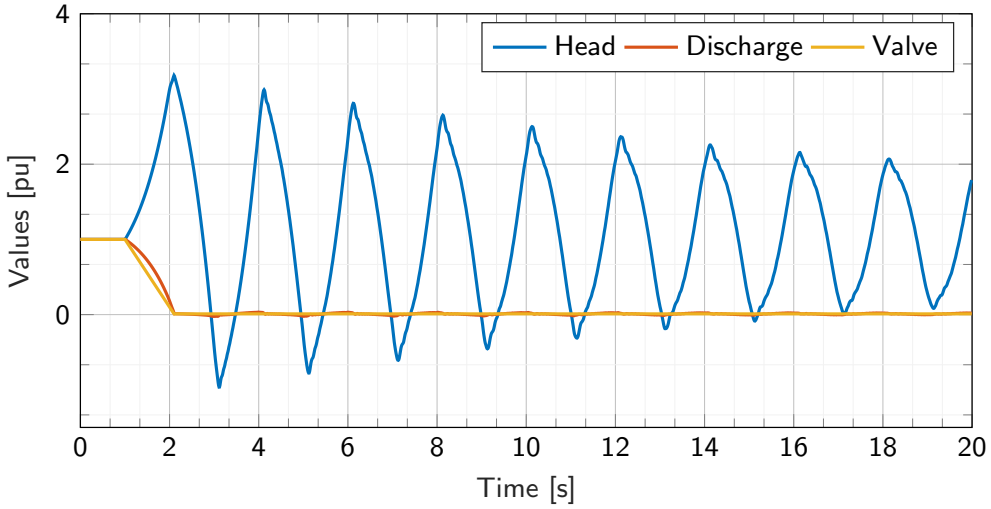

Figure 3.5: Time evolution in per-unit values of the head at the valve and the discharge at the valve resulting from a valve closure in 1s.

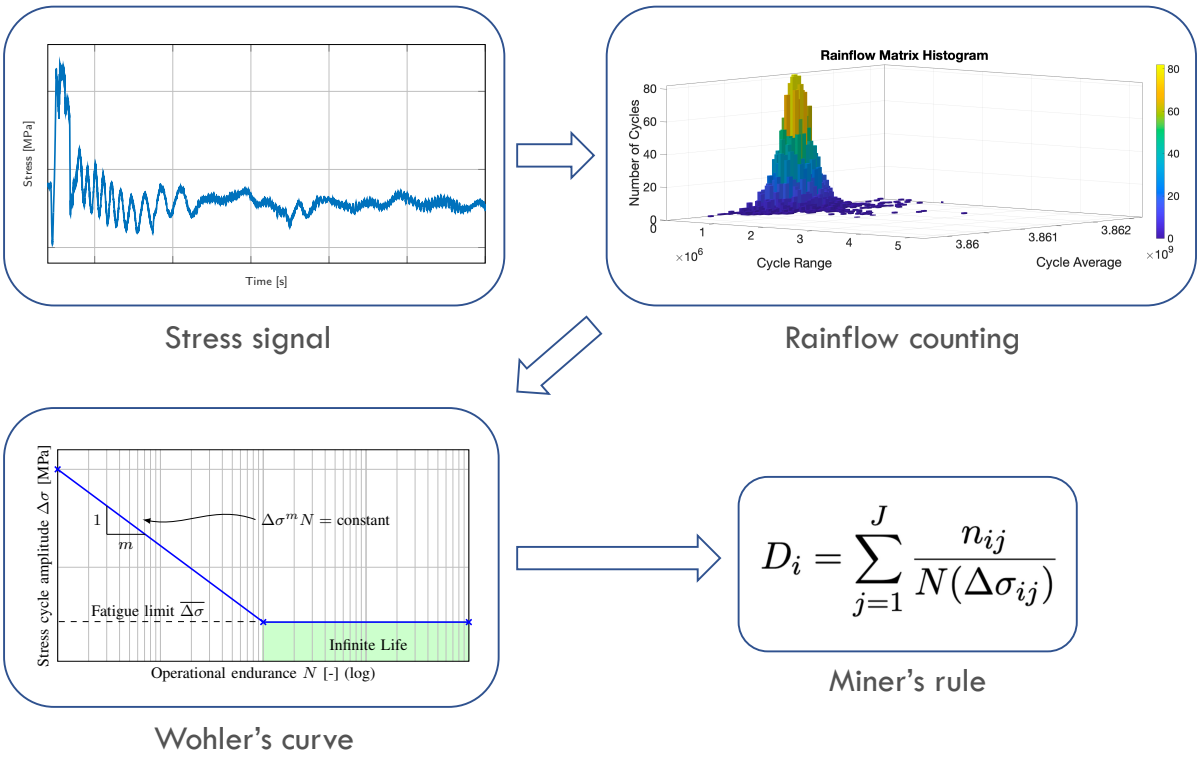

Figure 3.6: Methodology to assess the penstock damage from a stress signal history.

3.4 Evaluation of penstock fatigue

Fatigue is a failure mechanism that occurs to materials due to accumulated mechanical loads (or stress). Fatigue failures are typically sudden and hard to predict due to the variability of the loads, point of application, direction, etc. In material science, this phenomenon is also known as "crack growth". It is due to small imperfections in the material that grow over time, ultimately leading to ruptures because of mechanical loads [69–71]. Fatigue over time can be modelled using different approaches, as described next.

Fatigue and residual lifetime of a component can be modelled considering the number of cycles to failure for a specific loading level, typically determined empirically based on physical testing performed on the material specimen, e.g., [72]. This thesis assesses fatigue using the stress-life method based on Wöhler's curve, discussed later in this section. This method is used in applications where the applied stress is within the material's elastic range, and the material has a long cycle life (i.e., more than 10^4 cycles to failure), as for the penstock. The stress-life approach is widely adopted for fatigue evaluation due to its simplicity. It gives conservative lifetime estimates compared to other methods, such as crack propagation theory [73, 74], which will be considered in future works. However, as demonstrated hereafter, it provides an actionable way to determine operational patterns conducive to excess fatigue.

The penstock fatigue is estimated using the method reported in [16], shown in Fig. 3.6. It consists in the following steps:

1. evaluation of the penstock head, $h_i(t)$, at all penstock's elements, $i = 1, \ldots, I$;

2. conversion of the head to mechanical stress, $\sigma_i(t)$, using the model in [75]:

$$\sigma_i(t) = h_i(t) \cdot \frac{kD}{2e} \qquad i = 1, \ldots, I \tag{3.5}$$

   where D and e are the penstock diameter and wall thickness, respectively, and $k = g \cdot \rho$ converts from head H in meter to pressure p in pascal, with g the acceleration of gravity and ρ the water density in kg/m^3;

3. cycle counting of the mechanical stress with a rain-flow algorithm [76, 77]. For each penstock element, this algorithm provides J tuples $(\Delta\sigma_{ij}, n_{ij}), j = 1, \ldots, J$, one for each identified amplitude of stress cycle $\Delta\sigma_{ij}$, where n_{ij} is the number of cycles with stress amplitude $\Delta\sigma_{ij}$;

4. computation of the cumulative damage index, D_i, for each penstock element by applying Miner's rule [78]:

$$D_i = \sum_{j=1}^{J} \frac{n_{ij}}{N(\Delta\sigma_{ij})}, \qquad \text{for all } i \tag{3.6}$$

   where $N(\Delta\sigma_{ij})$ is the maximum number of cycles that the element can perform with a stress cycle of amplitude $\Delta\sigma_{ij}$; this value is given by the so-called SN, or Wöhler's curve (discussed in detail below). The cumulative damage index in (3.6) is used to approximate the residual life of a mechanical component. Values near 1 denote that the mechanical element is near to its end of life; zero, vice-versa.

The SN curve provides information on the number of cycles a mechanical component can perform for a given stress cycle. It is typically determined empirically and reported in technical standards, such as the BS7910 for welded structures made of steel [79], including penstocks. The curves are classified into different quality categories based on specific fatigue design requirements or the presence of flaws in the material. An example of an SN curve is presented in Fig. 3.7. The Basquin equation describes the initial log-linear trend of the curve:

$$\Delta\sigma^m N = \text{constant}, \tag{3.7}$$

where m represents the log-linear slope, indicating that the number of cycles increases as stress levels decrease. For ferrous materials, such as the steel alloys used in penstocks, a fatigue limit ($\overline{\Delta\sigma}$ in Fig. 3.7) is observed after the log-linear trend, below which the number of cycles drastically increases.

Developing on the fatigue limit of the penstock is the key notion leveraged in this chapter to reduce fatigue, as formally explained in the next section. It should be noted that identifying the SN curve is not within the scope of this analysis. It is assumed to be provided by a plant specialist based on detailed knowledge of the penstock and plant.

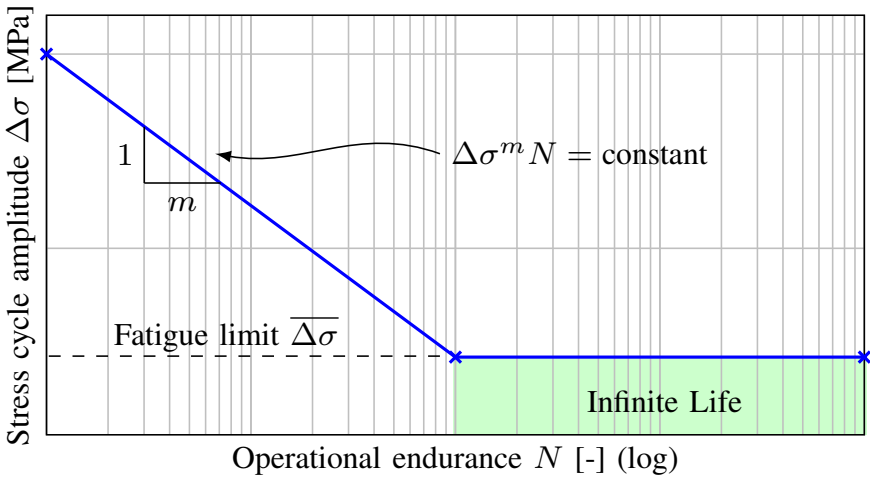

Figure 3.7: Example of SN curve of a ferrous material.

3.5 Model predictive control for fatigue reduction

This section proposes a receding horizon model predictive control strategy to reduce mechanical fatigue in the penstock of medium- and high-head HPPs. Fig. 3.8 shows the implementation of the MPC (the yellow block) in the control system of a medium-head HPP. Let $y^\star$ be the guide vane set-point determined by the turbine governor as a function of the plant regulation duties (the computation of $y^\star$ is described in detail in Section 1.2.2). As $y^\star$ might be unaware of the accumulated effects due to fatigue, we want to find a new guide vane set-point that respects the fatigue limit of the penstock.

The MPC takes the guide vane set-point from the governor as its input and generates a new guide vane opening, y^o, that satisfies two requirements:

1. it should not result in mechanical loads engendering fatigue;
2. it should be as close as possible to the reference guide vane opening, $y^\star$, to maintain the original regulation duties of the plant and avoid economic penalties or disqualification from regulation services.

As discussed in the previous chapter, the mechanical loads in the penstock and the resulting stress are formulated with linear models that capture the water pressure dynamics within the conduits. Utilizing these models makes the problem convex and can be solved with real-time requirements.

3.5.1 Fatigue constraint as a linear function of the plant's set-point

The stress is constrained within a specific interval to ensure that stress variations do not exceed the fatigue limit. Formally, this reads as:

$$\sigma_{\text{nom}} - \frac{\overline{\Delta\sigma}}{2} \leq \sigma_i(t) \leq \sigma_{\text{nom}} + \frac{\overline{\Delta\sigma}}{2} \tag{3.8}$$

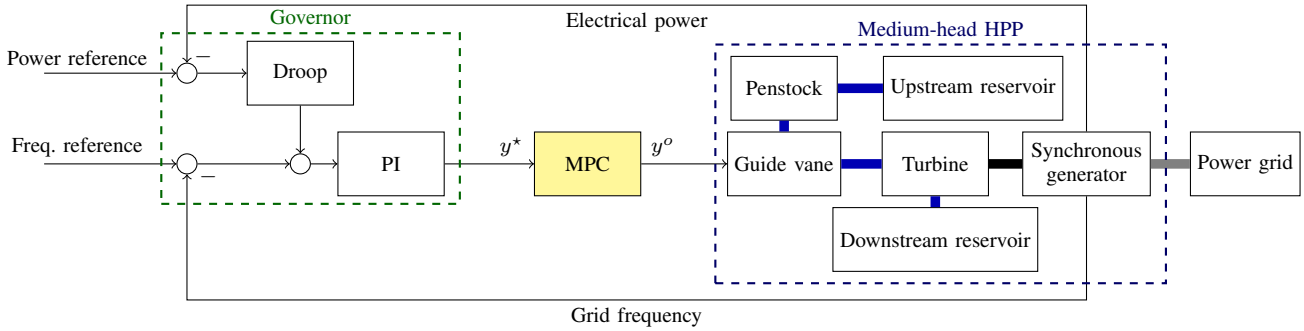

Figure 3.8: MPC implementation in the control system of a medium-head HPP. The MPC (the yellow block) receives the guide vane set-point from the governor, $y^\star$, and produces a new signal, y^o, with the desired properties described in the text.

where $\sigma_i(t)$ is the stress on the penstock element i at time t, σ_{nom} is the nominal stress (i.e., the stress during nominal operating conditions of the plant), and $\overline{\Delta\sigma}$ is the fatigue limit. It can be verified that under (3.8), the largest stress amplitude that can occur is:

$$\sigma_{\text{nom}} + \frac{\overline{\Delta\sigma}}{2} - \left(\sigma_{\text{nom}} - \frac{\overline{\Delta\sigma}}{2}\right) \leq \overline{\Delta\sigma} \;\Rightarrow\; \overline{\Delta\sigma} \leq \overline{\Delta\sigma} \tag{3.9}$$

thus attaining the requirement of operating below the fatigue limit.

The stress inequalities (3.8) can be represented using the linear relationship between penstock head and stress in (3.5). By doing so, the constraints can be expressed as:

$$\underline{h} \leq h_i(t) \leq \overline{h} \tag{3.10}$$

where the upper and and lower bounds of the head are

$$\underline{h} = \frac{\sigma_{\text{nom}} - \overline{\Delta\sigma}/2}{k \cdot D/2e} \tag{3.11}$$

$$\overline{h} = \frac{\sigma_{\text{nom}} + \overline{\Delta\sigma}/2}{k \cdot D/2e}. \tag{3.12}$$

The penstock head is calculated using the linearized state-space model in (2.30) as a function of the state and control history. For instance, the one-step-ahead prediction of the penstock head at time t can be expressed as a linear combination of the state vector $\boldsymbol{x}(t)$, the control input $y(t)$, and an auxiliary input vector $\boldsymbol{z}(t)$, as:

$$h_i(t+1) = C_i \left(A\boldsymbol{x}(t) + B_y y(t) + B_z \boldsymbol{z}(t)\right), \tag{3.13}$$

where $C_i \in \mathbb{R}^{1\times(2I+1)}$ is an output matrix properly designed to extract h_i from the state vector, and A, B_y, B_z are discrete-time state-space matrices obtained by discretizing (2.30).

Equations (3.10) and (3.13) are the building blocks used in the next paragraph for the formulation of the MPC optimization problem. As it will be explained next, the need to include predictions in the problem, as in (3.13), stems from hydraulic dynamics that determine transients of mechanical loads within the penstock.

3.5.2 Formulation of the MPC problem

Assuming to be at time interval t, the new guide vane set-point is found by solving the following optimization problem:

$$\boldsymbol{y}^o = \underset{\boldsymbol{y}\in\mathbb{R}^{T+1}}{\arg\min} \left\{ \sum_{\tau=t}^{t+T} \left(y(\tau) - y^\star(\tau)\right)^2 \right\} \tag{3.14a}$$

subject to guide vane limits

$$0 \leq y(\tau) \leq 1, \qquad \tau = t, \ldots, t+T \tag{3.14b}$$

and penstock model and stress constraints, starting from a known initial condition $x(t)$:

$$h_i(\tau+1) = C_i \left(A\boldsymbol{x}(t) + B_y y(t) + B_z \boldsymbol{z}(t)\right) \tag{3.14c}$$

$$\underline{h} \leq h_i(\tau) \leq \overline{h} \tag{3.14d}$$

for the whole optimization horizon $\tau = t, \ldots, t+T$ and all the penstock's elements $i = 1, \ldots, I$.

The two requirements of the previous section are formulated in a constrained optimization problem. The first requirement (fatigue limit) is formulated using the linear inequalities discussed in the former paragraph. The second requirement can be expressed in the sense of distance minimization between $y^o(t)$ and $y^\star(t)$.

The head within the penstock is a dynamic quantity that responds to differential equations, implying that a control decision at a certain time instant influences the head in the future ([2]). To account for these dynamics, formulating stress constraints for the penstock necessitates estimating future values of the head, motivating a predictive approach.

Therefore, the MPC is solved in a receding horizon manner, meaning that the problem is solved for the entire horizon $t+T$ at time t, and only the first element of the decision vector is implemented, disregarding the remaining elements. This process is repeated at each time interval, and the linearization of the model is updated to reflect changes in the plant's operational conditions.

The selection of the look-ahead time T is based on the concept that a change in the set-point at time t will no longer affect the system state after a certain time. This criterion provides a formal means of selecting the value of T and can be determined analytically.

The optimization problem in Eq. (3.14) is convex, owing to the linearized constraints of the HPP, and can be efficiently solved using standard optimization libraries for convex optimization. The description of how to formally write the MPC problem is provided in Appendix C. A performance analysis of the computational efficiency of the methodology is presented in Section 3.6.5.

It is important to note that, when solving the optimization problem, the set-points $y^\star(t+1), \ldots, y^\star(t+T)$ in (3.14a) are not known because they refer to future time intervals. Therefore, they are replaced with persistence predictions, which assume that future values are the same as the current realization (i.e., $y^\star(t+\tau) = y^\star(t), \tau = 1, T$). This approach is motivated by the

[2] head dynamics can also be interpreted in the light of the water hammer effect: suddenly closing the guide cause the water to slow down and a shock wave, which travels at a finite speed inside the penstock (thus head variations) and is reflected back and forth between the guide vane and reservoir until dissipated.

difficulty in accurately forecasting grid frequency deviations, on which the guide vane depends. However, persistence predictions yield satisfactory performance and successful stress reduction, as demonstrated in Section 3.6.6.

3.6 Performance evaluation of the MPC

3.6.1 Case study

The case study used to validate the performance of the MPC is a 230 MW medium-head HPP with a net-head of 315 meters equipped with one Francis turbine, an open-air 1100 meter-long penstock, and main characteristics as in Table 3.1. The plant is equipped with the standard governor shown in Fig. 3.8, which includes a Proportional-Integral (PI) regulator with a speed droop and set-point for speed-changer setting. The PI gains are determined using the Ziegler-Nicholas method. The governor performance complies with the ENTSOE qualification tests for PFC [41] (see Appendix A). The regulator has limits for the rate-of-change and magnitude of the guide vane actuator. The permanent speed droop is set to 2%. Compared to conventional speed droops for HPPs that are between 2.5% and 5%, we choose a lower value to reproduce future operational settings where larger flexibility might be required from dispatchable resources.

The plant is modelled with the non-linear model discussed in Chapter 2. The penstock is discretized in $I = 20$ elements, sufficient to accurately represent the hydraulic transients. The synchronous generator torque is modelled as a second-order model, with the electrical torque function of the generator's power angle, as described in Section 2.4.3. Rotor dynamics are simulated with the swing equation. The grid is modelled as an infinite bus, where the rest of the power system imposes the grid frequency under the assumption that its size is significantly larger than the simulated plant. Grid frequency variations are reproduced considering real system frequency measurements of the European interconnected system from [80].

Table 3.1: Parameters of the HPP case study

Parameter	**Unit**	**Value**
Nominal power	MW	230
Nominal head	m	315
Nominal discharge	m^3/s	85.3
Nominal speed	rpm	375
Nominal torque	Nm	5.86×10^6
Length of penstock	m	1'100
Diameter of penstock	m	5
Wave speed	m/s	1'100

3.6.2 Methodology for the numerical simulations

The simulation procedure is summarized in Fig. 3.9. At each time step, the grid frequency value is read from a measurement list and used to compute the guide vane set-point, $y^\star$, with the HPP governor. Then, a linearized HPP model is computed considering the plant's current working point and used in the MPC to find the new guide vane set-point, y^o. The non-linear plant model is subsequently employed to calculate the head and stress values in the penstock, which are combined with the SN curve to estimate the damage index, defined in the next section. The state-space matrices are discretized using the 4th order Runge-Kutta method, and the MPC look-ahead time horizon T is set to 2 seconds.

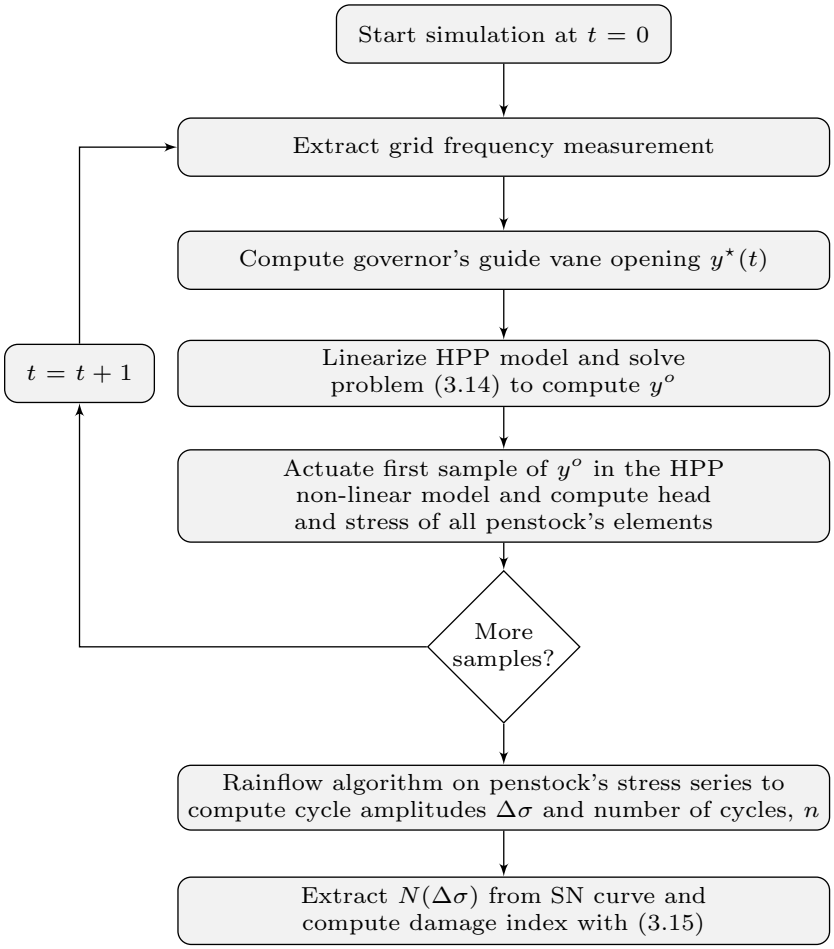

Figure 3.9: Procedure for the numerical simulations.

The fatigue analysis involves using the SN curve characteristics outlined in Table 3.2, corresponding to quality category Q5 as defined in [79]. In order to prevent optimistic outcomes and account for empirical uncertainties of the penstock fatigue limit, a change in the log-linear slope (from 3 to 5, as indicated in Table 3.2) is modelled after the fatigue limit is reached, rather than an infinite number of cycles as illustrated in Fig. 3.7.

Table 3.2: Parameters of the SN curve

Parameter	Unit	Value
Basquin equation (3.7)'s slope m	-	3
Effective fatigue limit $\overline{\Delta\sigma}$	MPa	23
Basquin equation's slope m after $\overline{\Delta\sigma}$	-	5

3.6.3 Performance metrics

MPC performance is assessed in terms of incurred penstock damage, measured with the damage index in (3.6). A convenient approach for measuring performance is comparing it to a base case where the MPC is not used, corresponding to the plant's classical configuration. In this configuration, the guide vane reference $y^\star$ in Fig. 3.8 serves as the input, bypassing the MPC. The Relative Damage Index (RDI) is defined for each penstock element i as:

$$\mathrm{RDI}_i = \frac{D_i^{(\mathrm{MPC})}}{\max_i \left(D_i^{(\text{base case})} \right)}, \tag{3.15}$$

where $D_i^{(\mathrm{MPC})}$ and $D_i^{(\text{base case})}$ are the damage indexes achieved with MPC and in the base case, respectively. In (3.15), the reason for dividing by the maximum damage index along the penstock instead of the damage index at i is to avoid that small values of the damage index in certain penstock segments (thus, with negligible impact on the fatigue) generate large value (but insignificant) performance improvements.

A second metric involves comparing the performance of different controllers (described in Sections 3.6.4 and **??**) in terms of their ability to track the original guide vane set-point $y^\star$ and preserve the original regulation effort.

Pearson's Correlation Coefficient (CC) is used to measure the similarity between y and $y^\star$ [81]:

$$\mathrm{CC} = \frac{\mathrm{cov}(y, y^\star)}{\sqrt{\mathrm{var}(y)}\sqrt{\mathrm{var}(y^\star)}}. \tag{3.16}$$

The coefficient ranges from -1 to +1, where -1 indicates anticorrelation, 0 no correlation, and 1 perfect correlation between the signals.

3.6.4 Benchmark controller: linear low-pass filter

In order to reduce fatigue, a commonly suggested solution in the literature is to employ a low-pass filter to preprocess the grid frequency signal that feeds the governor to avoid frequent variations of the guide vane set-point, as proposed in [52]. The parameter that needs to be determined in this approach is the LPF's cut-off frequency. Small cut-off frequencies would significantly smooth out the input grid frequency, thereby reducing damage and decreasing the plant's regulation response. Conversely, high cut-off frequencies preserve the regulation response but fail to achieve damage reduction. The choice of the cut-off frequency can be made empirically based on numerical simulations, for instance. For this performance comparison, a first-order linear low-pass filter is used. As

discussed in the next section, this filter's cut-off frequency is determined to achieve the same regulation performance as the MPC, enabling a fair comparison of the fatigue reduction performance between the two approaches.

3.6.5 Results

This section describes the results of applying the MPC to the output of the HPP governor (see Fig. 3.8) and computing a new guide vane set-point that respects the penstock's stress constraints. The MPC's set-point is computed by solving the optimization problem in Eq. (3.14), and the reference guide vane opening determined by the HPP governor is compared to the MPC's guide vane set-point.

The top panel of Fig. 3.10 shows the reference guide vane opening $y^\star$ (blue line) determined by the HPP governor and the one computed by the MPC y^o (dashed red line). These two signals are nearly identical, except for a few cases, as will be soon described. The bottom panel of Fig. 3.10 compares the head in the penstock's most critical element resulting from applying the two set-points and the head limits (dashed lines).

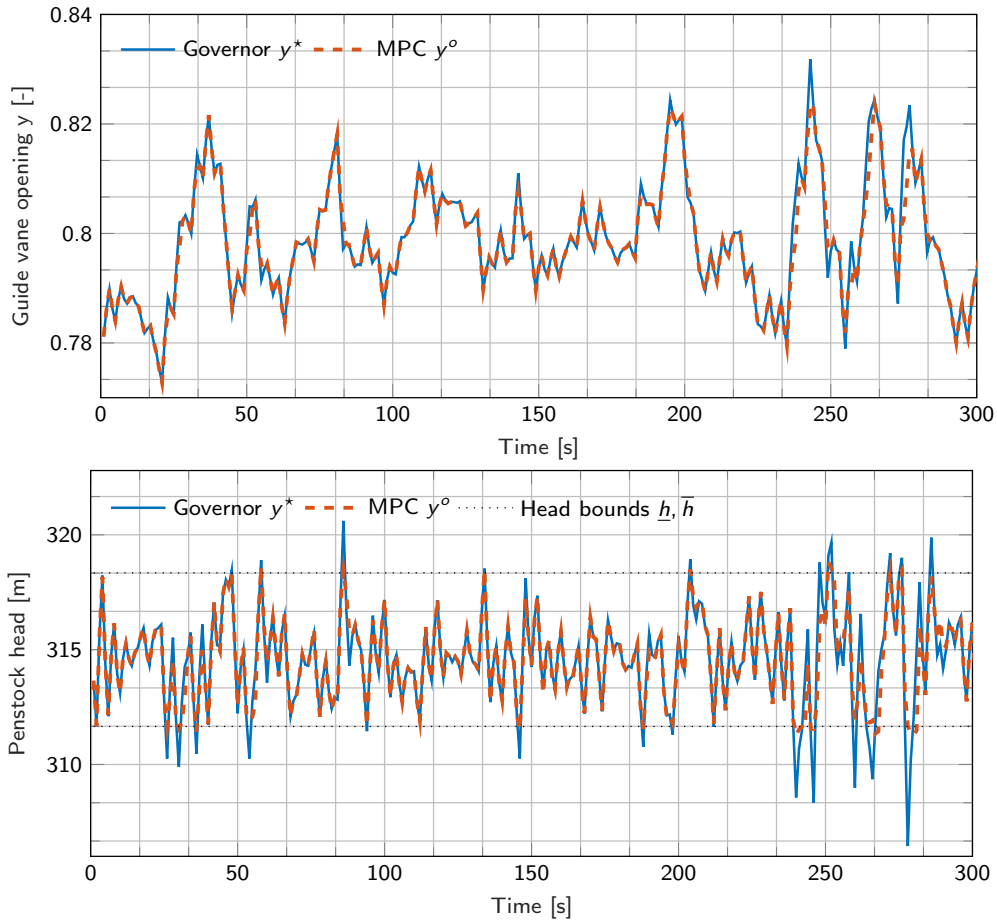

Figure 3.10: Set-point actuated by the governor and MPC (top panel) and respective head (bottom panel).

By looking at the top and bottom panels of Fig. 3.10, it can be seen that when the original set-point $y^\star$ does not engender violations of the head limits, the MPC set-point y^o is identical to $y^\star$. This follows directly from the formulation of the optimization problem in (3.14): in particular, when the head constraints in (3.14d) are not activated, the problem is unconstrained; its optimal solution happens when $y^\star$ equals y^o. However, when constraints become active, the optimization problem needs to satisfy the stress constraints and produces a set-point y^o which differs from $y^\star$.

Fig. 3.11 shows a zoomed view of the guide vanes of the top panel of Fig. 3.10 when the head limits are exceeded, and it can be observed that the control action of the MPC resembles a rate limiter. We can thus conclude that filtering mechanisms based on low-pass filtering might be uneffective for fatigue reduction.

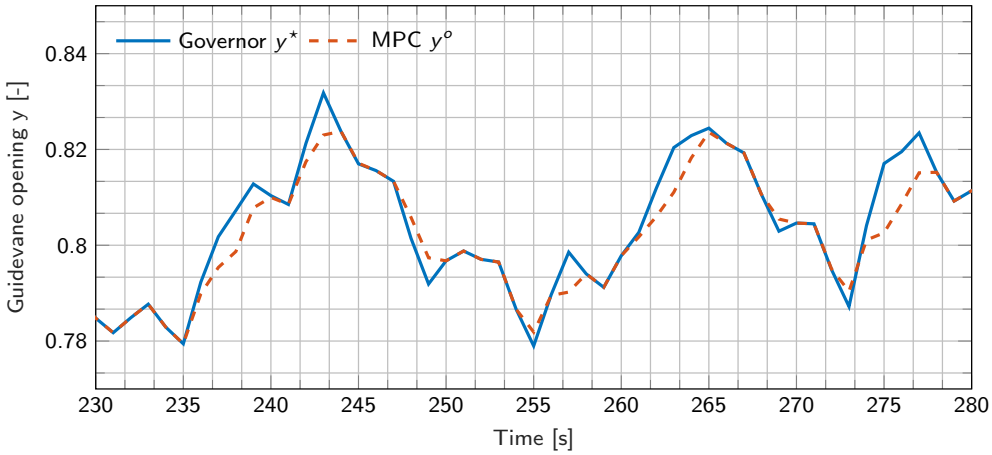

Figure 3.11: MPC actuated guide vane set-point

Fig. 3.12 compares the linear head estimates and the ground-truth ones simulated with a non-linear model. The relative mean absolute error of the linear estimates is less than 1% in the range of variations of the guide vane input of a ± 0.05 pu.

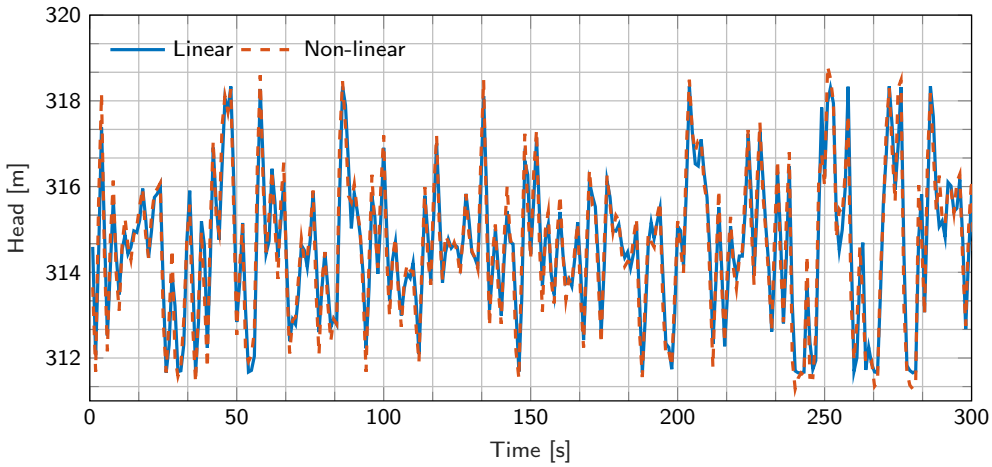

Figure 3.12: Comparison between linear and non-linear head in the critical portion of the penstock.

The MPC's convex optimization problem was computed with an average execution time of 22 milliseconds and a standard deviation of 5 milliseconds on a laptop with an Intel 5 processor. As the guide vane control action is updated each second, these metrics denote that the problem can be solved with real-time requirements with reasonable margins and, thus, is suitable to be implemented in real-life controllers.

3.6.6 Performance comparison against benchmark controllers

The evaluation of the performance of the controllers involves two key metrics, namely i) the reduction of the RDI as defined in (3.15), and ii) the ability of the controllers to track the original regulation signal for primary frequency control, quantified using the CC metric defined in (3.16).

Fig. 3.13 shows the RDI along the penstock. As discussed in Sec. 3.6.1, the penstock is discretized in 20 elements, and the damage is evaluated for each of these elements individually. It can be seen that the most damaged penstock element is the fifth one, corresponding to a position along the penstock of 200 meters from the upper reservoir.

The performance of the MPC against the low-pass filter and the fatigue-aware filter (described in Appendix B) are now discussed.

Low-pass filter versus MPC. We set the cut-off frequency of the LPF to 1.46 Hz to achieve a comparable level of performance to MPC, as measured by the CC metric. The results show that the LPF effectively reduces RDI, as illustrated in Fig.3.13. However, for the penstock segments between 200m and 400m with the highest damage values, the MPC outperforms the LPF, as shown in Fig.3.13 and summarized in the first two entries of Table 3.3. Specifically, MPC achieves a nearly 43% reduction in RDI compared to the LPF with the same level of performance as measured by the CC metric.

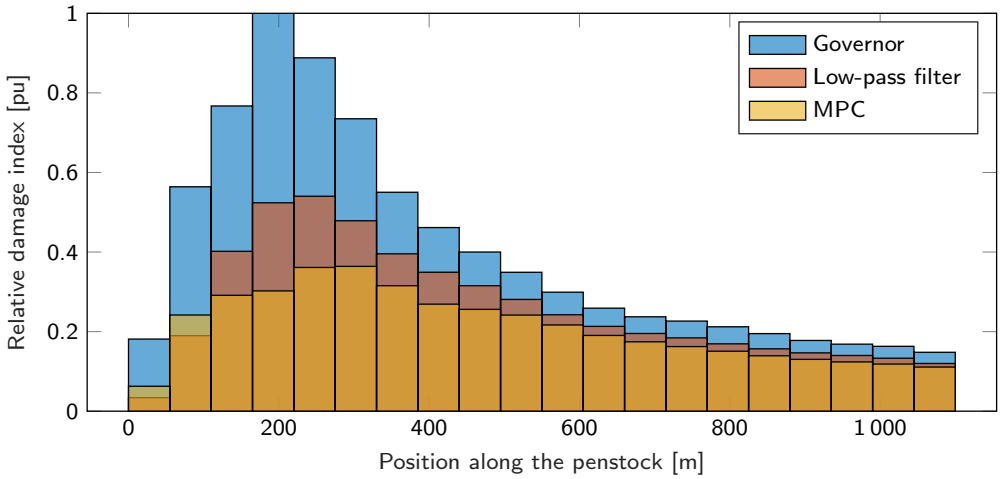

Figure 3.13: RDI along the penstock for the original governor, low-pass filter and MPC.

Fatigue-aware filter versus MPC. Both the fatigue-aware filter and the MPC are designed to prevent stress cycles above the fatigue limit, and thus inherently provide similar fatigue reduction

performance. This can be observed in Fig. 3.14, where both controllers demonstrate a comparable reduction in the RDI. Therefore, the comparison between the two controllers is based on their respective capacity to track the original regulation signal for primary frequency control, as quantified by the correlation coefficients presented in the last two entries of Table 3.3. The results show that the MPC outperforms the fatigue-aware filter in terms of regulation performance, achieving better tracking of the original regulation signal for the same level of damage reduction.

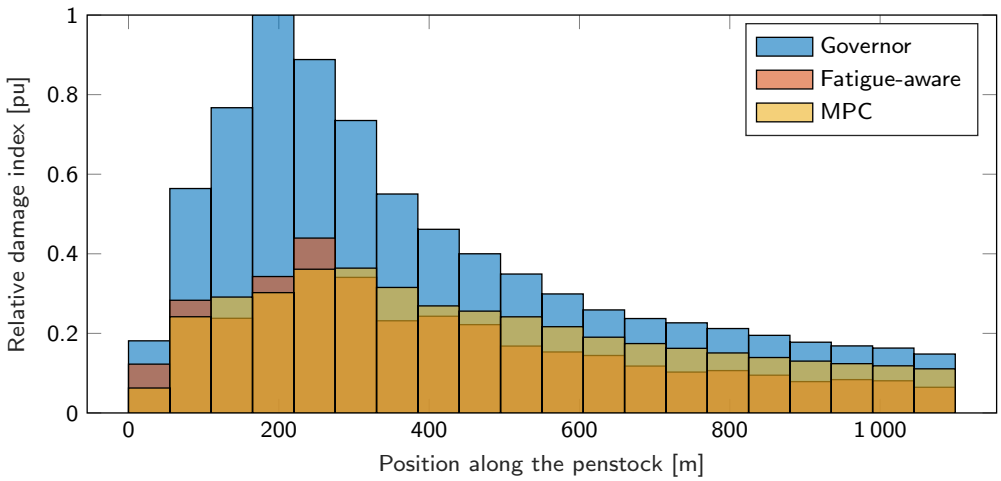

Figure 3.14: RDI along the penstock for the original governor, fatigue-aware filter and MPC.

Table 3.3: Summary of controller performances

Type of controller	**CC**	**RDI (5th penstock element)**
Low-pass filter	0.9948	0.53
MPC	0.9948	0.30
Fatigue-aware filter	0.9128	0.34

3.7 Extension to control of hybrid hydropower plants

The MPC described above computes a control trajectory for the guide vane so as to reduce the mechanical stress engendered in the penstock by way of explicit stress constraints. This section describes how this method is extended to derive a fatigue-informed controller for a HPP hybridised with a BESS.

As described in Chapter 1 (Fig. 1.5), the control problem of a hybrid hydropower plant consists in computing two set points, one for the HPP and the other for the BESS, starting from the plant's global set-point. This problem was defined as the set-point splitting problem.

3.7.1 Problem formulation

The design requirement adopted in this chapter to solve the set-point splitting problem is that the hybrid power plant should provide the same regulation performance as the HPP controlled with the guide vane from the original plant governor. In other words, we seek to provide the same regulation performance while achieving stress reduction in the penstock. Under this requirement, the battery power set-point, $B^{\dagger}(t)$, can be computed as:

$$B^{\dagger}(t) = P^{\star}(t) - P^{\dagger}(t), \tag{3.17}$$

where $P^{\star}(t)$ and $P^{\dagger}(t)$ are, respectively, the HPP's power output with the original guide vane $y^{\star}$ and the modified guide vane $y^{\dagger}$ from the MPC .

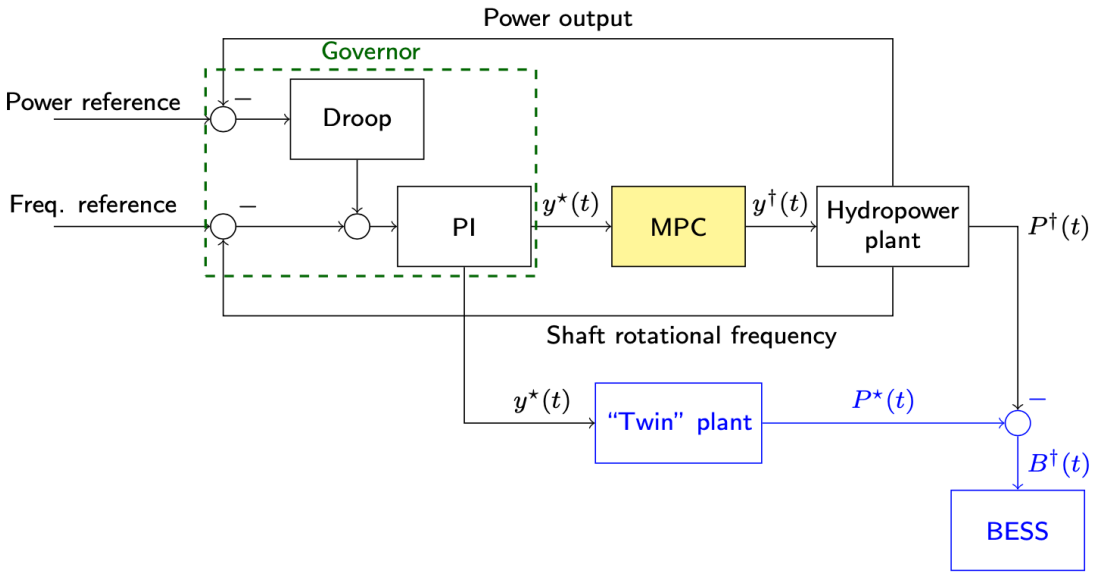

Figure 3.15: Battery power set-point estimation.

However, while the latter quantity could be accessed, e.g., from measurements because it is physically realized, the former power output is not available because it is unrealized, being the original control set-point never implemented. Consequently, the direct computation of the BESS power set-point as in (3.17) is not feasible. To overcome this limitation, we propose to estimate the unrealized power output using an estimation model, as illustrated in Fig. 3.15 and explained below.

The approach involves using a guide vane-to-power linear model, referred to as the "Twin" plant block in Fig. 3.15, to estimate the power output with the original guide vane set-point. This estimation is denoted by $\hat{P}^{\star}$ and is [3]:

$$\hat{P}^{\star}(t) = \hat{T}^{\star}(t) \cdot \hat{\omega}^{\star}(t), \tag{3.18}$$

[3]the $\hat{\cdot}$ notation refers to estimated quantities, as opposed to measured ones.

where $\hat{T}^\star$ and $\hat{\omega}^\star$ are the hydraulic turbine's torque and angular velocity. Since the frequency in power grids is regulated to a nominal value (e.g., 50 Hz) and we consider a small signal context for this control model where variations are small within a control cycle with linearization recomputed for new conditions, we assume the grid frequency to be constant and the generator synchronized to the grid and with unitary efficiency, yielding the following approximation:

$$\hat{P}^\star(t) = \hat{T}^\star(t) \cdot 2\pi \cdot \frac{f_n}{\rho}, \tag{3.19}$$

where f_n is the nominal grid frequency and ρ the polar couples of the electric generator. The modelling approximations and assumptions that have been introduced for the MPC (i.e., linear HPP model, constant grid frequency and synchronized generator) are validated by testing the control output of the MPC with simulation models that include swing equation and generator models.

Since the angular velocity of the generator is assumed to be constant, estimating the HPP power in (3.18) reduces to estimating the torque of the hydraulic turbine in (3.19). To estimate the torque, the linearized model (2.29) discussed in Chapter 2 is used. In the subsequent formulation, the linear estimates of the torque as a function of the guide vane are represented as $z(y(t))$ [4]. With this notation, the estimated power in (3.18) can be expressed as:

$$\hat{P}^\star(t) = z(y^\star(t)) \cdot 2\pi \cdot \frac{f_n}{\rho}. \tag{3.20}$$

Eq. (3.20) can be utilized to estimate the first term on the right-hand side of (3.17). However, the second term, $P^\dagger(t)$, may only be obtained from measurements, which results in a delay since the power output of the plant for the presently implemented guide vane $y^\dagger(t)$ is not yet available. Instead of relying on delayed measurements, one can use model (3.20) to estimate $P^\dagger(t)$, yielding:

$$\hat{P}^\dagger(t) = z(y^\dagger(t)) \cdot 2\pi \cdot \frac{f_n}{\rho}. \tag{3.21}$$

By combining (3.17), (3.20), and (3.21), we can derive the BESS set-point as follows:

$$B^\dagger(t) = \left[z(y^\star(t)) - z(y^\dagger(t))\right] \cdot 2\pi \cdot \frac{f_n}{\rho}, \tag{3.22}$$

which is proportional to the difference between the linear estimates of the torques under the original and MPC guide vanes. Compared to using delayed measurements, the method in (3.22) has the advantage that if the two guide vane set-points are similar (as we would expect in a small signal context), the modelling error of the linear torque model $z(\cdot)$ cancels out.

Finally, the hybrid controller operates as following:

1. recent measurements are utilized to compute the linearized models $f(\cdot)$[5] and $z(\cdot)$ for the penstock head and turbine torque.;

[4] where other model parameters and variables are not reported.

[5] the head as a linear function of the guide vane is here denoted as $h_i(y(t)) = f_i(y(t))$.

2. the MPC problem in (3.14) is solved, using the target guide vane $y^\star$ from the governor as an input to the problem and the plant model $f(\cdot)$, thereby making available $y^\dagger$ for the current time interval;

3. the BESS injection is computed using $y^\star$, $y^\dagger$, and the turbine torque model $z(\cdot)$ with (3.22).

It is important to note that the BESS injection must be adjusted properly to ensure that it respects the four-quadrant power converter (e.g., [82]) and battery operational constraints. These requirements, along with the reactive power contribution of the power converter and energy management of the battery system, are not considered at this stage, as our focus is on evaluating the global BESS power injection and comparing it with the power output of the HPP to determine the required BESS power.

It is worth highlighting that due to the hierarchical structure of the controller (i.e, first the MPC is solved, then the battery set-point is calculated), the linearity of the models involved in (3.22) is not a strict requirement for the tractability of the problem as this would not impact on the convexity of the MPC's optimization problem. This implies that more complex simulation models or digital twins (e.g., [83]) can be used to replace the linear estimates of the turbine's speed and torque, and HPP power. Moreover, there are multiple ways to integrate the MPC for fatigue reduction in (3.14) with the BESS injection model (3.22), including the incorporation of new constraints into the MPC formulation to model BESS injections and its constraints.

3.7.2 Results

This section illustrates the operations of a conventional HPP compared to its hybrid counterpart. Simulations are conducted over a day and refer to the case study in Section 3.6.1, where the HPP provides primary frequency control to the grid. Due to space constraints, the results are presented for a brief interval of the simulation duration. However, the conclusions remain valid for the entire period.

The upper panel of Fig. 3.16 shows the guide vane set-point of the standard governor and of the MPC. These set-points are mostly identical because the MPC is designed to achieve the same regulation duties as the original governor when penstock contraints are not active. However, when the governor's guide vane violates the head limits and constraints become active, the MPC produces a set-point that deviates from the original one, ensuring that the penstock head remains within the prescribed limits, as shown in the middle panel of Fig. 3.16.

The lower panel of Fig. 3.16 shows the contributions of the BESS, which operates only when the head constraints are active, as expected from the formulation. Notably, the BESS power is several MWs, which is small compared to the plant's power output of approximately 80 MW. This suggests that a relatively small battery injection is adequate to achieve the problem objectives.

Fig. 3.17 offers a zoomed view of the guide vanes and head constraints. In the bottom panel plot of Fig. 3.17, the head after the MPC action (dashed line) presents slight violations of the head constraints, which are due to the estimation error of the head linear model.

Fig. 3.18 shows the power output of three cases, namely:

1. the HPP operated with the original guide vane set-point ($P^\star$),

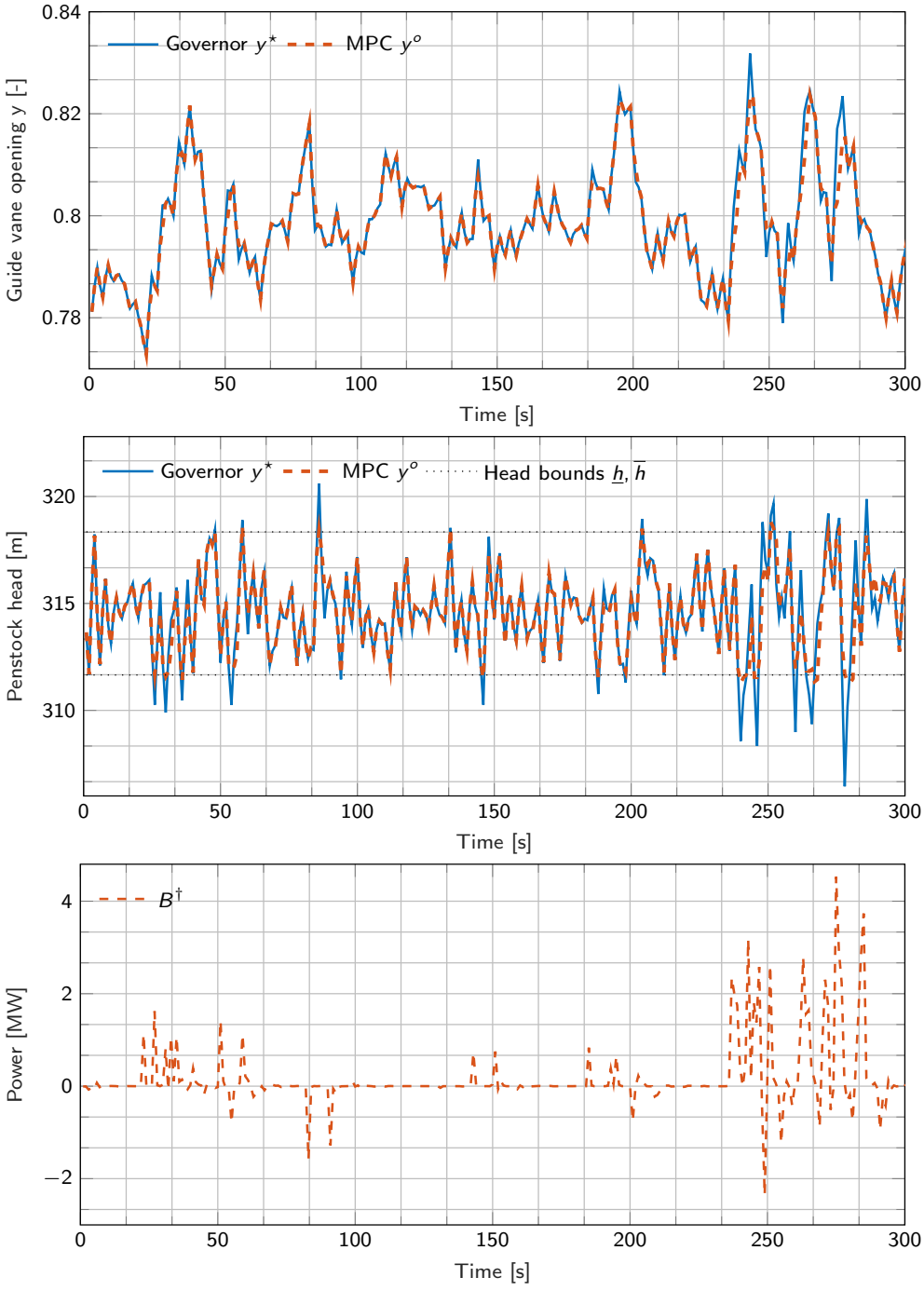

Figure 3.16: Governor guide vane versus the MPC one (in the upper panel), head of the penstock's critical element under governor and MPC control and head constraints (middle panel), battery power (lower panel).

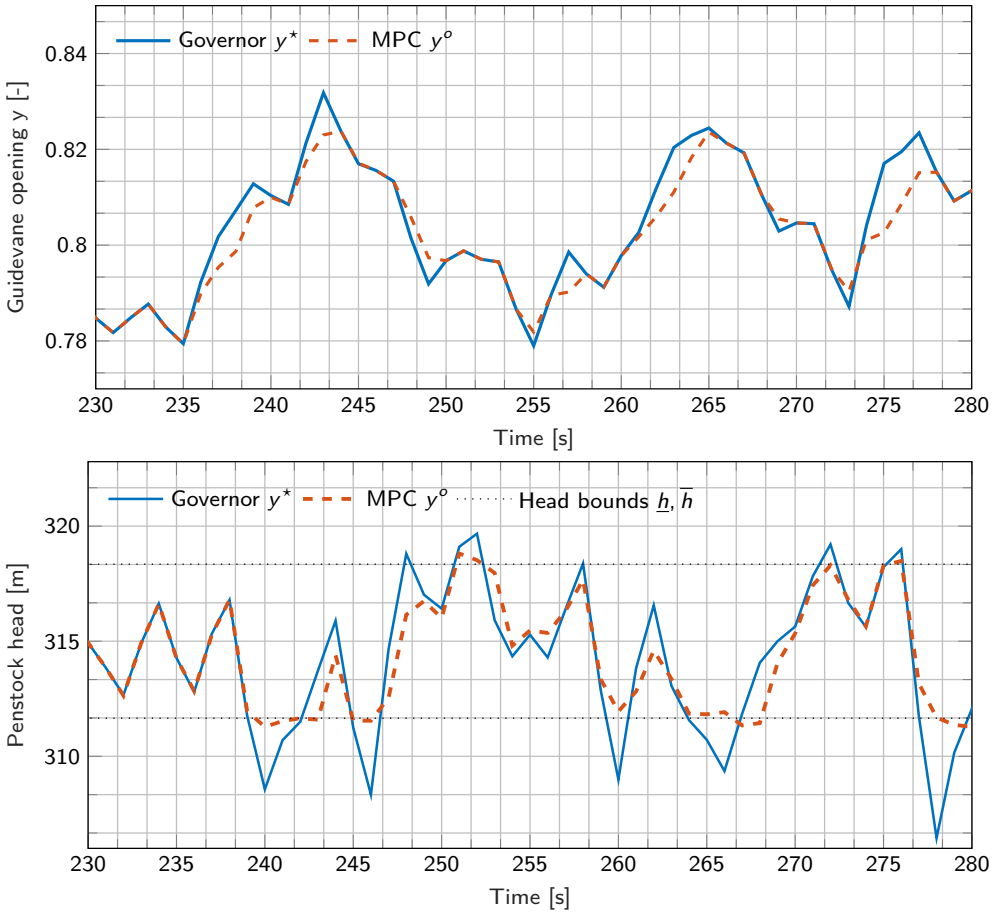

Figure 3.17: A zoomed view of Fig. 3.16 (line styles and colors are the same as there). When the head limits are violated (bottom panel), the MPC corrects the guide vane (upper panel) so as to respect them.

2. the HPP controlled by the MPC ($P^\dagger$) and,

3. the power output of the hybrid plant, given by the sum of the HPP's and BESS's contributions ($P^\dagger + B^\dagger$).

$P^\star$ is intended as a reference for the regulating power that the HPP should have provided in the original setting. It can be noticed that, while the HPP under MPC control does not track the reference power output, thus not providing the same regulating power, the hybrid plant closely tracks it. Therefore, it can be concluded that the requirement of controlling the battery to ensure that the hybrid HPP attains the same power regulation capacity as the original HPP has been fulfilled.

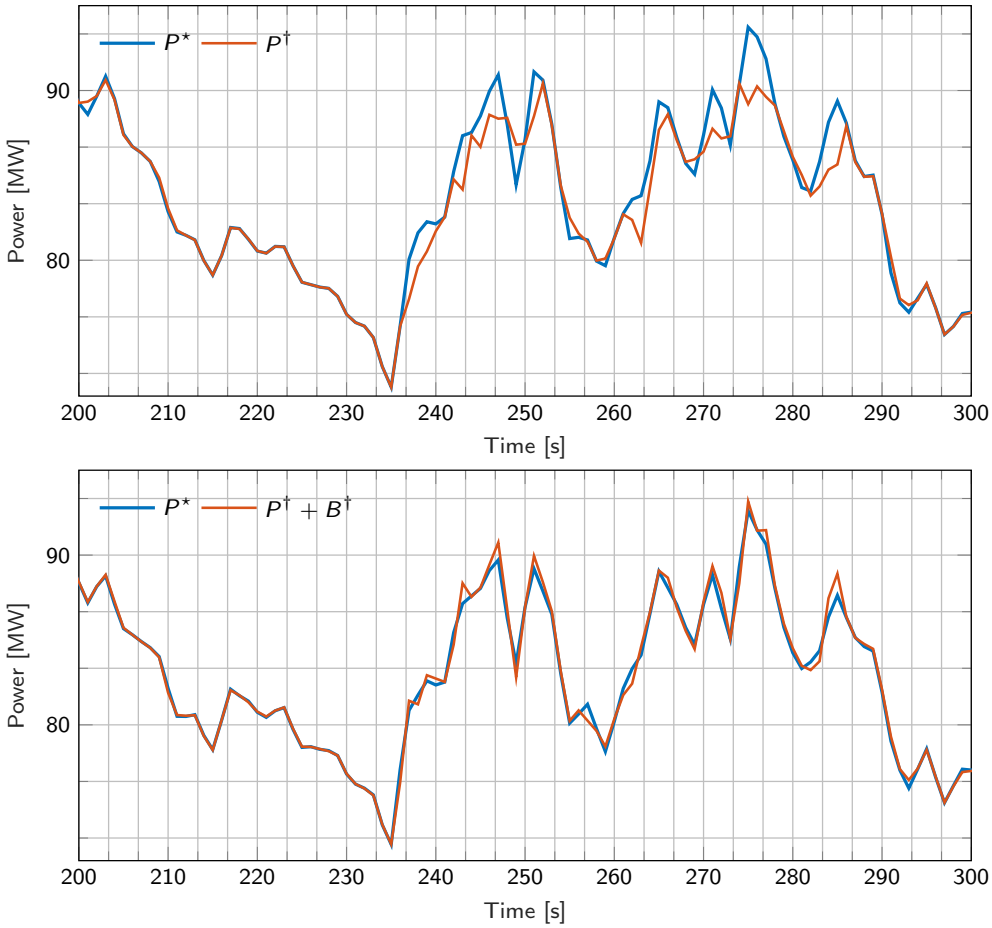

Figure 3.18: A comparison of the power output of the HPP with the original guide vane, $P^\star$, of the HPP under MPC control, $P^\dagger$, and of the hybrid power plant, $P^\dagger + B^\dagger$.

3.8 Conclusions

In this chapter, the issue of reducing mechanical fatigue on the penstock in medium-head HPPs was addressed by developing a receding horizon MPC for fatigue reduction. The root causes of penstock fatigue were initially discussed, which include hydraulic transients and water hammers resulting from increased regulation duties of the plant. A methodology was then presented to calculate the stress on each section of the penstock and determine the component's fatigue using pressure estimations obtained by the HPPs models from Chapter 2.

The key concept of avoiding stress cycles beyond the fatigue limit was used to develop the MPC. It received the guide vane set-point from the plant's governor and computed a new guide vane that did not result in fatigue. The MPC used linear models of the plant to estimate the stresses and constrain them below the fatigue limit by solving a convex optimization problem.

The simulation results obtained using a non-linear equivalent circuit model of a medium-head HPP demonstrated that:

- the linear models provided sufficiently accurate estimates of the penstock head to enforce

stress constraints effectively;

- the MPC reduced penstock damage compared to standard HPP governor and benchmark controllers,
- the proposed convex formulation of the MPC problem was computationally efficient, solving fast (tens of milliseconds), and suitable for implementation in real-life controllers.

Finally, the chapter addressed controlling the HPP hybridized with the battery. The battery set-point was obtained as the difference between the linear estimates of the torques under the original and filtered guide vanes after the MPC. The results showed that:

- the BESS power contribution necessary to reduce penstock fatigue was a small fraction of the rated power, potentially leading to positive implications for BESS sizing requirements and degradation;
- the hybrid plant was successfully controlled so as to meet the same regulation capability as the original HPP.

Chapter 4

Scheduling BESS operations for power-intensive applications

This chapter focuses on scheduling BESS operations for fatigue reduction services. In the former chapter, it was found that reducing penstock stress requires a significant amount of BESS' power and a modest amount of energy (i.e., power-intensive application). In this context, this chapter proposes a formulation of the scheduling problem specific to power-intensive applications, accounting for the dynamic power capability of the BESS based on SOC and internal resistance. The actual power capability of the BESS is estimated using the Voltage-Limited Ohmic Resistance (VLOR) method to formulate SOC-dependent power constraints within a convex optimization-based scheduling problem. Results demonstrate that, compared to traditional schedulers from the literature, which do not account for SOC-dependent power constraints, the proposed scheduler drastically reduces current violations and produces feasible schedules.

4.1 Résumé en français

Ce chapitre se concentre sur la conception d'un planificateur pour les systèmes de stockage d'énergie par batteries fournissant des services intensifs en puissance, en particulier le service de réduction de la fatigue dans une centrale hydroélectrique. Il souligne le manque de recherches sur les planificateurs adaptés aux applications intensives en puissance, mettant en lumière les conséquences de l'absence de contraintes physiques de puissance dans la formulation des problèmes.

Le chapitre présente une méthodologie qui intègre des contraintes de puissance dépendant de l'état de charge (SOC) de la batterie, résolvant ainsi le problème des planificateurs traditionnels qui ne tiennent pas compte de cette dépendance. Le modèle Voltage-Limited Ohmic Resistance (VLOR) est utilisé pour estimer la capacité de puissance réelle de la BESS en fonction de son SOC et de la résistance interne.

Le chapitre compare un planificateur traditionnel avec des courbes de capacité statiques à un planificateur utilisant des contraintes de puissance dépendant du SOC, démontrant que le dernier réduit significativement les violations de courant et produit des plannings réalisables.

En résumé, ce chapitre propose une approche novatrice pour la planification des opérations

de BESS dans des applications intensives en puissance, améliorant considérablement l'efficacité du planificateur grâce à l'intégration de contraintes dynamiques de puissance basées sur l'état de charge de la batterie.

4.2 Introduction

Battery energy storage systems have a limited capability of supplying loads since the stored energy is finite. BESSs include an application software layer responsible for firming up plans and producing a feasible charging/discharging trajectory according to the application requirements. This layer is the Energy Management System (EMS) used to optimize operations and increase the battery's performance. The scheduler's goal is to ensure that, for the battery utilization, the battery's energy and power converter's limits are respected. The scheduler achieves this by managing the recharge or discharge of the BESS to provide the required service.

When designing a scheduler, it is essential to begin by defining the BESS operator's service requirements. As discussed in Section 1.2.1, the BESS services can be grouped into energy-intensive and power-intensive.

While schedulers for energy-intensive applications have been extensively studied in the existing literature, few investigations have been conducted for power-intensive services. One notable research gap is the lack of physical power constraints in the problem formulation that consider the battery's actual power capability. As demonstrated in the next section, this oversight may result in unfeasible schedules when the BESS operates in power-intensive mode.

The main objective of this chapter is to formulate a scheduling problem for the fatigue reduction service. The lower panel of Fig. 3.16 in Chapter 3 has shown that the battery power needed to reduce the overpressures in the penstock is characterized by high spikes of a short duration when the fatigue limit is exceeded. Hence, the fatigue reduction service is a power-intensive application for the BESS.

The chapter is structured as follows: Section 4.3 shows an example of how a typical scheduler from the literature fails to produce a schedule that satisfies the subscribed service. Section 4.4 shows a method for estimating the peak power of the BESS as a function of its SOC and includes it as a constraint in the scheduling problem formulation. Section 4.5 presents a methodology for quantifying the BESS's power and energy requirements for power-intensive operations and outlines the problem formulation for the fatigue reduction service scheduler. Finally, a case study is presented in Section 4.5, which compares the performance of the new scheduler against the classical one.

4.3 Performance of a scheduler with static power limits in power-intensive applications

Methods for scheduling the charge of BESS in the existing literature consist in finding a charging/discharging power trajectory F_t over a scheduling horizon $t = 0, \ldots, T-1$ over T intervals that is optimal under a given cost function $f(\cdot)$ and subject to the kVA power rating of the BESS' con-

verter, S, and BESS state-of-charge limits, $\underline{SOC}, \overline{SOC}$. Typically, this problem has the following formulation:

$$\underset{[F_0,F_1,\ldots,F_{T-1}]}{\arg\min} \left\{ \sum_{t=0}^{T-1} f(F_t) \right\} \tag{4.1a}$$

subject to:

$$|B_t| \leq S, \qquad t = 0, \ldots, T-1 \tag{4.1b}$$

$$SOC_{t+1} = SOC_t + g(B_t), \qquad t = 0, \ldots, T-1 \tag{4.1c}$$

$$\underline{SOC} \leq SOC_{t+1} \leq \overline{SOC}, \qquad t = 0, \ldots, T-1 \tag{4.1d}$$

where SOC_t and SOC_{t+1} are the state-of-charge of the battery at the current and next time interval, and $g(\cdot)$ represents the energy increment at the time interval t as a function of the battery power B_t. The battery power at time t can be expressed as:

$$B_t = \widehat{P}_t + F_t \tag{4.2}$$

where $\widehat{P}_t$ is a point prediction of the power demand of the service to provide (e.g., primary frequency control, peak shaving), and F_t is a problem slack variable that represents the charging/discharging needs of the BESS.

In scenarios where the reactive power of a converter is also a variable in the problem, the constraint (4.1b) can be expanded to the 4-quadrant power capability of the converter:

$$B_t^2 + Q_t^2 \leq S^2 \tag{4.3}$$

where Q_t (in kVAr) is the supplied reactive power.

Model (4.1) assumes that the BESS DC voltage is constant. Indeed, under this assumption, the ampacity of the battery and power converter, which are the fundamental physical constraints of the system, can be equivalently rendered with power constraints. Under the same assumption, the SOC model can be represented with an integral over time of the discharging power in lieu of a more physically accurate Coulombic SOC model (e.g., [84, 85]).

However, the voltage of a BESS is not constant, for example it decreases with decreasing SOC values. In addition, the battery's internal resistance can determine voltage drops, altering the value of the terminal voltage. In a setting with variable voltage values, delivering the same amount of power requires a higher current at lower SOC values. This effect is not captured by scheduler (4.1) because the power constraint in (4.1b) does not depend on the SOC. Consequently, the schedule produced by (4.1) could be inaccurate and unfeasible in certain conditions, as now illustrated.

To illustrate how scheduler (4.1) may fail in producing a feasible schedule, we examine a BESS with a steady-state equivalent circuit model as in Fig. 4.1.

Battery's voltage dynamics are typically captured with equivalent circuit models composed of an Open Circuit Voltage (OCV) source and two or three RC circuits in series (see e.g., [26, 86, 87]). By assuming that the time interval of the scheduler is larger than the time constants of the RC circuits (typically from few seconds to several minutes), one can simplify such a circuit to the steady-state equivalent circuit model shown in Fig. 4.1.

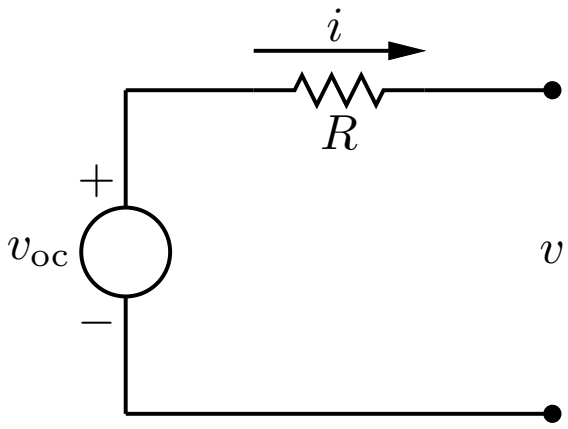

Figure 4.1: Steady-state equivalent circuit of a battery cell.

The steady-state model consists of an OCV source, series resistance R, voltage at the battery terminal (i.e., DC bus voltage) v, and DC current i. As a working example, we consider a Lithium Titanate 720 kVA/500 kWh BESS with parameters as reported in Table 4.1. Table 4.2 presents the voltage of v_{oc} as a function of the battery SOC. It is considered that, for the middle SOC range, the battery and power converter can deliver a maximum current of 1.35 kA and 0.76 kA in discharging and charging modes, respectively.

Table 4.1: Case study model parameters.

Parameter	**Unit**	**Value**
Nominal power	kVA	720
Nominal energy	kWh	500
Max voltage $\overline{V}$	V	750
Min voltage $\underline{V}$	V	530
Max current (charg.) $\overline{I}$	A	760
Min current (disch.) $\underline{I}$	A	1350
μ	-	100
γ	-	700

Let us now assume that the battery SOC at the current time instant is 15% and that the battery has been requested to discharge at its rated power of S = -720 kW in the next time interval. These pieces of information are given to scheduler (4.1), referred to as scheduler (A), which should compute a charging/discharging decision for the upcoming time interval to ensure that the BESS is in the conditions to provide the given request.

As illustrated in Fig. 4.2, scheduler (A) (blue line) maintains a constant OCV in the current time interval (t=1), resulting in the battery remaining at its current SOC. At t=2, the scheduler (A) discharges the required power, as shown in Fig. 4.3.

However, if we consider the equivalent circuit model of the battery depicted in Fig. 4.1, it becomes clear that a discharge of 720 kW would violate the current constraints outlined in Fig. 4.4.

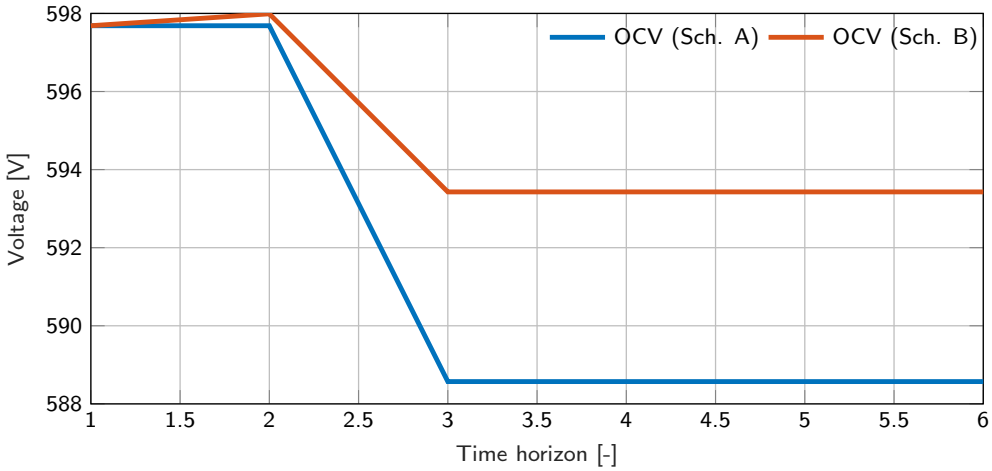

Figure 4.2: Effect of two different schedulers on the battery's OCV over the horizon time.

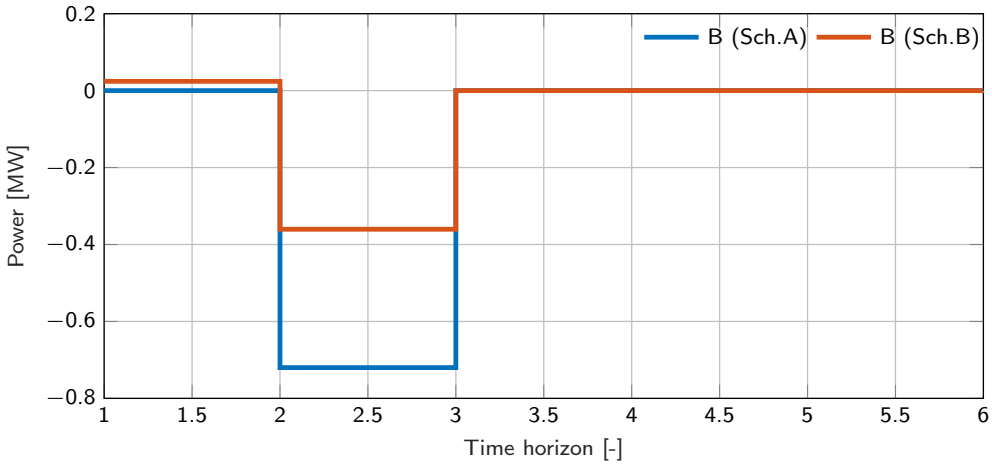

Figure 4.3: Discharging power provided with the two schedulers over the horizon time.

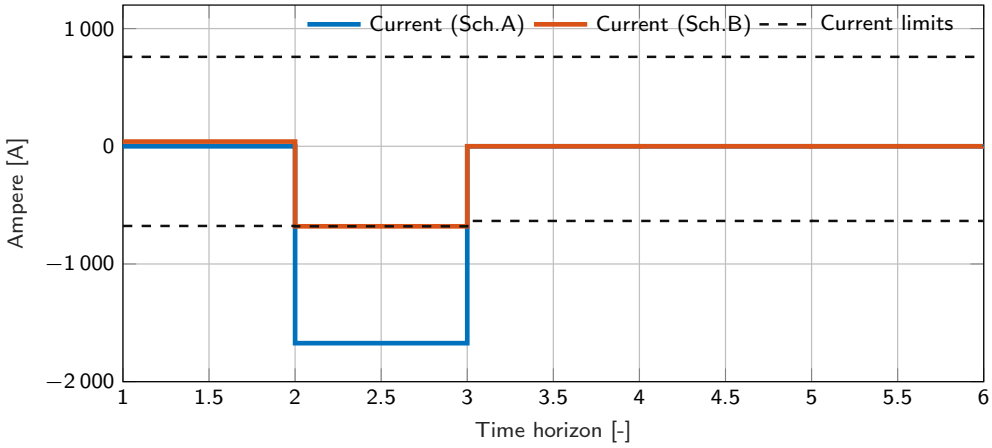

Figure 4.4: Battery currents and limits at low SOC with the two schedulers over the horizon time.

In summary, it can be concluded that the scheduler (4.1) is incapable of generating a viable schedule due to violating BESS's current limits.

To overcome this limitation, we propose a scheduler (B) that incorporates SOC power-dependent constraints in its formulation to allow a feasible schedule for power-intensive applications.

For clarity, we show the results of such a scheduler in Figs. 4.2, 4.3 and 4.4.

At time t=1, the proposed scheduler (red line) detects a violation of the power constraints and produces a set-point to charge the battery and increase its voltage (Fig. 4.2).

At time t=2, the battery provides the discharging power in Fig. 4.3, which is lower than the requested power, so that the constraints on the current are respected, as shown in Fig. 4.4.

In the next Section, we will address two crucial steps involved in formulating an improved scheduler for power-intensive applications: determining the battery's peak power capability as a function of its SOC and implementing the new power constraints into the scheduling problem.

4.4 Peak power estimation as a function of battery SOC

As discussed above, schedulers estimate the maximum charging and discharging capacity of a battery system using the kVA rating of the system. Estimating the maximum power that a BESS can deliver is paramount when controlling a battery in real-time to ensure that its operational limits are not violated. This section first reviews existing models to perform this task. Then, in the following sections, this thesis will show how one of these models can be integrated into the scheduling problem, thus achieving a more comprehensive modelling of the real-time constraints of BESS.

Existing methods to estimate the peak power that a battery can provide can be classified into two groups: characteristic maps and model-based approaches.

The characteristic-map-based techniques [88–90] utilize look-up tables stored in the Battery Management System (BMS). These tables represent the static correlation between the battery's electrical quantities, such as peak power, SOC, State-Of-Health (SOH), and working conditions such as terminal voltage and temperature. The Hybrid Pulse Power Characterization (HPPC) test procedure [90] is a commonly used method to obtain the characteristic maps.

A second family of techniques to estimate the maximum power are model-based. Model-based power estimation is generally regarded as a more promising approach. Several approaches have been proposed in the literature depending on the adopted model [91–98]:

- the SOC-limited method is used to estimate the battery's peak current based on the minimum and maximum SOCs. This method gives optimistic estimations of the battery's peak current if the battery is allowed to be discharged or charged over a wide range of SOC [96];
- the Voltage-Limited Ohmic Resistance (VLOR) method [93] estimates the peak power based on the equivalent circuit model in Fig. 4.1. Although simple, this estimate can be a reasonable initial guess for iterative algorithmic methods and will be further discussed next;
- the Voltage-Limited Extrapolation in the OCV method (VLEO) [93, 98] considers the dynamics of the RC elements and OCV change over a specified time range.

- the Two-Time-Constant (TTC) model has been used to compute the maximum power capability of the battery on the DC bus and integrated in a model-based real-time controller [99].

In this thesis, we leverage the VLOR method [93], briefly illustrated hereafter. Such a method has been chosen to highlight the importance of accounting for the maximum power estimation when formulating the scheduler problems for power-intensive applications. Despite its simplicity, this method has been proven to be effective in producing a feasible schedule for the BESS that respects the real-time constraints of the battery. Future works may consider the comparison of different model-based approaches to establish the best model suitable for various applications.

4.4.1 VLOR method

The VLOR method utilizes a simplified circuit model illustrated in Fig. 4.1 to estimate the peak power of a battery.

The power provided by the circuit in Fig. 4.1 is given by the product of terminal voltage and current:

$$B = v \cdot i \tag{4.4}$$

Typically, the battery supplier provides a current limitation of the batteries. In any case, the current of the battery cell should never exceed these limits. Besides this limitation, the peak power of the battery in real applications is also limited by voltage. Thus, both voltage and current limitations are considered in the power estimation.

We assume that the SOC and the v_{oc} are related by the following linear relation:

$$v_{oc}(SOC) = \psi + \mu \cdot SOC \tag{4.5}$$

where ψ and μ are two constants determined experimentally, v_{oc} is the open-circuit voltage expressed in Volts and the SOC in percentage points (0% = empty; 100% = full). The internal resistance R is also a function of the SOC, as reported in Table 4.2 for the considered BESS.

Table 4.2: Considered BESS open-circuit-voltage and series resistance for different SOC ranges [26].

SOC [%]	**0-20**	**20-40**	**40-60**	**60-80**	**80-100**
v_{oc} [V]	592.2	625.0	652.9	680.2	733.2
R [Ω]	0.029	0.021	0.015	0.014	0.013

The terminal voltage v of the circuit in Fig. 4.1 can be written as:

$$v = v_{oc}\,(SOC) - R\,(SOC) \cdot i \tag{4.6}$$

The minimum and maximum battery currents (I_{min}, I_{max}), where the negative values correspond to the charging current and the positive values to the discharging current, are obtained considering the voltage limits:

$$I_{min} = \frac{v_{oc}\,(SOC) - \overline{V}}{R\,(SOC)} \tag{4.7a}$$

$$I_{max} = \frac{v_{oc}\,(SOC) - \underline{V}}{R\,(SOC)} \tag{4.7b}$$

where $\overline{V}$ and $\underline{V}$ are the battery's allowed maximum and minimum terminal voltages.

Considering current and voltage limits, the maximum charge and discharge currents can be determined by:

$$I_{charge} = \max\left(\underline{I}, I_{min}\right) \tag{4.8a}$$

$$I_{disch} = \min\left(\overline{I}, I_{max}\right) \tag{4.8b}$$

where $\overline{I}$ and $\underline{I}$ are the rated currents of the system specified by the battery manufacturer.

Finally, the peak power estimation of the battery is obtained as:

$$\underline{B} = v_{oc}\left(SOC\right) \cdot I_{disch} - R\left(SOC\right) \cdot I_{disch}^2 \tag{4.9a}$$

$$\overline{B} = v_{oc}\left(SOC\right) \cdot I_{charge} - R\left(SOC\right) \cdot I_{charge}^2 \tag{4.9b}$$

The resulting charging and discharging peak power estimations as a function of the battery's SOC are shown in Fig. 4.5 for the system under consideration in Table 4.1. Fig. 4.5 shows that the battery's power capability is not constant over its SOC range. On the one hand, at low SOC values, the maximum discharging power is lower in absolute value the maximum charging power due to the need to maintain a minimum voltage value. On the other hand, at high SOC values, the maximum charging power is lower in absolute value than the maximum discharging power to avoid an overvoltage. Within the middle region and for the same SOC values, the charging power capability is smaller than the discharging power capability. The main factors affecting the charging and discharging power capabilities are the cut-off voltages, $\overline{V}$ and $\underline{V}$. Typically, the difference between the OCV and $\underline{V}$ is larger than the difference between the OCV and $\overline{V}$. This discrepancy is apparent when the battery operates within the middle SOC range, which makes the charging power capability smaller than the discharging power capability [100].

In the next section, we show how this SOC-dependent power curve of the BESS is implemented in the scheduling problem to represent the power constraints in battery power-intensive applications accurately.

It is worth highlighting that, compared to, e.g., [101], we do not consider a TTC model of the BESS but an internal-resistance model because the transients of the TTC models are typically faster than the time step of the scheduler. However, owing to the linearity of the TTC model (and assuming time-invariant parameters) one could integrate the TTC model into the proposed approach without significantly impacting the tractability of the problem.

4.4.2 Inclusion of power constraints in the scheduling problem

The curves in Fig. 4.5 replace the static constraints in Eq. (4.1b). The feasible operating region for the battery power is the area between these two curves. Because this area is convex, it can be represented by a set of linear inequalities, as described in the following, thus enabling a tractable implementation of this set of constraints.

For this development, we approximate the convex envelope in Fig. 4.5 with the following upper

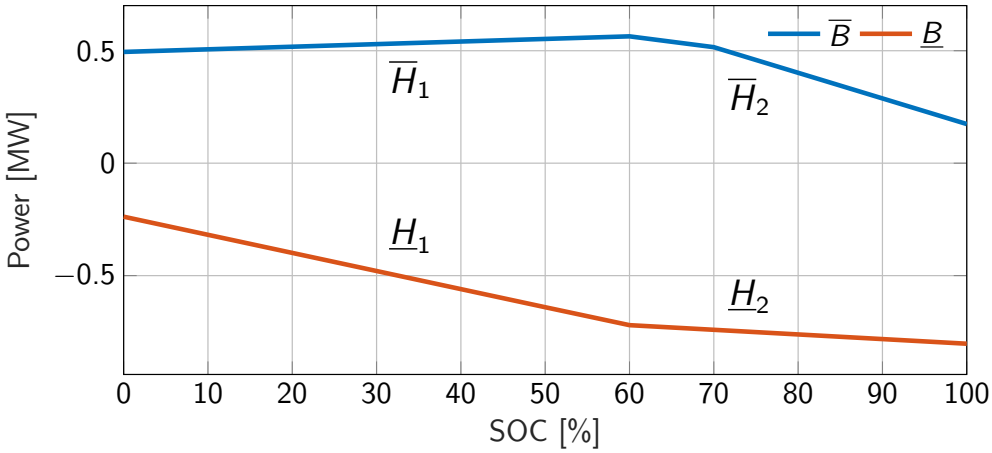

Figure 4.5: Charging (blue line) and discharging (red line) peak power estimation as a function of the SOC.

and lower bounds that are linear functions of the SOC:

$$\overline{H}_k = \overline{a}_k + \overline{b}_k \cdot SOC, \qquad k = 0, \dots, K \tag{4.10a}$$

$$\underline{H}_j = \underline{a}_j + \underline{b}_j \cdot SOC \qquad j = 0, \dots, J \tag{4.10b}$$

where the coefficients $\left(\overline{a}_k, \underline{a}_j\right)$ and $\left(\overline{b}_k, \underline{b}_j\right)$ can be estimated from the curves.

The scheduling problem presented in (4.1) can be reformulated as follows:

$$\underset{[F_0, F_1, \dots, F_{T-1}]}{\arg\min} \left\{ \sum_{t=0}^{T-1} f(F_t) \right\} \tag{4.11a}$$

subject to:

$$B_t \leq \overline{a}_k + \overline{b}_k \cdot SOC_t, \qquad t = 0, \dots, T-1 \tag{4.11b}$$

$$B_t \geq \underline{a}_j + \underline{b}_j \cdot SOC_t, \qquad t = 0, \dots, T-1 \tag{4.11c}$$

$$SOC_{t+1} = SOC_t + g(B_t), \qquad t = 0, \dots, T-1 \tag{4.11d}$$

$$\underline{SOC} \leq SOC_{t+1} \leq \overline{SOC}. \qquad t = 0, \dots, T-1 \tag{4.11e}$$

for $k = 0, \dots, K$ and $j = 0, \dots, J$.

The constraints in Eq. (4.11b)-(4.11c) are linear functions of the SOC, which is in turn a linear function of the battery power. The next section will provide a preliminary formulation of a BESS scheduler for the fatigue reduction service in medium-head HPPs embedding dynamic power capability curves.

4.5 Application to fatigue reduction service

4.5.1 Formulation of the scheduling problem

The objective of the scheduling problem is to keep the SOC value of the BESS at a feasible level to perform the fatigue reduction service. For example, if the state of charge of the BESS is too low

to enable a reliable provision of the prescribed services, it is the role of the scheduler to compute a suitable recharging power set-point. This objective is met by calculating a value, called offset and described later, which is over-imposed to the real-time battery power set-point so as to correct the SOC level of the BESS.

The requirements of the fatigue reduction service and its impact on the charging/discharging of the BESS enter the problem in the form of forecasts of the required power at a given time interval that is necessary to deploy to perform such a service. However, because the fatigue reduction service is a power-intensive application but modest in terms of energy, we propose using two sets of forecasts: one for the power requirements and one for the energy requirements. This design choice stems from the fact that using power forecasts only would quickly saturate the battery energy capacity in the scheduling problem, leading to very conservative scheduling decisions. For the sake of clarity, this aspect will be rediscussed after the formulation of problem (4.20).

The BESS power injection and energy during real-time operation to compensate for the fatigue reduction are:

$$B_t = \hat{P}_t + F_t, \qquad t = 0, \dots, T-1 \tag{4.12}$$

$$E_t = \hat{W}_t + T_s \cdot F_t, \qquad t = 0, \dots, T-1 \tag{4.13}$$

where $\hat{P}_t$ and $\hat{W}_t$ are predictions of the battery power and energy demand, respectively, F_t is the offset profile that accounts for the amount of energy necessary to maintain the battery at a flexible SOC level, and T_s is the duration of the sampling time in hours.

Because $\hat{P}_t$ and $\hat{W}_t$ are difficult to forecast precisely as they depend on grid frequency variations, we replace them with estimates of their lower and upper bounds $(\hat{P}_t^{\uparrow}, \hat{P}_t^{\downarrow})$, $(\hat{W}_t^{\uparrow}, \hat{W}_t^{\downarrow})$, in the form of prediction intervals. These prediction intervals can be used to model the worst-case imbalances that the BESS needs to compensate for. In particular, these are:

$$B_t^{\uparrow} = \hat{P}_t^{\uparrow} + F_t \tag{4.14}$$

$$B_t^{\downarrow} = \hat{P}_t^{\downarrow} + F_t \tag{4.15}$$

$$E_t^{\uparrow} = \hat{W}_t^{\uparrow} + T_s \cdot B_t^{\uparrow} \tag{4.16}$$

$$E_t^{\downarrow} = \hat{W}_t^{\downarrow} + T_s \cdot B_t^{\downarrow} \tag{4.17}$$

The boundaries of the SOC evolution over time can be derived by applying (4.16),(4.17) to (4.11d). At this stage, we neglect the charging/discharging efficiency. However, this can be included by using conventional strategies from the literature, such as splitting the BESS power in mutually exclusive charging and discharging power. The SOC evolution over time reads as:

$$SOC_{t+1}^{\uparrow} = SOC_t^{\uparrow} + \frac{T_s}{E_n}\left(\hat{W}_t^{\uparrow} + F_t\right) \tag{4.18}$$

$$SOC_{t+1}^{\downarrow} = SOC_t^{\downarrow} + \frac{T_s}{E_n}\left(\hat{W}_t^{\downarrow} + F_t\right) \tag{4.19}$$

where SOC_{t+1} and SOC_t are the state-of-charge at the next and current time interval and E_n is the rated energy of the battery.

We formulate an optimization problem to determine the value of decision vector $\mathbf{F}^o = [F_0^o, \dots, F_T^o]$ that ensures that BESS energy capacity is available for the fatigue reduction of the penstock during

the provision of primary and secondary frequency regulation. The offset profile alters the real-time set-point of the battery by acting as slack in battery energy constraint and relaxes it when not feasible. We seek to minimize the squared-sum offset profile F within a given time window T such that BESS energy and power are always in the respectively allowed bounds, namely$(\underline{SOC}, \overline{SOC})$ and $(\underline{B}(SOC), \overline{B}(SOC))$.

Assuming to be at time interval t and considering the power constraints found in the previous section, the optimization problem reads as:

$$\mathbf{F}^0 = \arg\min_{\mathbf{F}} \left\{ \sum_{t=0}^{T-1} F_t^2 \right\} \tag{4.20a}$$

subject to:

$$P_t^{\uparrow} + F_t \leq \overline{a}_j + \overline{b}_j \cdot SOC_t^{\uparrow} \tag{4.20b}$$
$$P_t^{\downarrow} + F_t \geq \underline{a}_k + \underline{b}_k \cdot SOC_t^{\downarrow} \tag{4.20c}$$
$$P_t^{\uparrow} + F_t = P_t^{\downarrow} + F_t \tag{4.20d}$$
$$SOC_{t+1}^{\uparrow} = SOC_t^{\uparrow} + \frac{T_s}{E_n}\left(\hat{W}_t^{\uparrow} + F_t\right) \tag{4.20e}$$
$$SOC_{t+1}^{\downarrow} = SOC_t^{\downarrow} + \frac{T_s}{E_n}\left(\hat{W}_t^{\downarrow} + F_t\right) \tag{4.20f}$$
$$SOC_{t+1}^{\uparrow} \leq \overline{SOC} \tag{4.20g}$$
$$SOC_{t+1}^{\downarrow} \geq \underline{SOC} \tag{4.20h}$$
$$\tag{4.20i}$$

for $t = 0, \ldots, T-1$, $k = 0, \ldots, K$ and $j = 0, \ldots, J$.

It is worth highlighting that the energy prediction intervals are used for the SOC model, while the power prediction intervals are used for the power rating constraints. Despite the fact that these two sets of prediction intervals are intrinsically related (i.e., these forecasts are generated from the same time series, just re-sampled at two different time intervals), they are used in a disconnected way to ensure scheduling not only enough energy capacity but also sufficient power capability. In fact, in power-intensive applications, "instantaneous" needs for power might be significant, but for a few seconds only, thus small in terms of energy. Using (large) power prediction intervals in the SOC model would lead to saturating the BESS energy storage capacity and unrealistic energy storage requirements. Decoupling these two forecasts is thus proposed as a way to model the requirements of power-intensive applications. To the best of the authors' knowledge, this attempt is not recorded in the existing literature. A possible avenue to explore further in this context is looking how these two different sets of prediction intervals, which are intrinsically related as discussed above, could be explicitly "reconciled" to give coherent power and energy estimates.

4.5.2 Quantifying BESS's power and energy needs for fatigue reduction

The optimization problem in (4.20) requires suitable forecasts, in terms of prediction intervals, of the services to provide with the BESS in order to ensure proper energy management. This

section explains the methodology used to quantify the BESS' power and energy needs to provide the fatigue reduction service to the HPP for primary and secondary frequency regulation. The ultimate objective of this exercise is to determine the prediction intervals of power, $(\hat{P}_t^{\uparrow}, \hat{P}_t^{\downarrow})$, and energy, $(\hat{W}_t^{\uparrow}, \hat{W}_t^{\downarrow})$, to be included in the scheduling problem.

The method adopted to compute the prediction intervals consists of the following three steps, which are explained in the rest of this section:

1. estimating the battery power and energy demand;
2. computing the statistical distributions (i.e., histograms) of these estimations;
3. determining power and energy prediction intervals by selecting symmetric quantiles (e.g., 5% and 95%) of the computed distributions.

The BESS power and energy are modelled as composed by the contribution of primary and secondary frequency control:

$$\hat{P}_\tau = \hat{P}_\tau^{\,pfc} + \hat{P}_\tau^{\,sfc} \tag{4.21}$$

$$\hat{W}_t = \hat{W}_t^{\,pfc} + \hat{W}_t^{\,sfc}, \tag{4.22}$$

where t and τ denote time interval indexes, as further discussed next. We show in the following how these contributions are estimated and how prediction intervals are finally derived.

Contribution of PFC The power required from the battery to implement fatigue reduction during PFC could formally be computed by applying the problem formulation of the real-time control problem in Section 3.6.2 and Eq. (3.17); however, we introduce a simplified model aimed at producing large time series data to estimate forecasting models for this service in a computationally more tractable way. As it will explained in this section, this simplification consists primarily in approximating the behavior of the MPC action with a rate limiter, whose similarities were discussed in Section 3.6.5. The rate limit of this limiter is estimated by running a simple system identification procedure on the power output of the HPP.

Let f_τ for $\tau = 0, 1, \ldots$ denote a time series with grid frequency measurements at high temporal resolution (e.g., from [80]) and f_{nom} the nominal grid frequency (e.g., 50 Hz). The power for PFC, $\hat{P}_\tau^*$, can be approximated as:

$$\hat{P}_\tau^* = (f_\tau - f_{\text{nom}}) \frac{P_{\text{nom}}}{f_{\text{nom}} \cdot B_s} \tag{4.23}$$

where P_{nom} is the plant nominal power and B_s is the droop. In this model, plant dynamics are neglected. This assumption is deemed reasonable as the objective is not real-time control but feeding a forecasting model.

Similarly, the power output after the MPC action (modelled with a rate limiter) is:

$$\hat{P}_\tau^\dagger = \left(f_\tau^{rl} - f_{\text{nom}}\right) \frac{P_{\text{nom}}}{f_{\text{nom}} \cdot B_s} \tag{4.24}$$

where f_τ^{rl} denotes the grid frequency measurements filtered with the rate limiter.

To model the BESS power contribution, we leverage the same principle adopted for the hybrid real-time controller; namely, the BESS is called to provide the missing PFC after the action of the MPC. In this context, the BESS power is the difference between the two quantities above:

$$\hat{P}_\tau^{pfc} = \hat{P}_\tau^{*} - \hat{P}_\tau^{\dagger} = \left(f_\tau - f_\tau^{rl}\right) \frac{P_{\text{nom}}}{f_{\text{nom}} \cdot B_s}. \tag{4.25}$$

The energy requirements for PFC is computed by integrating the BESS power contribution $\hat{P}_\tau^{pfc}$ over a suitable time interval. This is given by:

$$\hat{W}_t^{pfc} = \frac{t_s}{3600} \cdot \sum_{\tau}^{T/t_s} \left(\hat{P}_\tau^{pfc}\right) \tag{4.26}$$

where t_s is the sampling time (in seconds), T is the number of ninety-second intervals in the signal and $\hat{W}_t^{pfc}$ is the energy at current time interval (in kWh). The ninety-second resolution is chosen to determine the dispatch plan for this specific application.

Contribution of SFC As for PFC, the contribution of SFC is estimated as the difference between the a power set-point for secondary frequency control and the same signal filtered with the rate limiter. The considered power set-point signal for SFC is shown in Fig. 4.6. It refers to to a signal delivered by Swissgrid from [49].

The energy is calculated as follows:

$$\hat{W}_t^{sfc} = \frac{t_s}{3600} \cdot \sum_{\tau}^{T/t_s} \left(\hat{P}_\tau^{sfc}\right) \tag{4.27}$$

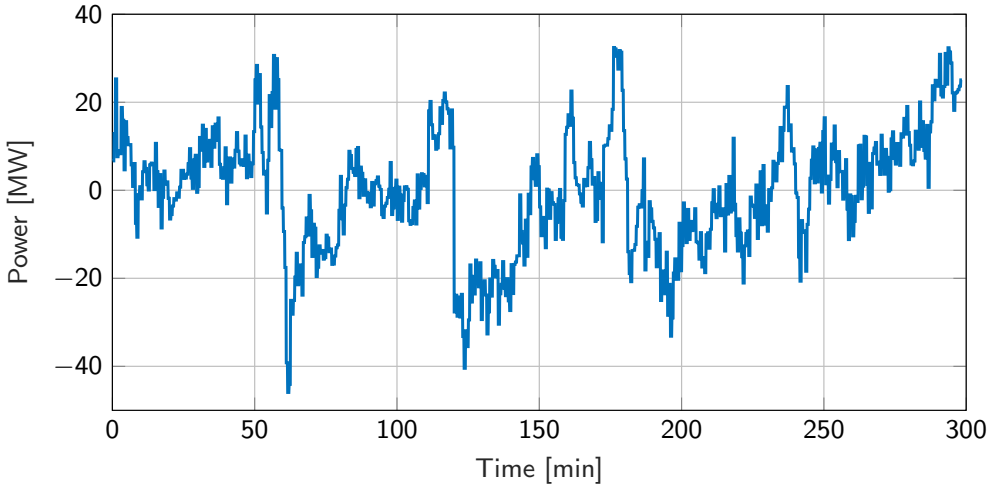

Figure 4.6: A power set-point for secondary frequency control.

Distribution and computation of the prediction intervals The distributions of the samples in the time series P_τ and W_t are shown in Fig. 4.7. Finally, the prediction intervals for power and energy, $(\hat{P}_t^{\uparrow}, \hat{P}_t^{\downarrow})$ and $(\hat{W}_t^{\uparrow}, \hat{W}_t^{\downarrow})$ respectively, to be used in the scheduler problem are selected as symmetric quantiles from these distributions. It is worth highlighting that one could use alternative forecasting strategies in the proposed BESS scheduler than the one adopted in this work.

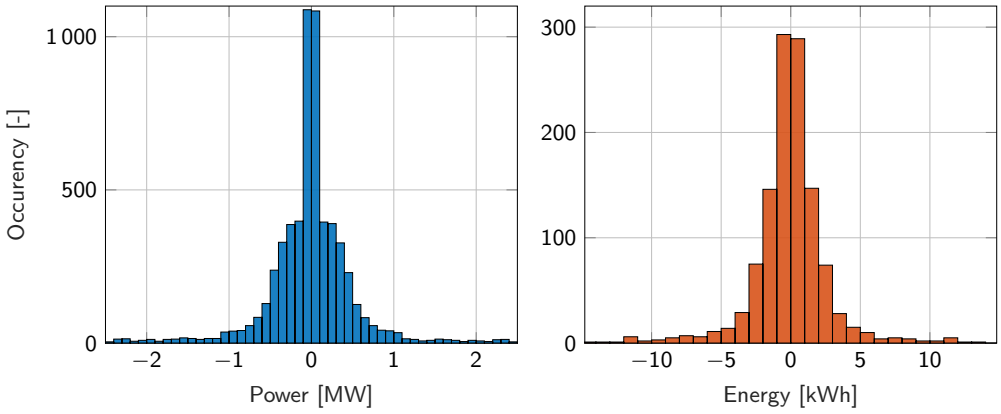

Figure 4.7: Distribution of the power and energy predictions resulting from PFC + SFC.

4.5.3 Case study and simulation procedure

It is considered the same medium-head hybrid HPP described in Chapter 3 equipped with BESS with parameters as in Table 4.1.

The interval of the optimization horizon of the scheduler is 90 seconds, and the length of its optimization horizon is 90 minutes. These two parameters are chosen because they are deemed compatible with the timing of primary and secondary frequency control, which require quick rescheduling of the energy storage assets. The scheduler is applied in a receding horizon manner, namely at each time interval t, the scheduling problem is solved, and only the first element of the decision vector is considered for actuation.

The adopted simulation procedure is depicted in Fig. 4.8. At time $t = 0$, the scheduler solves the optimization in (4.20) and determine the trajectory of the decision vector F for the given horizon. Only the first element of the control input is then applied to the system. This value of the offset power is given to the MPC for fatigue reduction that each second computes the guide vane set-point $y^{\dagger}(t)$ of the hydropower plant to keep the penstock stress below the fatigue limit and adjusts the battery's set-point $B^{\dagger}(t)$ to provide the missing regulation. At each second, a simulation is performed where the MPC set-point is given to the HPP (modelled using a a nonlinear HPP model) and to the BESS. After 90 seconds, the scheduling optimization problem is solved again with updated information from the real-time layer (i.e., MPC and simulation). Fig. 4.9 shows the control inputs of the scheduler and the MPC and the information exchanged between the two layers.

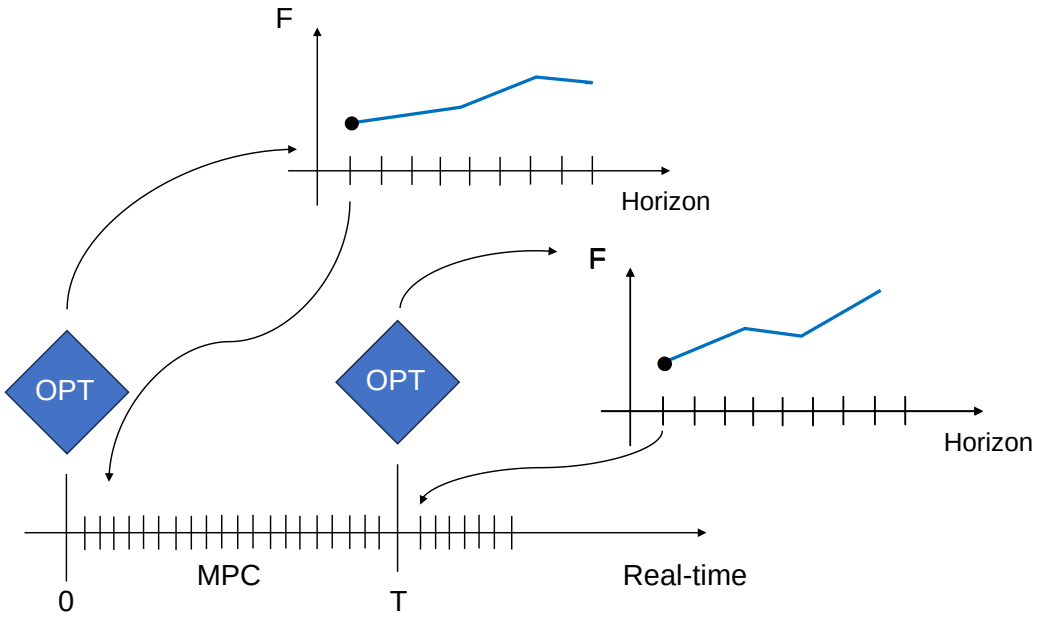

Figure 4.8: Operation sequence for the scheduler and real-time controller framework.

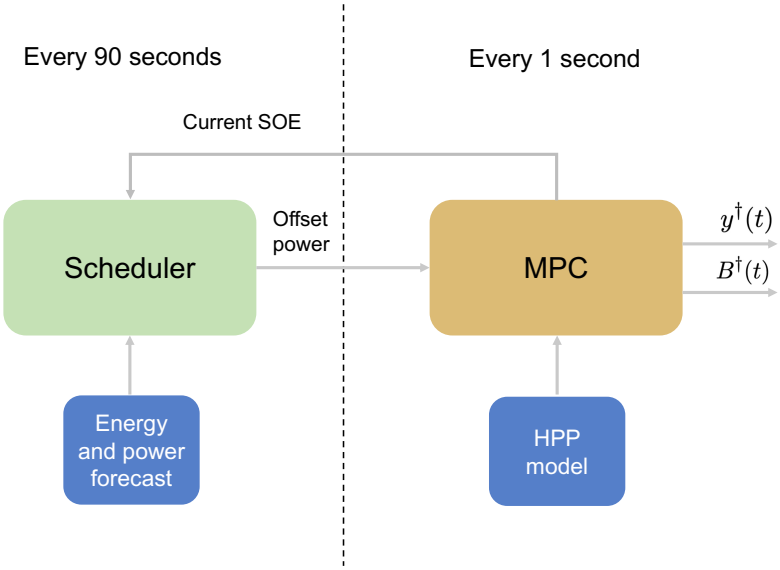

Figure 4.9: Control inputs and information exchanged between the two layers.

4.5.4 Comparison between classical and power-intensive schedulers

This section compares the performance of two different schedulers. The first scheduler uses the classical formulation as in (4.1) , while the second scheduler uses the formulation in (4.20) with SOC-dependent power constraints. These two schedulers are denoted as schedulers (A) and (B), respectively. The comparison involves two aspects:

1. assessing the efficacy in generating a feasible offset power that respects the power and energy constraints of the battery;
2. evaluating the compliance of the ampacity (current) constraints.

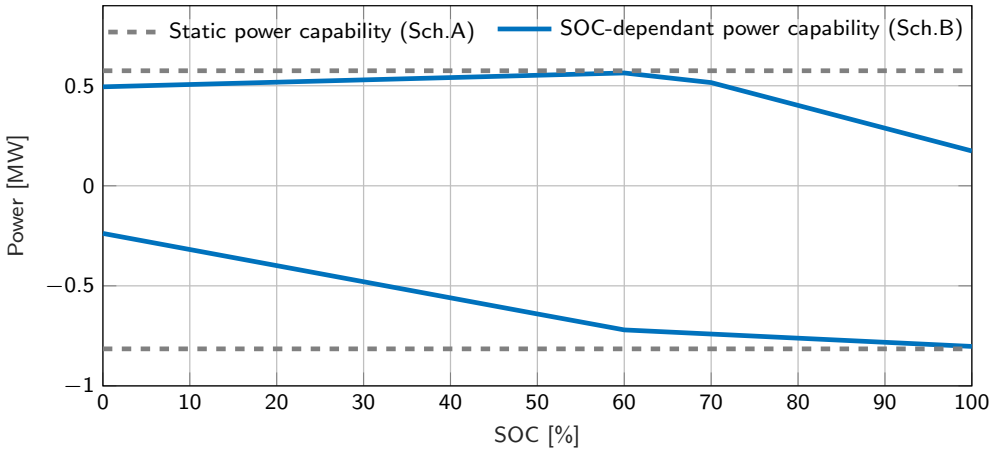

Figure 4.10: Capability curves implemented in the two schedulers.

The performance of the schedulers was evaluated during a period of 24 hours by simulating different scenarios of initial SOC conditions.

In addition to providing the fatigue reduction service, the BESS is assumed to provide an additional grid ancillary service with the following power characteristics:

- when the initial SOC is within the range of 10% to 50%, the battery must provide a constant discharging power of 50 kW for 12 hours and 250 kW of charging power for the remaining period;
- when the SOC is within the range of 60% to 90%, the battery must provide a constant discharging power of 250 kW for 12 hours and 50 kW of charging power for the remaining period.

This additional service (that could correspond to, e.g., peak-shaving or grid congestion management) is implemented in order to reproduce variable SOC conditions for the BESS in the optimization and simulation problems.

Table 4.3 displays the minimum and maximum expected power and energy realization for the two SOC ranges, considering the 9th percentile of the distributions presented in Section 4.5.2.

Table 4.3: Upper and lower power and energy bounds.

SOC Range	$\hat{P}_t^{\uparrow}$	$\hat{P}_t^{\downarrow}$	$\hat{W}_t^{\uparrow}$	$\hat{W}_t^{\downarrow}$
10-50%	0.6 MW	-0.6MW	4.1 kWh	-5.2kWh
50-90%	0.6 MW	-0.6MW	5.2kWh	-4.1kWh

Fig. 4.11 illustrates a comparison of the performance of the two schedulers with the battery's initial SOC set to 10%. The hybrid plant implements the real-time controller for fatigue reduction.

The schedulers receive the current SOC from the real-time MPC and determine an offset profile F that satisfies the energy and power constraints within a given time horizon T of 90 minutes. The present case requires the battery to discharge 50 kW for the first 12 hours and charge 250 kW for the rest, to provide peak-shaving services. The power energy previsions for the future time window are as in the first line of Table 4.3.

We now discuss the performance of the two schedulers under the first comparison, consisting in generating feasible schedules while meeting the power and energy constraints.

- Scheduler (A) implements the static power constraints (grey dashed lines in Fig. 4.10), with the charging and discharging power limits set at 0.6 MW and -0.8 MW, respectively. Scheduler (A) produces a positive offset to maintain the SOC at the acceptable lower limit $\underline{SOC} = 10\%$ (solid blue line in the middle panel of Fig.4.11) over the optimization horizon. At t = 12h, the battery is required to provide a charging power of 250 kW for the remaining period, and scheduler (A) generates a negative offset to respect the SOC upper limit $\overline{SOC} = 100\%$. However, the SOC exceeds the limit at t = 22 h, and thus scheduler (A) fails to comply with the energy constraints.

- Scheduler (B) implements the SOC-dependant power constraints (solid blue line in Fig. 4.10). Since the battery's SOC is 10%, it cannot deliver the predicted power of 0.6 MW, and hence scheduler (B) generates a positive offset power F_2 to charge the battery up to an SOC level of around 40% (dashed red line in the middle panel of Fig.4.11), where it can meet the power requirement. At t = 12h, the offset power becomes negative, as for scheduler (A), and the SOC upper limit $\overline{SOC}$ is respected.

The lower panel in Fig. 4.11 depicts the total output power of the battery generated by the combination of real-time power used for fatigue reduction and peak-shaving services, $B^{\dagger}$, and the offset power, F, produced by the two schedulers.

The second comparison aims to assess the adherence to the current limitations, as elaborated in Section 4.3. Fig. 4.12 displays the BESS output current resulting from the two scheduler's actions and the current limits corresponding to the SOC levels from the middle panel of Fig. 4.11. In the initial 12 hours, scheduler (A) maintains a constant SOC of 10%, corresponding to a maximum dischargin current of 560 A. In contrast, scheduler (B) charges the battery, leading to an increase in the maximum allowed discharging current up to 1100 A. The number of current limit violations, indicated by the blue and red markers in Fig. 4.12, is 10 for scheduler (A) and 5 for scheduler (B). During the remaining simulation period, scheduler (A) violates the upper current limits eight more times due to the sudden increase in the battery's SOC. After t = 22h, when the energy constraints are exceeded, current violations are not taken into account.

The analysis has been repeated for different initial SOC and the two schedulers have been compared based on the following metrics: the number of current limit violations, the average difference from the upper and lower current limits, and their variance. The results are summarized in Table 4.4. Based on the analysis, the following conclusions can be drawn:

1. scheduler (B) drastically reduces the number of current violations by 28% in the range 10-50% and by 40% in the range 60-90% of the initial SOC.

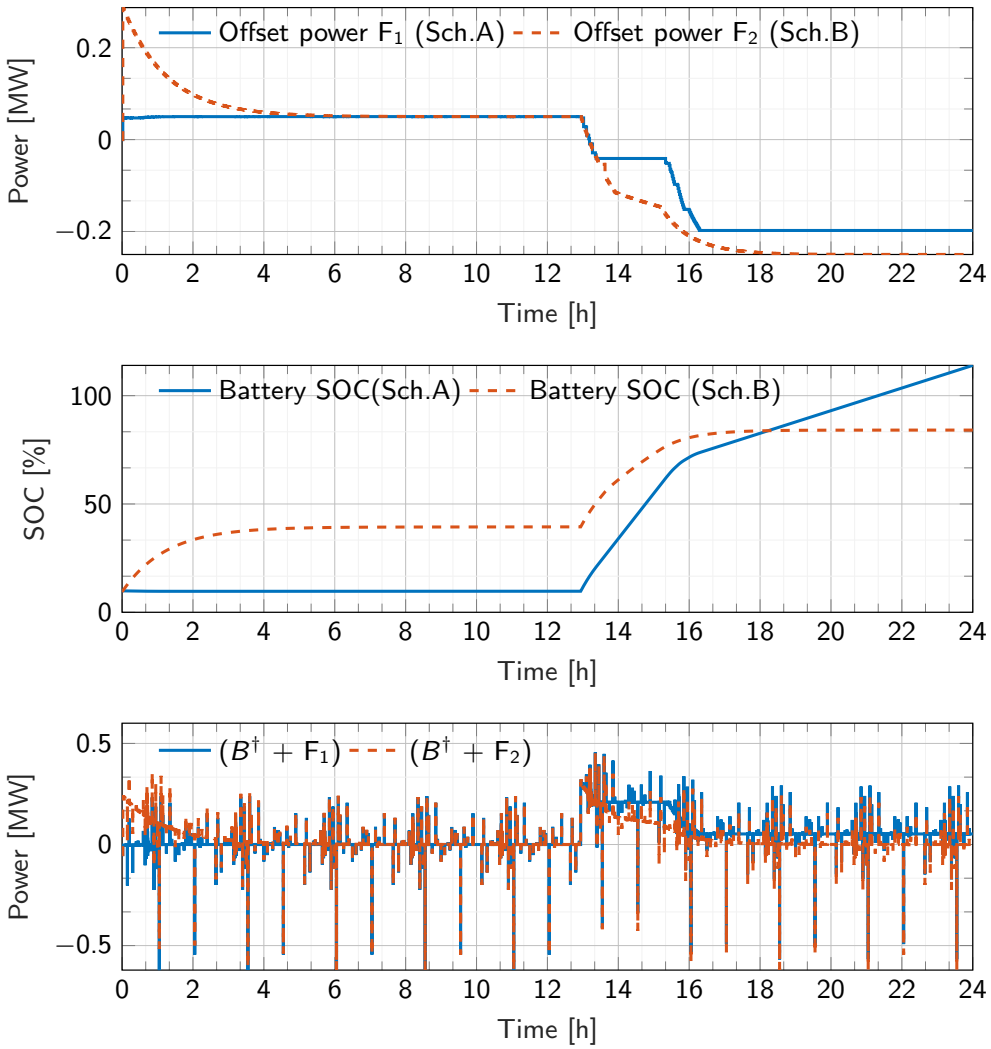

Figure 4.11: Offset profiles of the two schedulers (top panel), battery SOC evolution from the provision of the fatigue reduction and peak-shaving services (middle panel) and battery output power as the sum of the offset profile and the regulating power $B^\dagger$ (bottom panel).

2. Both schedulers show low values for the average distance of the BESS current from the upper limits. However, scheduler (B) performs better with a reduction of 30% of the average distance and a lower variance compared to scheduler (A).

3. Regarding the current's violations due to the battery discharge, scheduler (B) significantly reduces the average difference from the lower limit by a factor of three, with a reduction of the variance of one order of magnitude compared with scheduler (A).

In conclusion, the results demonstrate that implementing SOC-dependent power constraints in the scheduler's problem formulation considerably impacts the scheduler's performance in power-intensive applications, reducing the probability of producing inaccurate and unfeasible schedules.

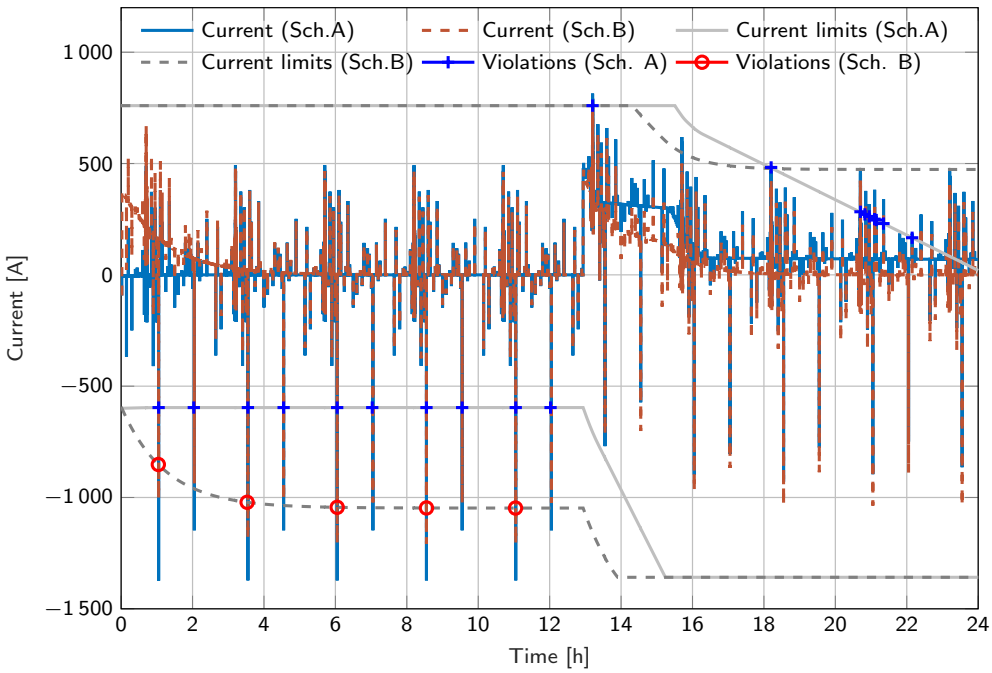

Figure 4.12: Battery currents, current limits and violations. The blue and red curves correspond to the BESS currents due to the action of the two schedulers. The solid and dashed grey lines are the actual current limits of the battery as a function of its SOC resulting from scheduler (A) and (B), respectively. The blue and red markers report the violation of the current limits.

Table 4.4: Schedulers' perfomance comparison on current limits violation.

Type of scheduler	**N^o of violations**	**Average diff. (upper) [A]**	**Variance (upper)**	**Average diff. (lower) [A]**	**Variance (lower)**	**Initial SOC [%]**
Sch.A	18	24.77	233.13	-329.92	$5.21 \cdot 10^4$	10%
Sch.B	5	-	-	-105.32	$2.82 \cdot 10^3$	
Sch.A	18	24.77	233.13	-334.87	$5.08 \cdot 10^4$	20%
Sch.B	6	-	-	-105.81	$2.82 \cdot 10^3$	
Sch.A	18	24.77	233.13	-339.92	$5.02 \cdot 10^4$	30%
Sch.B	6	7.82	19.42	-106.31	$2.86 \cdot 10^3$	
Sch.A	18	24.76	233.08	-333.82	$4.58 \cdot 10^4$	40%
Sch.B	6	7.82	19.42	-106.83	$2.88 \cdot 10^3$	
Sch.A	19	24.77	233.36	-322.87	$4.55 \cdot 10^4$	50%
Sch.B	6	7.81	19.42	-107.36	$2.91 \cdot 10^3$	
Sch.A	22	-	-	-347.34	$1.50 \cdot 10^5$	60%
Sch.B	9	-	-	-302.26	$4.30 \cdot 10^4$	
Sch.A	22	-	-	-345.35	$1.50 \cdot 10^5$	70%
Sch.B	9	-	-	-302.26	$4.30 \cdot 10^4$	
Sch.A	22	-	-	-345.29	$1.49 \cdot 10^5$	80%
Sch.B	9	-	-	-302.26	$4.30 \cdot 10^4$	
Sch.A	22	-	-	-341.46	$1.49 \cdot 10^5$	90%
Sch.B	9	-	-	-302.26	$4.30 \cdot 10^4$	

4.6 Conclusions

This chapter formulated a scheduler to ensure adequate SOC levels in a BESS providing fatigue reduction service to an HPP. It was shown that traditional schedulers from the literature might fail in producing a reliable schedule because they consider static power constraints of the BESS, i.e., they assume that the BESS can provide the rated power at any level of SOC. To address this shortcoming, we used the model-based VLOR method to derive dynamic capability curves of the BESS power. These curves were successfully integrated into the problem formulation of a scheduler as a set of linear (and convex) power constraints.

The scheduler is part of a two-layer controller and was tested by simulations in an HPP case study. The upper-level controller is the scheduler that aims to produce an offset profile to charge or discharge the battery, based on service forecasts, to restore its SOC level. The lower-level controller is the MPC of Chapter 3, which adjusts the BESS's power injection to track real-time regulating power.

We compared the traditional scheduler implementing static capability curves and the scheduler with SOC-dependent power constraints, based on (i) the production of a feasible schedule and (ii) the respect of the current limits. The comparison was conducted for different initial SOC ranges, and the results showed that the proposed scheduler performed better in both comparisons. Specifically, it produced a schedule that respected the SOC limitations and significantly reduced the number of current violations by 28% in the SOC range of 10-50% and by 40% in the range of 60-90%. Therefore, implementing SOC-dependent power constraints into the problem formulation of the scheduler is of utmost importance to optimize its efficacy in power-intensive applications.

Chapter 5

Conclusions

5.1 Thesis summary

The thesis addressed the problem of controlling and scheduling the operations of a hydropower plant hybridized with a BESS. While controlling a conventional HPP is a well-established practice, the inclusion of a BESS requires a careful design of the strategy to implement the power set-point splitting between the hydraulic turbine and the BESS in order to improve plant performance in a meaningful and effective way, such as increasing the flexibility of the plants and reducing the wear-and-tear of the hydraulic components.

As further discussed in this chapter, this thesis' main and unique contribution to the state-of-the-art is embedding the notion of fatigue in the control processes of a hybrid HPP. This contribution was developed for the case of medium- and high-head HPPs with the objective of reducing the fatigue of the penstock, which, in these plants, is the most critical component.

Chapter 1 presented the challenges related to integrating more renewables into the power systems. It was explained that hydropower has a pivotal role in this transition because, besides being renewable, it offers balancing power to the grid by implementing grid frequency regulation. However, the combination of increasing regulation duties and aging infrastructure represent a challenge for HPP's operators as these might lead to excess stress on the plant's mechanical components. Retrofitting existing HPPs with BESSs (i.e., hybridization) is a technological solution that operators could adopt to alleviate the mechanical stress while still providing regulation services to the power grid.

Chapter 2 formulated linear models of the HPPs for control applications. These linear models were developed because of their mathematical tractability in MPC applications. In particular, implementing linear models into the MPC problem leads to a convex formulation of the underlying optimization problem, which is a fundamental property to achieve an (approximated) global optimum and acceptable computation time for deployment in real-life applications. The formulation and performance assessment of these linear models were presented at the *2021 IEEE PES Innovative Smart Grid Technologies Europe (ISGT Europe)* [66].

Chapter 3 investigated real-time controllers for penstock fatigue reduction in a medium-head hybrid HPP providing PFC. The underlying phenomena responsible for the fatigue on the penstock

(i.e., hydraulic transients and water hammer) were examined, and the methodology to assess the damage to the component was presented. A MPC for fatigue reduction was formulated, and its performance was evaluated in simulations and compared against a power set-point splitting strategy based on a low-pass filter, the current mainstream solution from the existing state-of-the-art. The results showed that the MPC achieves the best performance in terms of fatigue reduction and compliance with regulatory requirements for PFC. In addition, linear estimates of the power derived from the linear models of Chapter 2 were formulated in the MPC problem and used to determine the battery set-point. The hybrid plant was successfully controlled so that its power output met the same regulation capability as the original HPP while drastically reducing the penstock fatigue. This work originated three publications:

1. The Fatigue-aware filter has been presented at the *55th International Universities Power Engineering Conference (UPEC)* [48], receiving the "Top 5% Papers" distinction.

2. The MPC for penstock fatigue reduction in medium-head HPPs providing PFC has been published in *Sustainable Energy, Grids and Networks (SEGAN)* [37].

3. The MPC framework for hybrid medium- HPPs for the power set-point splitting problem has been published in *Electric Power Systems Research (EPSR)* [102].

Chapter 4 focused on schedulers for battery applications on fatigue reduction service. The objective is to ensure an adequate level of battery SOC to provide the prescribed services. A specific formulation for power-intensive applications was developed, accounting for the real power capability of the battery. The battery power estimation was performed using a model-based state-of-the-art technique, leading to SOC-dependant power constraints included in a control problem based on convex optimization. The scheduler was then combined into a two-layer control and scheduling formulation with the real-time MPC for fatigue reduction. The performance of the proposed scheduler was evaluated against a classical scheduler with static capability curves of the BESS. The formulation of the scheduling problem for power-intensive applications and the comparison against traditional schedulers from the literature is currently being described in a journal paper under preparation.

5.2 Analysis of the contributions

Each chapter of the thesis addressed a specific challenge related to the modelling, control, and optimization of hybrid HPPs. The main results and contributions from each chapter can be summarized as follows.

Chapter 2 contributed to the development and evaluation of linear models for HPPs to estimate key parameters such as torque and head with high accuracy. The EEC method was leveraged to describe pressure and discharge dynamics within the pipe, with the potential for extension to other hydraulic components. Hydraulic machines, specifically Francis and Kaplan turbines, were modelled using a quasi-static approach from the literature based on the characteristic curve of the machines to balance computational tractability and accuracy. The dynamic behaviour of the

synchronous generator was described using a second-order model to capture the dynamics of rotor speed and the power-angle relation. The 1-D linear model of a medium-head HPP with a Francis turbine and a low-head RoR with a Kaplan turbine was developed and validated against real hydro units modelled in the SIMSEN software for hydraulic simulation. The main non-linearities were analysed, and linear models of the HPPs were derived through linearization techniques. Finally, the performance of the proposed linear models was evaluated by comparing the linear estimates of turbine torque and head in the penstock against the non-linear model. The head and torque estimates were found to be crucial to fatigue and HPP output power estimation, respectively. The HPP linear model derivation corresponds to **Contribution 1**. The outcome of this contribution is two-fold:

1. linear models provide accurate estimations of torque and head around the linearization point with a relative mean absolute error of less than 10% for the torque and less than 1% for the head;

2. the developed linear models can be used in small signal applications, opening for the development of efficient model predictive control based on convex optimization.

Chapter 3 focused on the design of a receding horizon MPC to mitigate mechanical fatigue on the penstock in hybrid medium-head HPPs. The MPC leveraged the linear models developed in Chapter 2 to accurately reproduce the hydraulic phenomena associated with the penstock fatigue. The evaluation of the component's lifespan was performed using the stress-life method based on Wöhler's curves. The control trajectory designed by the MPC controller was successful in reducing the penstock damage and outperformed other controllers.

This method was used as the basic element to realize the power set-point splitting strategy for a hybrid HPP. In particular, the missing regulating power from the HPP due to the MPC action was compensated by using the BESS. The missing regulating power was estimated using the guide-vane-to-torque model developed in Chapter 2.

The hybrid controller's formulation corresponds to **Contribution 2**. The following are the major results associated with this contribution:

1. the MPC demonstrated a reduction in penstock damage compared to the standard HPP governor and other controllers for fatigue reduction from the literature;

2. the proposed convex formulation of the MPC problem was fast to solve (within tens of milliseconds) and is appropriate for real-life controller implementation;

3. the BESS's power required to decrease penstock fatigue was a small fraction of the HPP rated power. This implies that fatigue reduction services could be accomplished with relatively small BESSs; and

4. the hybrid HPP with MPC achieved the same level of regulation capability as the conventional HPP with the traditional governor.

In summary, these elements demonstrate the effectiveness of the MPC controller for mitigating penstock fatigue and maintaining regulation performance in hybrid medium-head HPPs.

Chapter 4 focused on scheduling BESS operations when used for the fatigue reduction services of Chapter 3. It was shown that, for power-intensive applications (such as the fatigue reduction service), classical schedulers from the literature would fail as they do not consider the power capability curve of the BESS (battery and converter) as a function of the battery's SOC and internal resistance. As a contribution to the state-of-the-art, a specific formulation for power-intensive applications was developed, accounting for the actual power capability of the BESS. The battery power capability was estimated using the VLOR method to formulate SOC-dependant power constraints into a scheduling problem based on convex optimization. Then, a strategy based on a statistical analysis fixed the upper and lower power and energy bounds of the PFC and SFC services provided.

The chapter showed that the proposed scheduler drastically reduced the number of current violations and produced feasible schedules for the fatigue reduction service compared to classical scheduler formulations from the existing literature.

The formulation of the scheduler for power-intensive applications corresponds to **Contribution 3**. It has been showed that:

1. the proposed scheduler generated feasible schedules for the fatigue reduction service when compared to the classical scheduler;

2. the proposed scheduler significantly reduced the number of current violations by 28% in the SOC range of 10-50% and by 40% in the range of 60-90%.

3. implementing SOC-dependent power constraints in the optimization problem was found to critically impact the scheduler's performance.

Overall, this thesis has made notable contributions to the modelling, control, and optimization of hydroelectric power plants that incorporate BESSs. The proposed models have accurately captured the hydraulic and electric dynamics of the system, while the control and optimization strategies have been successful in reducing mechanical fatigue on the penstock and enhancing the plant's regulation capability. These outcomes represent a significant advancement in the field of renewable energy systems and offer novel research opportunities for future endeavors.

5.3 Future perspectives

The research presented in this thesis has provided important advancements in control and scheduling algorithms for hybrid HPPs. In light of the proposed contributions, it is possible to identify several avenues for future research. They are discussed next.

Fatigue modelling of the mechanical components. Determining which fatigue model is best suited for modelling the fatigue of the penstock of hydropower plants is a complex problem that requires a detailed understanding of the specific loading conditions, material properties, and environmental factors involved. Many different fatigue models are available, each with its own strengths and limitations, and no single model can be considered universally superior for all applications.

One of the main challenges in fatigue modelling is the difficulty in accurately capturing the complex interactions between microstructural features and loading conditions. Fatigue failure is

typically initiated at the microscale, and the behavior of individual microstructural features, such as cracks and defects, can significantly impact the overall fatigue response. However, accurately modelling these interactions is a significant challenge due to the complexity of the underlying physics and the lack of experimental data.

Despite these challenges, there has been significant progress in the development of fatigue models in recent years. New approaches, such as machine learning, data-driven modelling and multi-scale models [103–108], which combine different modelling approaches at different length scales, are being explored as a way to capture the complex interactions between microstructural features and loading conditions.

In conclusion, continued research and development in this area is essential for improving our understanding of the behavior of materials and structures under cyclic loading. By developing more accurate and reliable fatigue models, we can better predict and prevent fatigue failure.

Improved BESS modelling. The central contribution of this thesis was to formulate explicit stress constraints in an MPC of an HPP and to show how this can be a viable strategy for implementing the power set-point splitting in a hybrid HPP. We proposed a preliminary version of the hybrid controller by implementing a simple model of the BESS. However, a more comprehensive model of the BESS could be considered in the real-time control problem, e.g., in [26]. Battery models that are suitable for this purpose are equivalent circuit models [109, 110], which can be expressed as a linear system of equations, or extended Kalman filter models [111, 112], which can capture the nonlinear behavior of the battery while still being amenable to convex optimization. Additionally, some researchers have proposed using simplified, empirical models that can be represented by convex functions, such as the polynomial model [113, 114], to describe the battery's behavior. These models can be optimized using convex optimization techniques and have been shown to be effective in controlling battery systems in certain applications.

Moreover, this thesis did not specifically address BESS degradation based on the practical consideration that maintenance costs for the mechanical components (e.g., replacing a penstock) could be much larger than replacing the BESS. However, including BESS degradation constraints to prolong BESS's lifespan could be a valuable avenue to explore further. For example, authors in [115] discuss cycle-based degradation models, specifically focusing on the rain-flow algorithm for cycle counting, which is electrochemically accurate, and establish the convexity of the rain-flow cycle-based degradation cost concerning charging and discharging power. This convexity ensures easy incorporation of the degradation model in the optimization problem.

Extension to other types of plants. The analysis we conducted on fatigue reduction in penstocks of medium-head HPPs can also be generalized to other types of power plants. In this context, the key challenge is identifying the critical component that is most vulnerable to fatigue and replicating the fatigue on that component to develop a closed-form expression. This formulation can then be included in MPC algorithms to generate a control trajectory that minimizes the impact of fatigue and extends the power plant's lifespan.

In run-of-river plants, fatigue phenomena are associated with the servomotor mechanism of the Kaplan turbine. Due to the interplay of multiple factors, modelling these phenomena can be challenging. Nonetheless, diverse formulations can be implemented in the optimization problem to

decrease fatigue in these components. An idea to enhance the flexibility of a Kaplan turbine in a run-of-river plant is presented in Appendix D. However, the feasibility of this approach is limited by the forbidden zone, which defines the safe operating range of the turbine. A thorough investigation is therefore required to verify the feasibility of the proposed method.

In summary, developing an explicit formulation of the mechanical stresses and incorporating closed-formulations into MPC algorithms to generate control trajectories that minimize the impact of fatigue is a promising approach that should be pursued in industrial practices.

Appendix A

Model and controller framework validation

The models described in Chapter 2 have been developed in the Matlab environment and validated against SIMSEN [116, 117], a commercial software used for simulating hydropower plants. The validation process involved assessing relevant hydraulic quantities during four different scenarios: i) water hammer caused by a valve closure, ii) turbine's step response, iii) emergency shutdown, and iv) ENTSOE qualification tests for PFC and SFC. Hereafter, the validation of a medium-head and low-head run-of-river HPP, equipped with Francis and Kaplan turbines, is presented.

A.1 Medium-head HPP model and controller validation

The validation concerns the plant of the hydroelectric power plant discussed in the case study of Section 3.6.1. This plant is composed of a 230 MW medium-head HPP that employs a Francis turbine and a 1,100-meter-long open-air penstock connecting the powerhouse to the upper-level reservoir, which is situated at a height difference of 315 meters.

Water hammer

The water hammer effect in the penstock resulting from a closure of the guide vane at t=1 s is shown in Fig. A.1. The discharge at the downstream valve (red line) decreases to zero within the valve closure time, while the head at the valve (blue line) attains its maximum amplitude. The overpressure wave propagates back and forth the pipe, decreasing gradually due to the friction of the penstock's wall. The solid lines represent the quantities obtained from Matlab, while the dashed lines represent those from SIMSEN. The comparison between the two models demonstrates good agreement.

Francis step response

The response of the Francis turbine to a 0.1 pu change in the guide vane is depicted in Fig. A.2. As illustrated, the simulation exhibits an inverse response of the head when the vane is closed, i.e.,

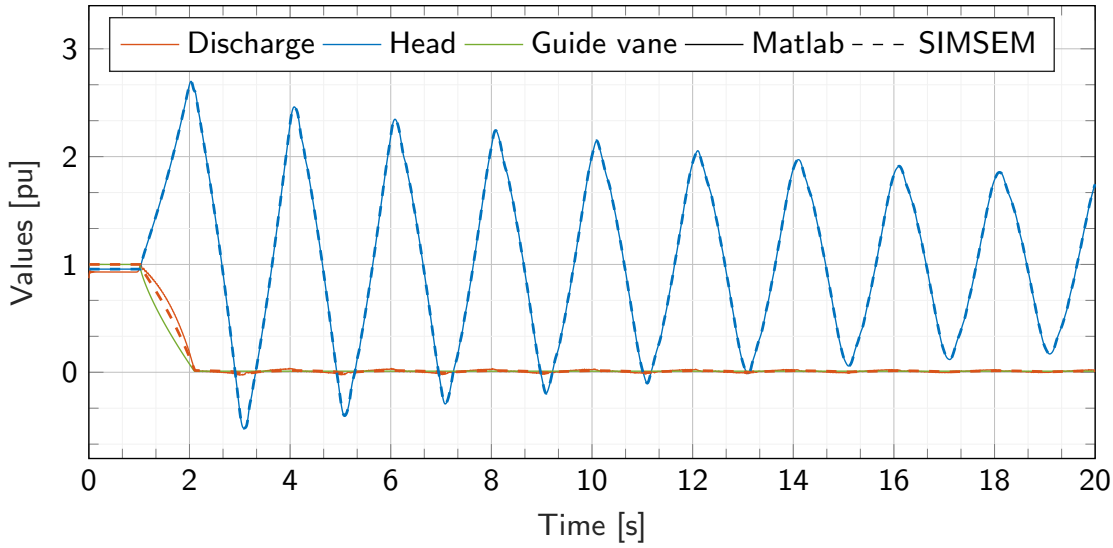

Figure A.1: Water hammer: heads and discharges at downstream valve resulting from a sudden closure of the valve at t=1 s.

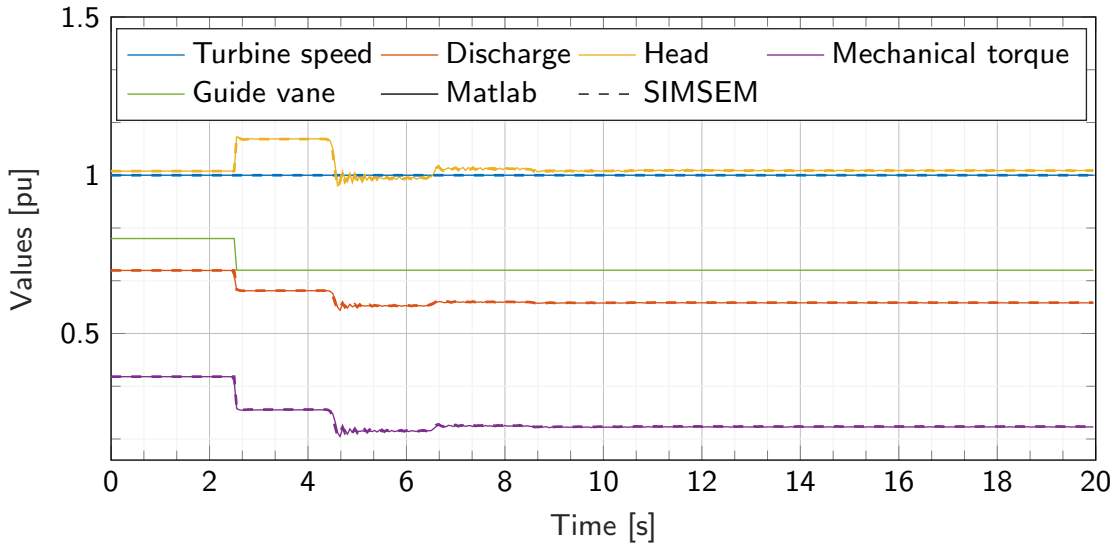

Figure A.2: Francis turbine's step response: heads, discharges and mechanical torques resulting from a guide vane step of 0.1 pu at t=2.5 s.

the flow begins to reduce, but the water head suddenly increases due to the smaller passage. The comparison between the two models reveals a good agreement.

Medium-head HPP emergency shutdown

Fig. A.3 illustrates the emergency shutdown process of the medium-head hydropower plant. At t=10 s, the electromagnetic torque from the fully open guide vane is set to zero, and the guide vane starts closing following a bi-linear closing law. As a result, the turbine experiences a runaway

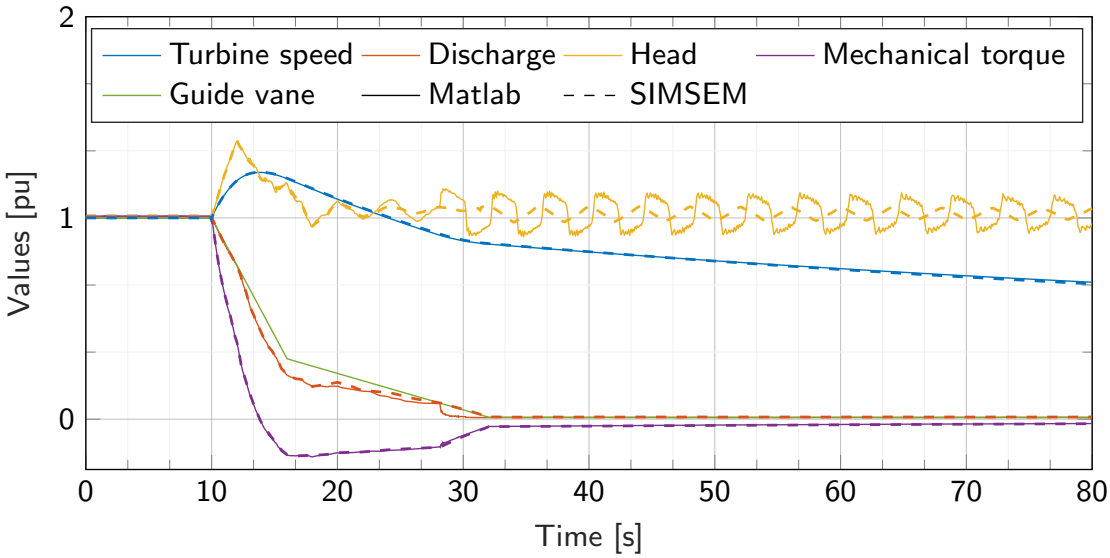

Figure A.3: Medium-head HPP emergency shutdown: heads, discharges, mechanical torques and guide vane resulting from an electromagnetic torque loss at t=10 s.

speed, while the torque and discharge decrease to zero. The full closure of the guide vane triggers a water hammer in the penstock, leading to oscillations in the hydraulic head. The comparison between the two models shows a good match, except for less damped oscillations in the head in our models, which can be attributed to water viscosity.

PFC test

The validation of the controller's dynamic performance involves ensuring that the plant satisfies the ENTSOE qualification test for primary frequency control [41]. The test requires the plant to be able to deliver 50% and 100% of its total power output within 15 and 30 seconds, respectively, following a ramp variation of the frequency signal of 0.2 Hz over 10 seconds, while remaining within a specified envelope.

For the medium-head hydropower plant in the case study, the permanent speed droop is set at 4%, which corresponds to a 10% variation in the nominal power P_n from the operating point. Additionally, the power must remain within upper and lower boundaries. The results for a downward frequency ramp are presented in Fig. A.4, demonstrating that the controller's performance meets the requirements of the qualification test.

SCF test

The secondary frequency control test [42] consists of four ramps, involving a variation of the power set-point within 800 and 133 seconds, which is also referred to as the "emergency ramp". The power level is then maintained for 15 minutes. Figs.A.5-A.6 depict a ramping up of 133 and 800 s, respectively, which corresponds to 25% of the nominal power (yellow line), the response of the plant (blue line), and the tolerance interval (grey dashed lines). The plant successfully passes the

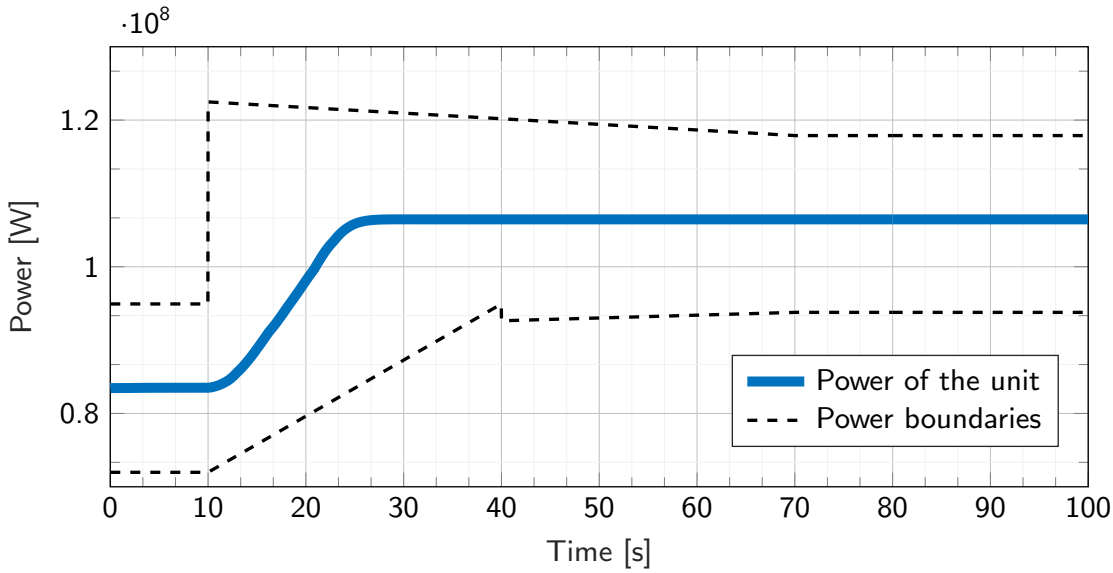

Figure A.4: Active power time evolution resulting from PFC test case with frequency drop of Δf = -200 mHz and permanent speed droop R = 4%.

SFC qualification test.

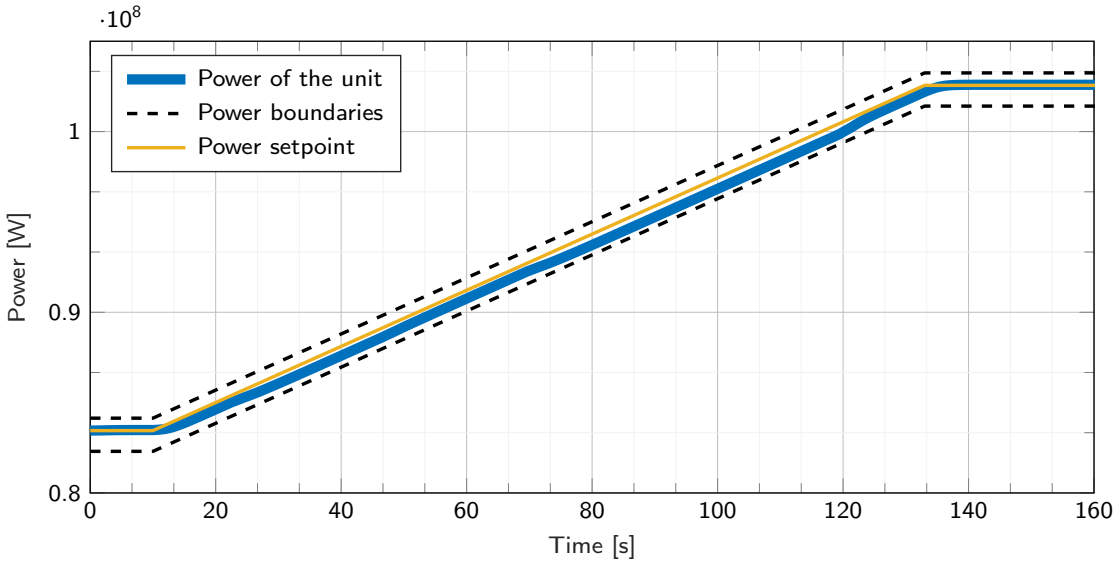

Figure A.5: Active power time evolution resulting from SFC test case with 133 s power set-point ramping ("emergency ramp"), corresponding to +25% of the nominal power and permanent speed droop R = 4%.

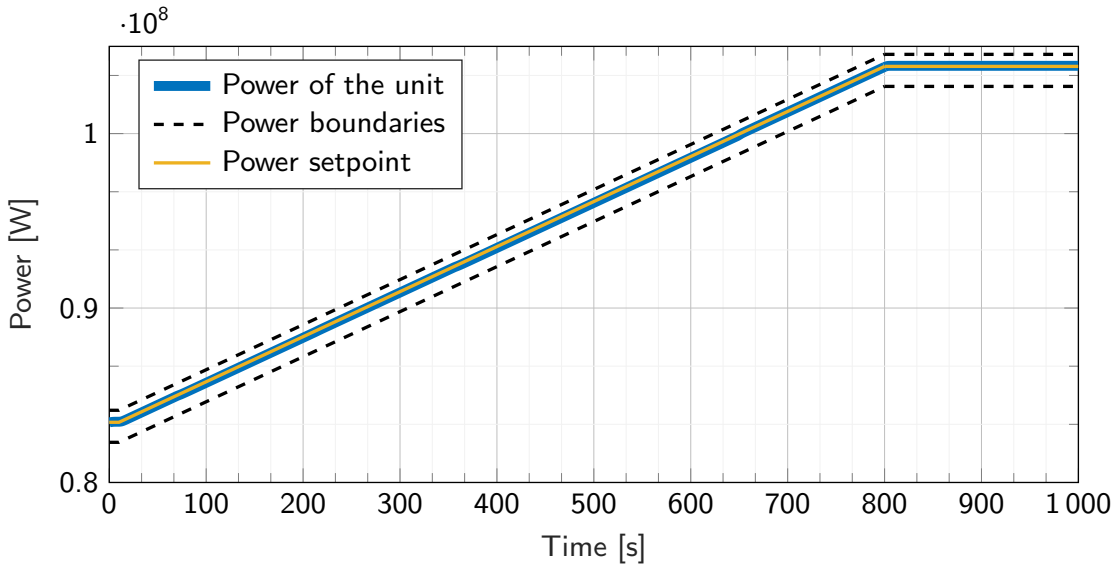

Figure A.6: Active power time evolution resulting from SFC test case with 800 s power set-point ramping corresponding to +25% of the nominal power and permanent speed droop R = 4%.

A.2 Run-of-river HPP model and controller validation

The case study plant is a RoR hydropower plant with a nominal power of 156 MW, comprising of four low-head Kaplan turbine units. The hydraulic circuits include the water intake and the spiral case. In this study, we focus on the modelling of one Kaplan turbine unit as it is used for providing ancillary services.

Kaplan step response

Fig. A.7 displays the step response of a Kaplan turbine resulting from a change of 0.1 pu on the guide vane and 0.125 pu on the blade pitch. The simulation illustrates the behavior of the head, discharge, and mechanical torque. The comparison between the developed model and the results from the reference shows that the model is validated.

RoR plant emergency shutdown

The emergency shutdown of the RoR hydropower plant is illustrated in Fig. A.8. The comparison between the two simulation framework shows a good agreement, except for a minor discrepancy in the calculation of the turbine speed.

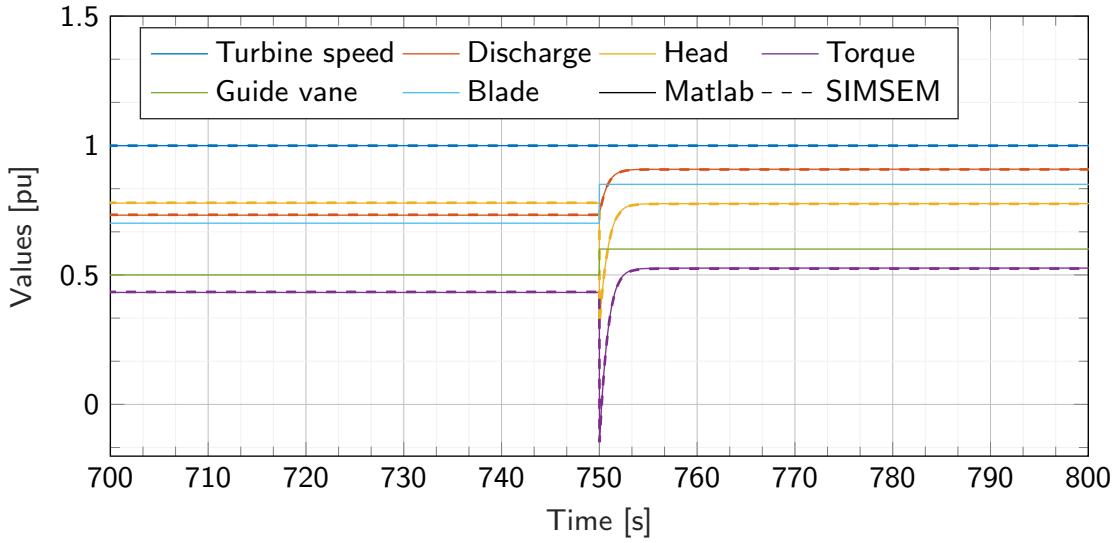

Figure A.7: Kaplan turbine's double step response: heads, discharges and mechanical torques resulting from a guide vane step of 0.1 pu and blade pitch step of 0.125 pu at t=750 s.

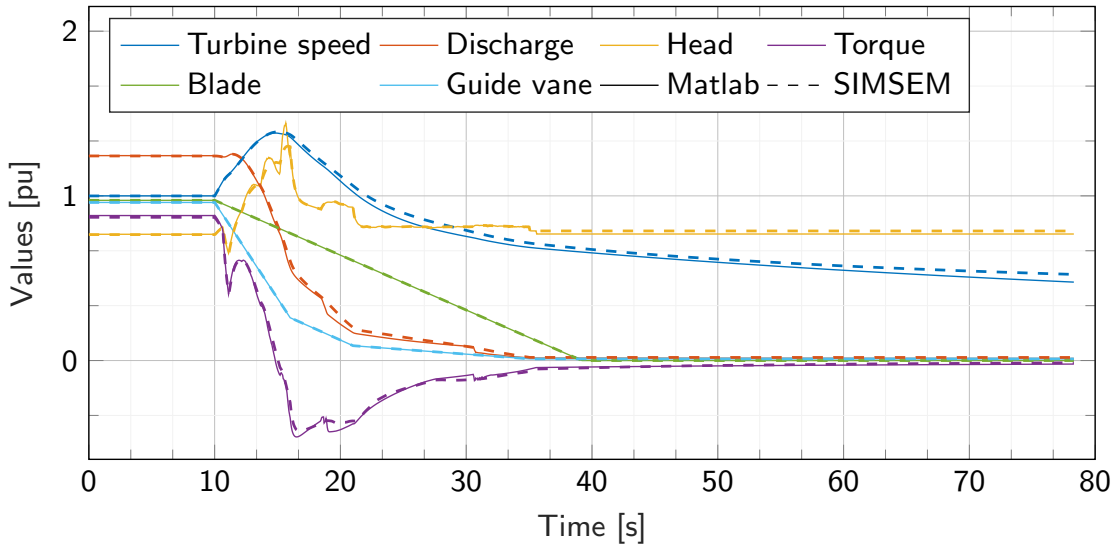

Figure A.8: RoR plant emergency shutdown: heads, discharges, mechanical torques and guide vane resulting from an electromagnetic torque loss at t=10 s.

PFC test

To validate the primary frequency control of the RoR hydropower plant, a test was conducted with a downward frequency ramp of 200 mHz. The governor's permanent speed droop was set at 5%, and the Kaplan unit was expected to deliver the required output power within the time constraints and remain within the power boundaries. The test results, shown in Fig. A.9, demonstrate that the plant's PFC performance meets the requirements.

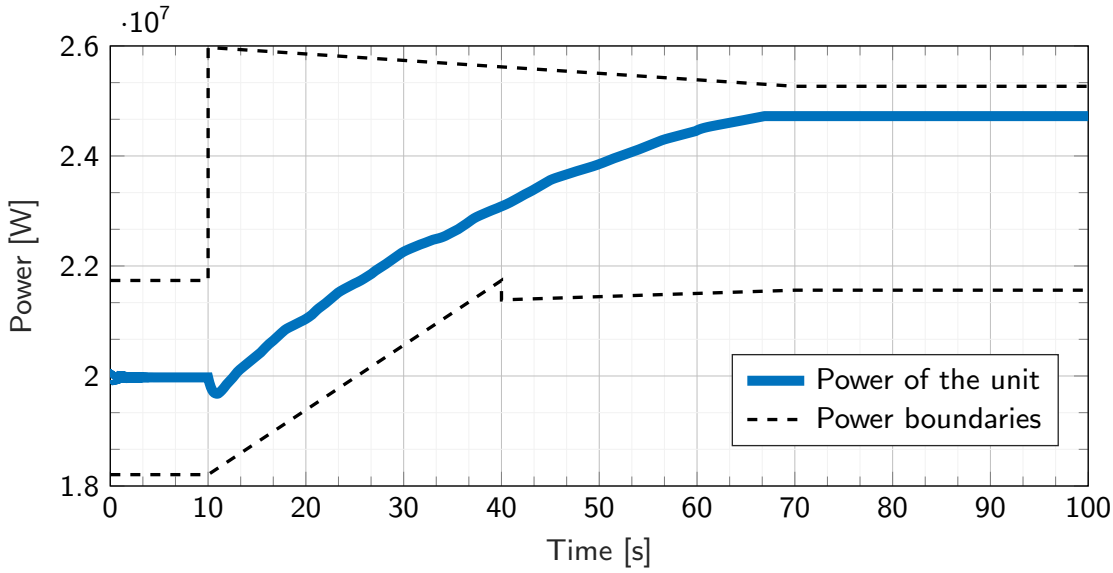

Figure A.9: Kaplan unit's output power time evolution with frequency drop of Δf = -200 mHz and permanent speed droop R = 5%.

Appendix B

Fatigue-aware filter

As mentioned in Section 3.4, stress cycles that fall below the effective fatigue limit threshold do not contribute to relevant penstock fatigue. In this section, we introduce the fatigue-aware filter, which aims to adjust the HPP power set-point to prevent cycles that exceed the effective fatigue limit of the penstock. This is achieved with the control loop shown in Fig. B.1, where the input of the system is the HPP's frequency set-point. The HPP model, $G(s)$ [40], is utilized to calculate the resulting guide vane opening y, which is subsequently applied to the model $H(s)/y(s)$ to determine the head at a specific section of the penstock. In this context, the penstock element with the largest stress variations is considered.

To ensure that stress variations do not exceed the fatigue limit, the stress is constrained within a specific interval, as in (3.8). The filtered stress σ^* is translated to H^* by applying the inverse of (3.5). From the trimmed head H^*, the inverse transfer function model $y(s)/H(s)$ and the inverse HPP's model $G^{-1}(s)$ ([1]) are used to reconstruct the guide vane opening and power set-point, respectively.

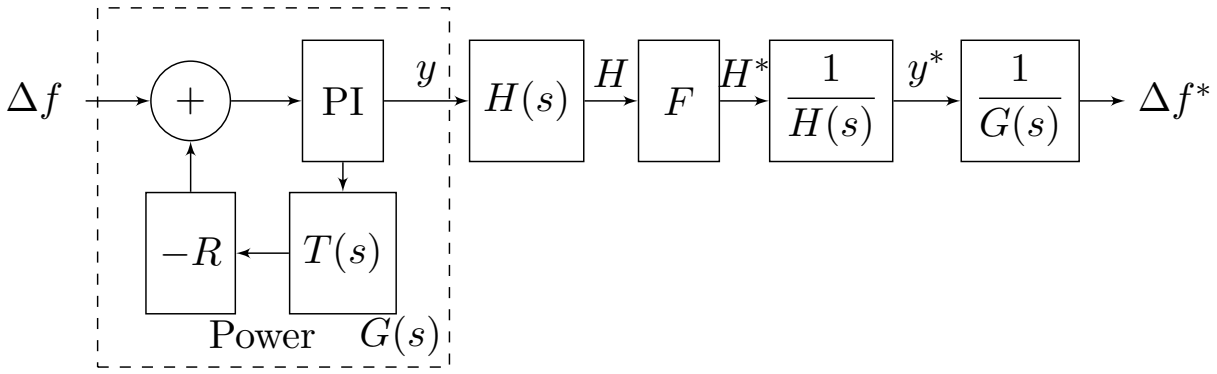

Figure B.1: Fatigue-aware filter. The frequency deviation Δf (i.e., frequency set-point minus the measured frequency) is used to compute guide vane position y and head H in the penstock's most fatigue-critical element. The filtered head is reconverted to Δf^* by applying the inverse modelling tool-chain.

[1] This requires the model $G(s)$ to be invertible.

To accurately replicate the behavior of the detailed simulation of the plant, a parameter estimation procedure is required for the reduced-order model $G(s)$. This is due to a different interpretation of the input control signal between [40] and the current model. In [40], the input control signal is referred to as gate opening g, while in the current model, it is referred to as guide vane y. To address this difference, we adopt the quadratic relationship between the two proposed by the authors of [118]:

$$g(y) = d_0 + d_1 \cdot y + d_2 \cdot y^2. \tag{B.1}$$

where d_0, d_1 and d_2 are parameters found by minimizing the root mean square deviation between the two models.

Appendix C

Model predictive control formulation

C.1 Derivation of the transition matrices for MPC (Single-input case).

We consider the following linear discrete state-space model with one input:

$$x(t+1) = Ax(t) + Bu(t) \tag{C.1}$$
$$y(t) = Cx(t) + Du(t), \tag{C.2}$$

where $x(t) \in \mathbb{R}^n$ is the state vector at the discrete time interval t, $u(t) \in \mathbb{R}$ is the input, $y \in \mathbb{R}$ is the system output, A is the $n \times n$ system matrix, B is the $n \times 1$ input matrix, C is the $1 \times n$ output matrix, and the scalar D is the feed-forward gain. The evolution in time of the state vector x from a known initial state $x(0)$ as a function of a given input sequence $u(0), u(1), \ldots, u(T)$ is

$$x(1) = Ax(0) + Bu(0) \tag{C.3}$$
$$\begin{aligned} x(2) &= Ax(1) + Bu(1) = A(Ax(0) + Bu(0)) + Bu(1) = \\ &= A^2x(0) + ABu(0) + Bu(1) \end{aligned} \tag{C.4}$$
$$\begin{aligned} x(3) &= Ax(2) + Bu(2) = \\ &= A^3x(0) + A^2Bu(0) + ABu(1) + Bu(2). \end{aligned} \tag{C.5}$$

Iterating until T yields

$$x(T) = A^T x(0) + A^{T-1}Bu(0) + \cdots + A^0 Bu(T-1), \tag{C.6}$$

and

$$y(T) = CA^T x(0) + CA^{T-1}Bu(0) + \cdots + CA^0 Bu(T-1) + Du(T). \tag{C.7}$$

Using matrix products, the evolution in time of the system output y can be written as

$$\begin{bmatrix} y(0) \\ y(1) \\ y(2) \\ \vdots \\ y(T) \end{bmatrix} = \begin{bmatrix} CA^0 \\ CA^1 \\ CA^2 \\ \vdots \\ CA^T \end{bmatrix} x(0) + \begin{bmatrix} D & 0 & 0 & \dots & 0 & 0 \\ CA^0B & D & 0 & \dots & 0 & 0 \\ CA^1B & CA^0B & 0 & \dots & 0 & 0 \\ \vdots & \vdots & \vdots & \ddots & \vdots & \vdots \\ CA^{T-1}B & CA^{T-2}B & CA^{T-3}B & \dots & CA^0B & D \end{bmatrix} \begin{bmatrix} u(0) \\ u(1) \\ u(2) \\ \vdots \\ u(T-1) \\ u(T) \end{bmatrix}, \quad \text{(C.8)}$$

or, in a compact form:

$$y = \phi x(0) + \psi u, \quad \text{(C.9)}$$

where matrices ϕ and ψ, whose definition follows directly from (C.8), are entirely built based on the knowledge of the state-space model.

We can write (C.7) in a more compact form as:

$$y(T) = \phi_T x(0) + \psi_T u, \quad \text{(C.10)}$$

where ϕ_T and ψ_T are, respectively, the T-th row (counting from zero) of matrix ϕ and matrix ψ.

Extension to multiple inputs. With an additional input $\boldsymbol{r} = r(0), \dots, r(T)$, the state-space model is:

$$x(t+1) = Ax(t) + B^{(u)}u(t) + B^{(r)}r(t) \quad \text{(C.11)}$$

$$y(t) = Cx(t) + D^{(u)}u(t) + D^{(r)}r(t). \quad \text{(C.12)}$$

The system output is written by applying the transformation ψ_r to $\boldsymbol{r}$:

$$\boldsymbol{y} = \phi x_0 + \psi^{(u)}\boldsymbol{u} + \psi^{(r)}\boldsymbol{r}. \quad \text{(C.13)}$$

C.2 Fatigue reduction without feedforward matrix

With a more compact and adjusted notation, (3.14d) is:

$$(\psi_t - \psi_{t-1})\, \boldsymbol{y}_t \leq \overline{h} \quad \text{(C.14)}$$

where bold type-faced $\boldsymbol{y}_t$ is the column vector

$$\boldsymbol{y}_t = \begin{bmatrix} y(t-T) & \dots & y(t) \end{bmatrix}'. \quad \text{(C.15)}$$

and ψ_t is the row of matrix ψ such that:

$$\psi_t \boldsymbol{y}_t = h(t). \quad \text{(C.16)}$$

If the last element of ψ_t is zero, we have that changing the guide vane opening does not instantaneously impact on the head. Being (C.14) fully determined by the historic control action, it is not

use for active decision making at time t. However, we can still use the same notion to implement the following constraint:

$$(\psi_{t+1} - \psi_t)\, \boldsymbol{y}_{t+1} \leq \overline{h}. \tag{C.17}$$

Let $Z = (\psi_{t+1} - \psi_t)$, we can rewrite the constraint above as:

$$\begin{bmatrix} Z(t-T) & \dots & Z(t) & Z(t+1) \end{bmatrix} \begin{bmatrix} y(t-T) \\ \vdots \\ y(t) \\ y(t+1) \end{bmatrix} \leq \overline{h} \tag{C.18}$$

which we can solve for $y(t)$ so as to determine our control action. We note that $Z(t+1)$ is zero because it is assumed so, so $y(t+1)$ can be omitted from the formulation.

Follow-up to simplify notation We rewrite (3.14d) for two inputs in the following form:

$$\psi_{t+1}^{(1)} u^{(1)} + \psi_{t+1}^{(2)} u^{(2)} \leq \overline{h} \tag{C.19}$$

$$\psi_{t+1}^{(1)} u^{(1)} + \psi_{t+1}^{(2)} u^{(2)} \geq \underline{h} \tag{C.20}$$

where:

- dependency of psi from T bar is omitted,
- $\psi_{t+1}^{(1)}$ denotes the psi for the first input, and similarly for the second;
- $u^{(1)}$ is the first historic input, and $u^{(2)}$ the second; we assume the first is the controllable one;
- h-bar and h-underbar are the upper and lower bounds suitably derived from above.

Assuming the variable in expressions (C.19) and (C.20) is the last element of vector $u^{(1)}$, we now want to rewrite them so that the variable and known terms appear on the left- and right-hand side, respectively, of the expressions. We start by noting that the following row-column product

$$\begin{bmatrix} \psi_{t+1}^{(1)}(1) & \dots & \psi_{t+1}^{(1)}(T+1) & \psi_{t+1}^{(1)}(T+2) \end{bmatrix} \begin{bmatrix} u^{(1)}(t-T) \\ \vdots \\ u^{(1)}(t) \\ u^{(1)}(t+1) \end{bmatrix} \tag{C.21}$$

can be rewritten as

$$\underbrace{\begin{bmatrix} \psi_{t+1}^{(1)}(1) & \dots & \psi_{t+1}^{(1)}(T+1) \end{bmatrix}}_{\overline{A}} \underbrace{\begin{bmatrix} u^{(1)}(t-T) \\ \vdots \\ u^{(1)}(t) \end{bmatrix}}_{\overline{x}} + \underbrace{\psi_{t+1}^{(1)}(T+2)}_{\underline{A}} \underbrace{u^{(1)}(t+1)}_{\underline{x}}. \tag{C.22}$$

We can find two matrices, $\overline{M}$ and $\underline{M}$, such that

$$\underbrace{\psi_{t+1}^{(1)} \overline{M}'}_{\overline{A}} \underbrace{\overline{M} u^{(1)}}_{\overline{x}} + \underbrace{\psi_{t+1}^{(1)} \underline{M}'}_{\underline{A}} \underbrace{\underline{M} u^{(1)}}_{\underline{x}} \tag{C.23}$$

By using the transformation above, we can rewrite (C.19)

$$\psi_{t+1}^{(1)} u^{(1)} + \psi_{t+1}^{(2)} u^{(2)} \leq \overline{h}$$

as

$$\psi_{t+1}^{(1)} \overline{M}' \overline{M} u^{(1)} + \psi_{t+1}^{(1)} \underline{M}' x + \psi_{t+1}^{(2)} u^{(2)} \leq \overline{h}. \tag{C.24}$$

Re-arraging, we get:

$$\psi_{t+1}^{(1)} \underline{M}' x \leq \overline{h} - \psi_{t+1}^{(1)} \overline{M}' \overline{M} u^{(1)} - \psi_{t+1}^{(2)} u^{(2)} \tag{C.25}$$

that we can solve for x.

Appendix D

Achieving Higher Ramping Rates in a Run-of-River HPP

This section presents a method to enhance the dynamic response of run-of-river hydropower plants equipped with Kaplan turbines by trading off generation efficiency for response time. The proposed approach involves the development of a new cam curve, referred to as the "Flex-cam" curve, which is compared to the conventional on-cam curve in terms of various performance metrics, including output power ramping time, discharge control action, frequency signal tracking, and wear assessment of guide vanes and runner blades. The findings demonstrate that the Flex-cam curve enables better response time with the same hardware components. Nevertheless, off-cam operations may generate pressure transients and affect stable operation and turbine lifespan. Future studies will explore the feasibility of operating points on the Flex-cam curve.

D.1 Problem statement

Typically, run-of-river hydropower plants are regulated to maintain water levels within a specific range to enable navigation and other human activities. To extract the highest power generation from a given discharge, a Kaplan turbine is commonly used and operated at the highest conversion efficiency. Kaplan turbines offer two degrees of freedom: the guide vane opening and blade position. These two elements are regulated to ensure the highest efficiency of mechanical conversion for a given water discharge. The on-cam curve represents the relationship between the guide vane opening and blade position, resulting in the highest efficiency.

The objective of this analysis is to determine the relationship between guide vane opening and blade position that achieves maximum flexibility, defined as the operational points that determine the highest response time of the hydropower plant's power output. The outcome of this study is a new cam curve, known as the Flex-cam curve. We propose two methods to achieve this: the first is an experimental approach based on numerical simulation using a modelling framework of a run-of-river hydropower plant, while the second approach arises from analytical considerations of the turbine's model.

D.2 Methods

D.2.1 Experimental derivation of the flexibility curve

This section presents a straightforward and intuitive method to evaluate the ramping rate of a run-of-river hydropower plant (HPP) at different operational points, namely guide vane and blade pitch angles. The method involves numerically differentiating the power output with respect to time while sweeping different operational conditions. This approach can be applied to both simulation models and measurements from a real power plant. However, the method requires a significant amount of measurements and experiments, which motivates the development of a semi-analytical formulation discussed in the next section. The purpose of this investigation is to identify the operational conditions that yield the largest power output variation with the minimum time. The first step in this approach is to define the curve $P' = dP/dt$. This curve is evaluated using a non-linear model framework in MATLAB software, assuming a constant rotor speed N and constant gross head H_g of the Kaplan turbine. The time derivative of the power output can be expressed as:

$$P' = \frac{\Delta P}{\Delta \beta} \cdot \frac{\Delta \beta}{\Delta t} + \frac{\Delta P}{\Delta y} \cdot \frac{\Delta y}{\Delta t} = \left.\frac{\Delta P}{\Delta t}\right|_{y=const} + \left.\frac{\Delta P}{\Delta t}\right|_{\beta=const}, \tag{D.1}$$

where β and y are the runner blade pitch angle and guide vane opening, respectively. The last term in the equation is obtained by ramping the guide vane opening from 0 to 1 [pu] with increments of 0.025 [pu] while fixing β. The numerical derivative is computed at a fixed value of β while ensuring that the power output reaches its steady-state value for each step of the guide vane. The same procedure is repeated for different values of β and y. The second-to-last term in Eq. (D.1) is derived similarly by switching y and β. The procedure is summarised in the following algorithm pseudo-code:

Algorithm 1 Experimental flexibility assessment

Input: Guide vane y and runner blade β grid values

Output: P' surface

Initialisation :

0: set gross head H_g and speed N
0: set Δt
0: build y and β ramp steps
0: **for** $i = 1$ to length(β) **do**
0: **for** $j = 1$ to length(y ramp) **do**
0: P_{out} = HPP_model(y ramp, β);
0: $P'|_{\beta=const}(i,j) = \Delta P/\Delta t$;
0: **end for**
0: **end for**
1: **return** switch y and β to find $P'|_{y=const}(i,j)$
1: $P' = P'|_{y=const}(i,j) + P'|_{\beta=const}(j,i)$; =0

D.2.2 Semi-analytical derivation of the flexibility curve

By incorporating modelling considerations on the Kaplan turbine, it becomes feasible to compute the ramping rate through a semi-analytical approach. This method offers the potential to investigate the influence of other quantities, such as head, on the turbine's flexibility. Furthermore, it requires fewer experiments to determine the flexibility.

The power output of a hydropower plant equipped with a Kaplan turbine is a function of the rotational speed, N, the blade pitch angle, β, the guide vane opening, y, and time t as expressed by the equation:

$$P = f(N, \beta, y, t). \tag{D.2}$$

The time derivative of Eq. (D.2) can be determined through the chain rule. Assuming a constant rotational speed of the turbine, this leads to:

$$P' = \frac{dP}{dt} = \frac{df}{d\beta}\frac{d\beta}{dt} + \frac{df}{dy}\frac{dy}{dt}. \tag{D.3}$$

In hydraulic turbine models, quasi-static models are often utilized to represent the dynamic behavior of the turbine as a series of steady-state operating points [54]. This approach, which relies on characteristic curves, provides the dynamic parameters of the turbine during transients with sufficient accuracy in all flow regimes [63]. Thus, quasi-static modelling is particularly advantageous for power system simulations.

By virtue of the quasi-static modelling approach, presented in Chapter 2, the output power in (D.2) can be expressed in terms of the torque dimensional factor T_{11}. Assuming the rotational speed N as constant, it leads to:

$$P \propto T_{11}(\beta, y) \tag{D.4}$$

where all constants are assumed embedded in the function $T_{11}(\cdot)$. The derivative of the power with respect to the time is:

$$P' = \frac{dP}{dt} \propto \frac{dT_{11}(\beta, y)}{dt} = \frac{dT_{11}}{d\beta}\frac{d\beta}{dt} + \frac{dT_{11}}{dy}\frac{dy}{dt}. \tag{D.5}$$

Assuming y and β varies with time with a first order system of linear ramping introduced by the guide vane and runner blade servo mechanism $r_y(t)$ and $r_\beta(t)$, the expression above becomes:

$$P' \propto r_\beta(t)\frac{dT_{11}(\beta, y)}{d\beta} + r_y(t)\frac{dT_{11}(\beta, y)}{dy}. \tag{D.6}$$

Therefore, the computation of the P' curve can be simplified by linearizing the $T_{11}(\beta, y)$ curve with respect to the blade pitch and guide vane opening. This curve is obtained from the turbine's characteristic curves, as previously described, which are provided by the turbine's manufacturers and based on actual tests. The comparison and validation of the experimental and semi-analytical methods will be demonstrated in Section D.3.1. The subsequent section outlines the case study examined in this work.

D.2.3 Case study

The 156 MW HPP being studied in this work is located on the Rhine river in France and consists of four Kaplan turbines. However, only one turbine was modelled in this study as it is specifically used for PFC. The simulation framework used is based on the non-linear modelling approach described in the earlier sections and is being validated against the commercial software SIMSEN in Appendix A. During PFC, the HPP governor tracks a frequency set-point signal, which is accomplished by adjusting the guide vane opening of the turbine y_c based on measurements of gross head and discharge, as well as the experimental function $y_c = f(Q, H)$. The difference between the set-point and the calculated guide vane opening is multiplied by the gain K and added to the frequency error e_f, which is the difference between the set-point value of 50 Hz and the measured frequency. The input error of the PID is obtained by multiplying this value by the speed droop coefficient, which is set to 5%. The PID processes the error and the servo-motor adjusts the guide vane opening of the Kaplan turbine y, while the blade pitch angle β is obtained using the integrated on-cam characteristic of the turbine to ensure maximum efficiency at the given guide vane opening and gross head conditions. The governor model is developed in shown in Fig. D.1.

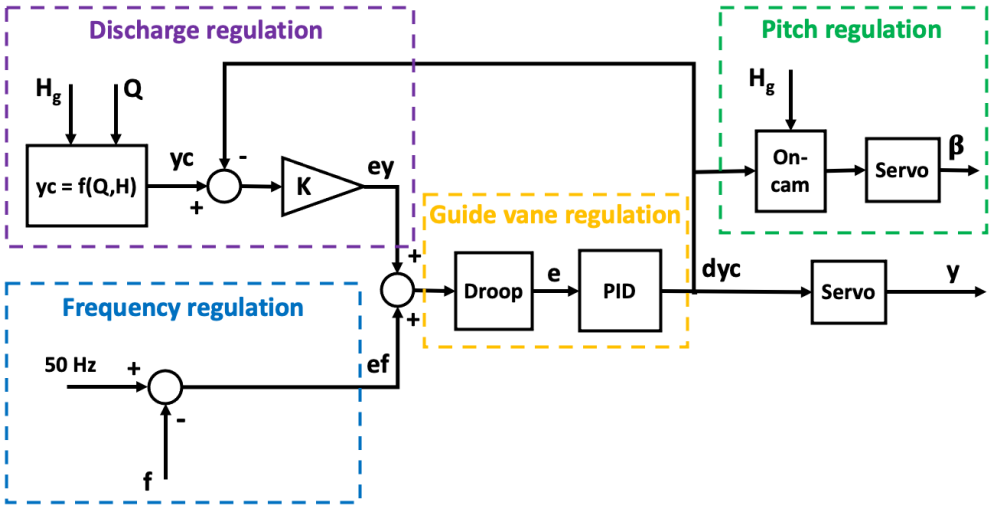

Figure D.1: HPP governor block diagram

The Flex-cam curve will be used instead of the on-cam block to determine the blade pitch angle β that maximizes flexibility, based on the guide vane opening and the gross head.

D.3 Results and Discussion

This section describes the derivation and assessment of the Flex-cam curve, which is used to determine the ramping rate capacities of the HPP through both experimental and analytical approaches. Firstly, the assessment of the curve is presented. Then, the performance of the HPP when operated with the traditional on-cam curve, which corresponds to the highest efficiency, is compared with that of the Flex-cam curve. Finally, the last part of the section discusses the origin of the flexibility through analytical investigations and presents some considerations on the topic.

D.3.1 Flex-cam curve

The flexibility heat map for the ramping rate capacities, obtained using both experimental and analytical methods, is presented in Fig. D.2 for a synchronous operation with a gross head $H_g = 11.79$ [m] and $N = 83.3$ [rpm]. The guide vane and beta values less than 0.2 [pu] are excluded, as they are not typical operating conditions for the plant. The upper-left region of the figure is also excluded as the turbine efficiency is below 30%, resulting in a low level of output power. The

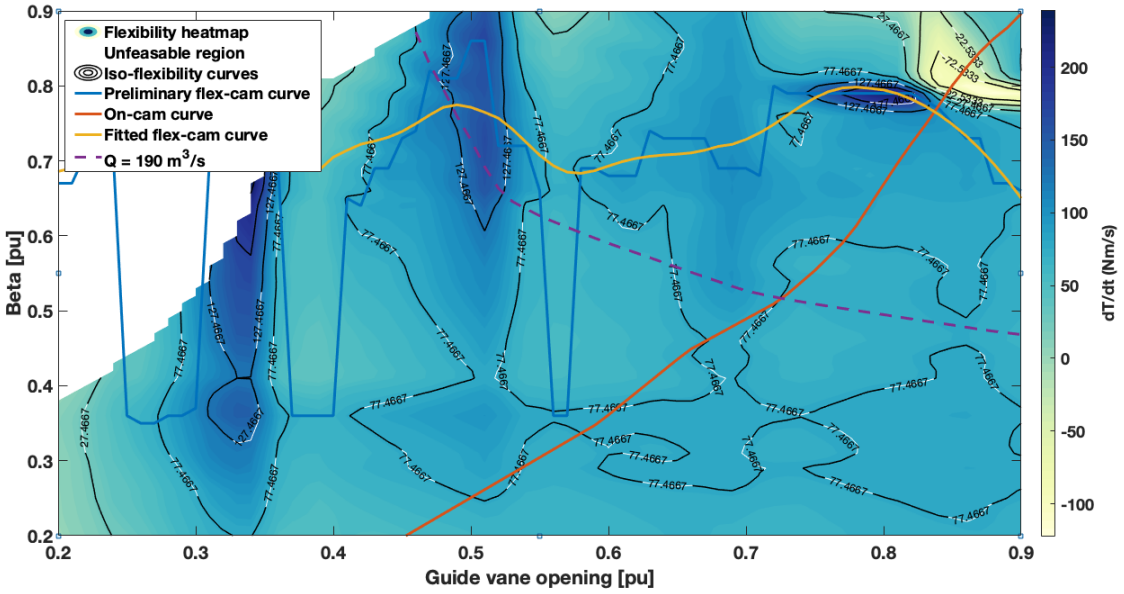

Figure D.2: Flexibility heat map of the run-of-river HPP and cam-curves for $H_g = 11.79$ [m] and $N = 83.3$ [rpm].

flexibility heat map demonstrates significant variations in ramping rates throughout the operating range of the HPP. The Flex-cam curve is determined as the trajectory of pairs (β, y) with the maximum ramping rate. The preliminary representation of the Flex-cam is shown as a solid blue line in Fig. (D.2). However, the curve exhibits abrupt changes in β around guide vanes corresponding to $y = 0.3, 0.4, 0.55$ [pu], making it impractical. To overcome this issue, a confidence interval is considered, proposing a plausible range of values for a deviation from the local maxima of the $P'(\beta, y)$ curve of 1%. This results in a smoothed curve represented by the yellow solid line, which varies along the guide vane opening in a range from $\beta = 0.7$ to 0.8 [pu]. Fig. D.2 also depicts the on-cam curve (orange line) and the iso-discharge curve (purple line) at a value of $Q = 190$ [m^3/s], discussed later. The experimental Flex-cam curve in both the preliminary and fitted form (red and yellow lines, respectively) and the analytical Flex-cam curve (blue line) are compared in Fig. D.3. The fitted experimental Flex-cam curve (yellow line) exhibits good agreement with the analytical Flex-cam curve (blue line). The graph in Fig. D.4 depicts the maximum flexibility curves for various levels of gross head, corresponding to those employed in the on-cam feature. The pitch blade β of the Flex-cam curves remains between 0.65 to 0.8. Based on this observation, it can be inferred that alterations in gross head do not significantly impact the flexibility.

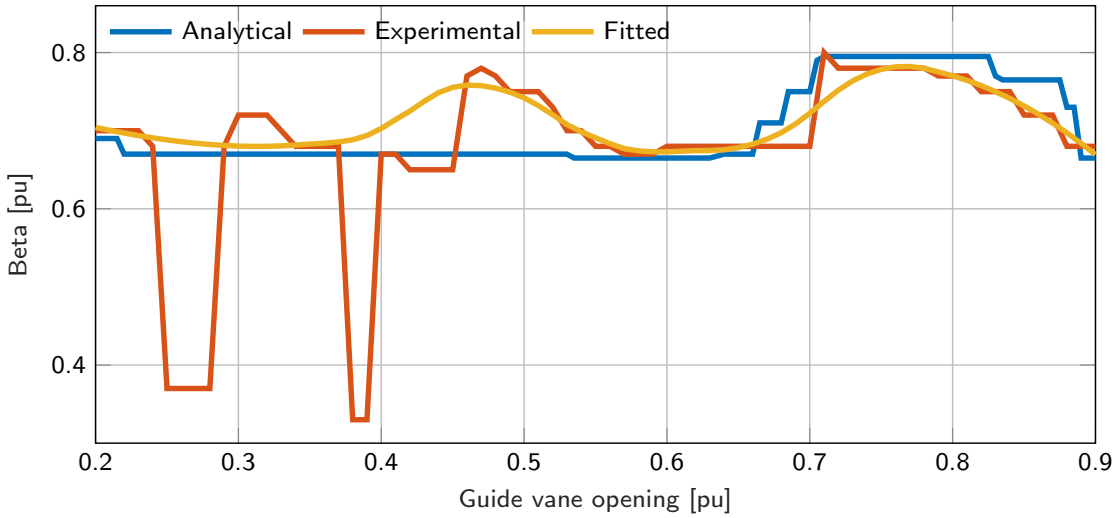

Figure D.3: Experimental and semi-analytical methods: Flex-cam curve comparison

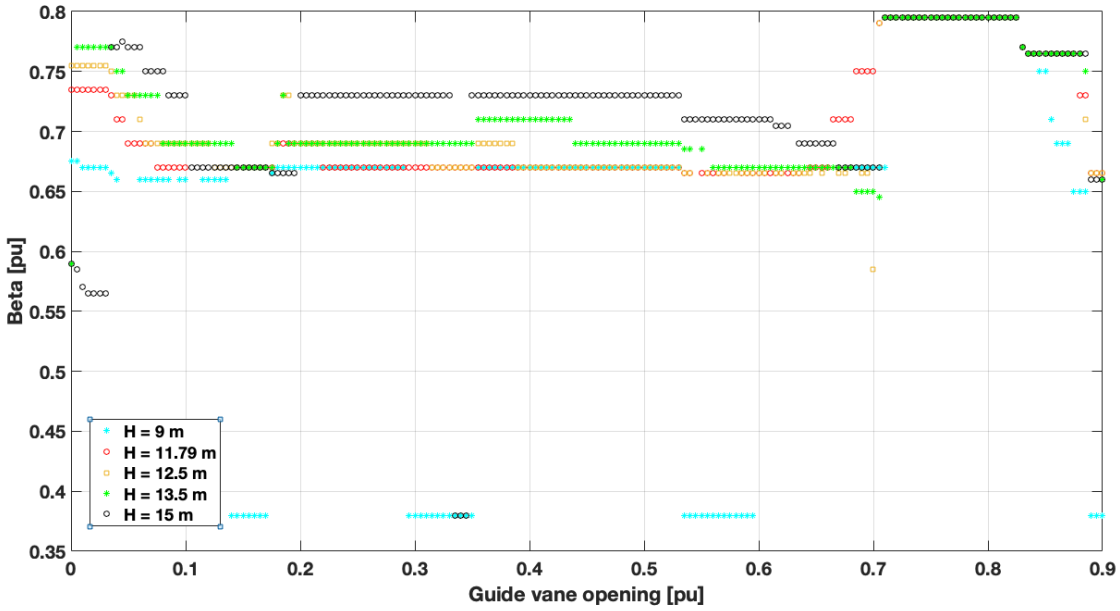

Figure D.4: Flex-cam curves under different gross heads H_g

D.3.2 Performance comparison between on-cam and flexible operations

We conduct a comparative analysis of the performance of an HPP when operated using the on-cam curve and the Flex-cam curve. The performance evaluation is based on the following metrics:

1. output power ramping time: this metric measures the percentage of ΔP delivered to the grid within a given time, in accordance with the plant's droop coefficient.

2. Discharge control action: this metric evaluates the plant's ability to maintain the water discharge as close as possible to the reference value.

3. Tracking of the frequency signal: this metric is evaluated using the correlation coefficients (CCs), which range from -1 to +1. A value of ±1 indicates the strongest possible agreement, while a value of 0 indicates the strongest possible disagreement.

4. Wear (mileage) evaluation of guide vanes and runner blades: this metric assesses the time integral of the absolute value of the position changes of the guide vanes and blade's pitch during operation.

The evaluation is conducted under two scenarios: the response of the plant to a step of the grid frequency, and primary frequency control with a real frequency signal.

Step response to a frequency deviation

We consider a frequency drop of $\Delta f = -200$ mHz from 50 Hz, and the governor's PID system adjusts the guide vanes to modulate the HPP's output power based on the permanent speed. Another requirement is to maintain the discharge at a constant value of $Q = 190$ [m^3/s].

The two initial operating conditions are determined by the intersection of the iso-discharge curve (purple line) with the on-cam (orange line) and Flex-cam (yellow line) characteristics, respectively, for the maximum efficiency and maximum flexibility working modes. The resulting values are $y = 0.726$ [pu] and $\beta = 0.5171$ [pu] for the efficiency mode, and $y = 0.486$ [pu] and $\beta = 0.7514$ [pu] for the flexibility mode, corresponding to efficiencies of 93% and 53.60%, respectively, for each mode. The performance comparison is presented in Figs. (D.5 - D.8).

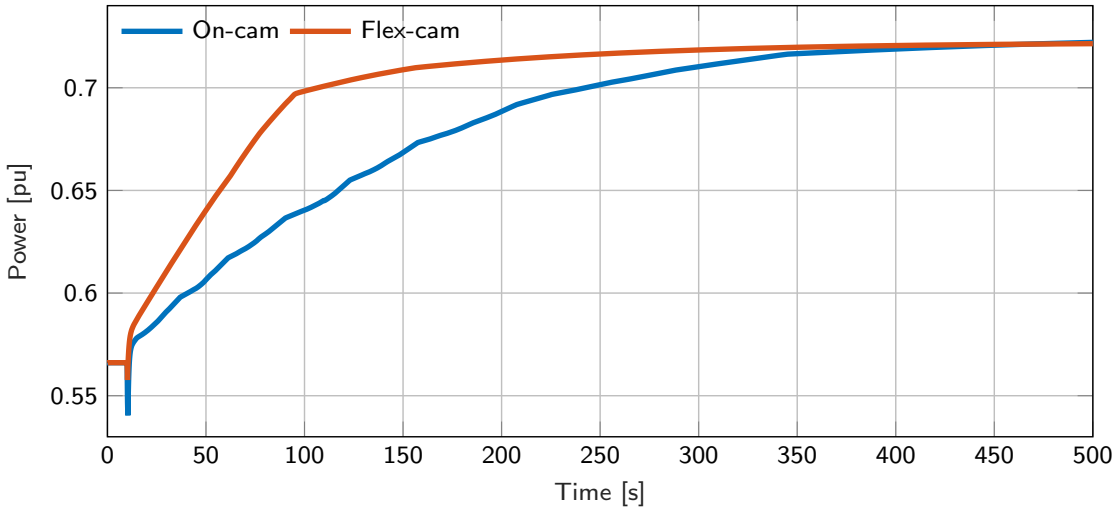

Figure D.5: HPP step response: output power resulting from a frequency drop of 200 mHz at t = 10s

In Fig. D.5, the power offset relative to the initial output power is illustrated by comparing the two output power curves. To highlight the different dynamic performance, the curves are translated. The output power from the flexibility working mode shows a larger response time, delivering 50% and 100% of the ΔP corresponding to the droop coefficient in a time of $t = 9$ and $t = 28$ [s], respectively, compared to $t = 22$ and $t = 62$ in the case of the maximum-efficiency mode.

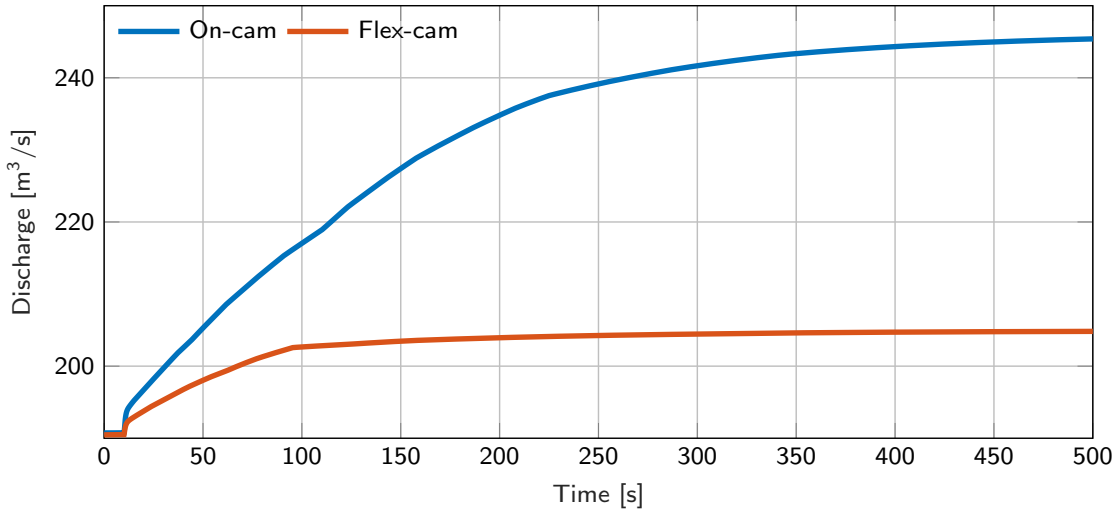

Figure D.6: HPP step response: discharge resulting from a frequency drop of 200 mHz at t = 10s

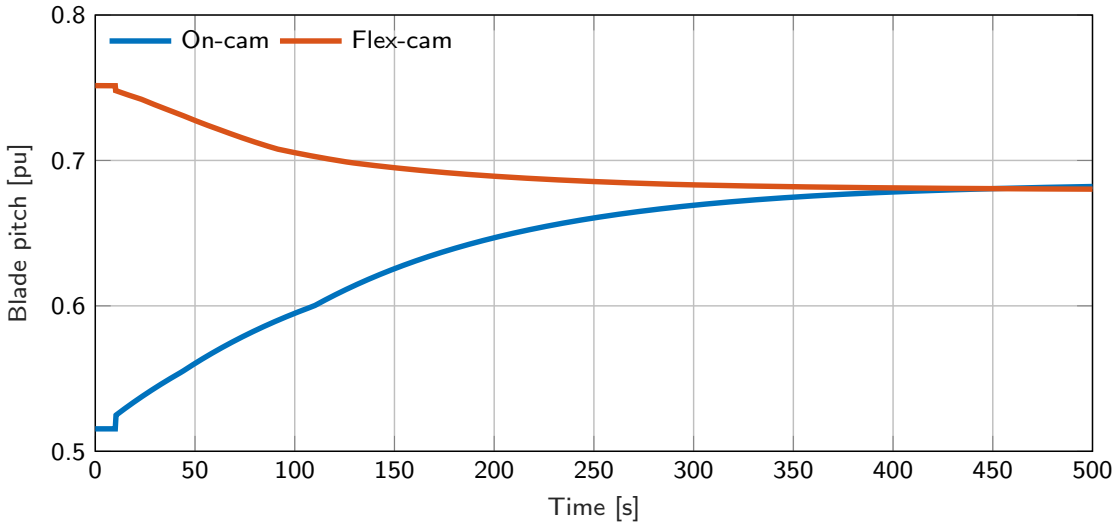

Figure D.7: HPP step response: blade pitch angle resulting from a frequency drop of 200 mHz at t = 10s

In terms of discharge control action, Fig. D.6 indicates better performance of the HPP in the flexibility mode, with a maximum deviation of 14 [m^3/s] compared to 55 [m^3/s] for the maximum-efficiency mode. However, this may seem to contradict the definition of flexibility since it was expected that a flexible working point would feature a higher rate of change of power, corresponding to a greater change of discharge. This issue will be addressed in the final section of the results. It should be noted that the change in β is very small, as depicted in Fig. D.7, and that we are leveraging on efficiency by lowering it.

The tracking of the frequency signal is evaluated through the correlation coefficients (CCs), with the values of the CCs and the mileage of the guide vane, as depicted in Fig. D.8, and the runner blade pitch shown in Table D.1.

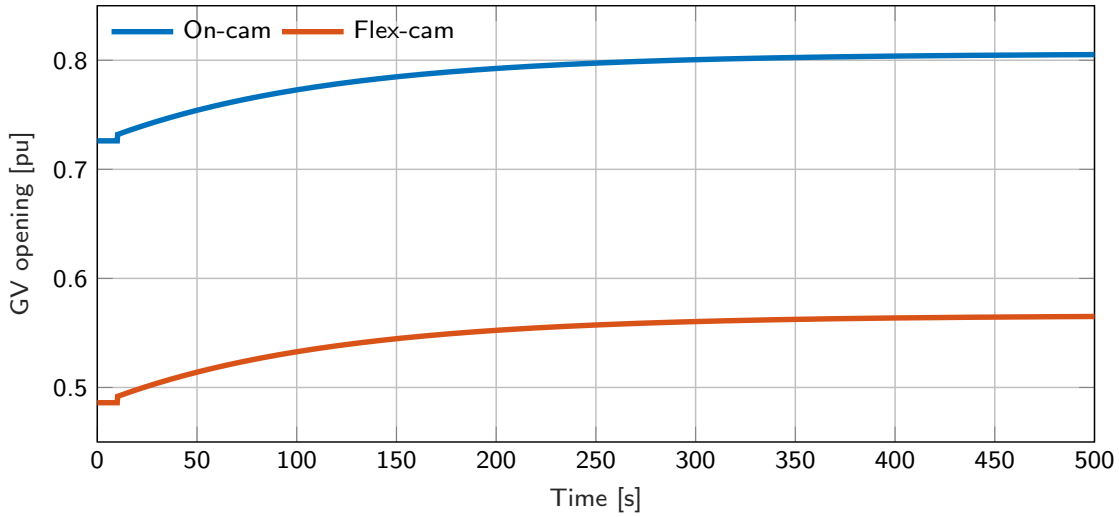

Figure D.8: HPP step response: guide vane opening resulting from a frequency drop of 200 mHz at t = 10s

Table D.1: Performance metric values (frequency step)

Metric	**Eff. mode value**	**Flex. mode value**
Frequency tracking CC	-0.6538	-0.7925
Mileage (wear) of y	0.1275	0.1275
Mileage (wear) of β	0.2827	0.1157

In terms of tracking the frequency signal, the flexibility mode exhibits better performance than the maximum-efficiency mode. Furthermore, the mileage of the guide vane is identical in both cases due to the same control action. However, a noteworthy finding is that the mileage of the runner blade pitch β is approximately 40% lower in the flexibility mode.

Primary frequency control

A similar analysis was carried out by employing a frequency signal measured during a day of operation from [80]. The findings regarding the output power response and discharge control action are consistent with those obtained previously. The tracking of the frequency signal and the wear are presented in Table D.2.

Table D.2: Performance metric values (PFR)

Metric	**Eff. mode value**	**Flex. mode value**
Frequency tracking CC	-0.6675	-0.7026
Mileage (wear) of y	0.6799	0.6799
Mileage (wear) of β	0.9400	0.3778

We can see that the flexibility mode still outperforms the maximum-efficiency mode in terms of tracking the frequency signal, although the difference is not as significant as in the first table. The mileage of the guide vane y is identical in both cases, but the mileage of the runner blade pitch β is significantly lower in the flexibility mode, approximately 60% lower. This suggests that the flexibility mode may be more efficient and cost-effective in terms of wear and tear on the equipment.

D.3.3 Where is the flexibility from?

This work demonstrates the existence of an operational mode, alternative to the classical mode at maximum efficiency, that provides superior response time while utilizing the same hardware components. To explain the reasons for the increased flexibility levels compared to conventional operation, it is convenient to examine the power output of the plant in terms of water kinetic energy:

$$P(\beta, y, t) = \rho \cdot g \cdot \eta(\beta, y, t) \cdot Q(\beta, y, t) \cdot H(\beta, y, t), \tag{D.7}$$

where ρ represents the water density in kilograms per cubic meter, and g is the acceleration due to gravity in meters per second squared. As the water head in the plant typically varies slowly and can be assumed to be constant, the time derivative of (D.7) is:

$$\begin{aligned} \frac{dP(\beta, y, t)}{dt} = \frac{d(\rho \cdot g \cdot \eta(\beta, y, t) \cdot Q(\beta, y, t) \cdot H)}{dt} = \\ c \cdot \eta(\beta, y, t) \cdot \frac{dQ(\beta, y, t)}{dt} + c \cdot Q(\beta, y, t) \cdot \frac{d\eta(\beta, y, t)}{dt}. \end{aligned} \tag{D.8}$$

Here, the constant coefficient c contains all the relevant constants. In Eq. (D.8), the discharge Q is directly derived from the $Q_{11}(\beta, y)$ characteristic curve. Thus, the time derivative of the discharge is derived by applying the chain rule to Q_{11} as:

$$\frac{dQ}{dt} \propto \frac{dQ_{11}(\beta, y)}{dt} = \frac{dQ_{11}}{d\beta}\frac{d\beta}{dt} + \frac{dQ_{11}}{dy}\frac{dy}{dt}, \tag{D.9}$$

leading to:

$$\frac{dQ}{dt} \propto r_\beta(t)\frac{dQ_{11}(\beta, y)}{d\beta} + r_y(t)\frac{dQ_{11}(\beta, y)}{dy}. \tag{D.10}$$

The efficiency is computed as:

$$\eta(\beta, y) = \frac{T(\beta, y) \cdot \omega}{\rho \cdot g \cdot \eta(\beta, y) \cdot Q(\beta, y) \cdot H}, \tag{D.11}$$

where the torque T is obtained by the $T_{11}(\beta, y)$ characteristic curve, as in Eq (D.4). At this point, the time derivative of the efficiency η is computed numerically.

Using Eqs. (D.9)-(D.11), we are able to evaluate both terms in Eq. (D.8). A comparison of these terms shows that the second term dominates. Therefore, it can be inferred that the plant's flexibility is mainly influenced by its efficiency, and consequently, better discharge control is achieved with fewer movements of the runner blade.

D.4 Conclusion

In this section, we have demonstrated an alternative operational mode for a run-of-river power plant with a Kaplan turbine, which involves operating at maximum flexibility rather than maximum efficiency. Additionally, we have proposed two methods for determining the relationship between guide vane opening and blade position to achieve maximum flexibility.

Through simulations on frequency deviation of 200 mHz and on PFR operations, we have observed that operating in flexibility mode instead of classical efficiency mode offers several advantages, including larger power dynamic response up to two times, better discharge control and water flow management, higher frequency signal tracking due to faster plant response, and a significant reduction in blade mileage of about 40%, which is a major cause of fatigue in the turbine's servomechanism.

It is important to note that Kaplan turbines are designed to operate in the region close to the maximum efficiency points, and off-cam operations may result in pressure transients due to vortex rope, cavitation, and vibration, which can strongly affect stable operation and the turbine's lifespan. Future research will explore the identification of these "forbidden zones" to evaluate the feasibility of the working points of the Flex-cam curve.

Bibliography

[1] E. Commission and D.-G. for Communication, *European green deal : delivering on our targets*. Publications Office, 2021. [Online]. Available: https://op.europa.eu/en/publication-detail/-/publication/762414e8-ee81-11eb-a71c-01aa75ed71a1

[2] E. Commission and D. G. for Communication, *REPowerEU Actions*. Publications Office of the European Union, 2022. [Online]. Available: https://op.europa.eu/en/publication-detail/-/publication/41efb4a6-d7ea-11ec-a95f-01aa75ed71a1

[3] E. Commission and Eurostat, *Shedding light on energy in the EU : a guided tour of energy statistics : 2022 edition*. Publications Office, 2022. [Online]. Available: https://ec.europa.eu/eurostat/cache/infographs/energy/bloc-3b.html

[4] J. Bertsch, C. Growitsch, S. Lorenczik, and S. Nagl, "Flexibility options in european electricity markets in high res-e scenarios—study on behalf of the international energy agency," *Cologne, Germany: Energiewirtschaftliches Institut an Der Universität Zu Köln (EWI)*, 2012.

[5] I. E. Agency, *Harnessing Variable Renewables*, 2011. [Online]. Available: https://www.oecd-ilibrary.org/content/publication/9789264111394-en

[6] EU-SysFlex Consortium, *EU-SysFlex*, 2017. [Online]. Available: https://eu-sysflex.com

[7] OSMOSE Consortium, *OSMOSE*, 2018. [Online]. Available: https://www.osmose-h2020.eu/

[8] IEA, *Hydropower Data Explorer*, 2021. [Online]. Available: https://www.iea.org/data-and-statistics/data-tools/hydropower-data-explorer

[9] Agence Internationale de l'Energie (AIE), *Hydropower Special Market Report*, 2021. [Online]. Available: https://www.oecd-ilibrary.org/content/publication/07a7bac8-en

[10] ENTSO-E, Ed., *"ENTSO-E Statistical Factsheet 2018"*, Brussels, 2019.

[11] R. R. Shrivastwa, A. Hably, B. Seddik, H. Mesnage, and R. Guillaume, "An overview of hybridization of power sources for ancillary service," 02 2020, pp. 536–541.

[12] Y. Luo, Z. Wang, J. Zhang, J. Zeng, J. Lin, and G. Wang, "Vibration and fatigue caused by pressure pulsations originating in the vaneless space for a kaplan turbine with high head," *Engineering Computations: Int J for Computer-Aided Engineering*, vol. 30, 03 2013.

[13] K. Yonezawa, "An experimental investigation of cavitation surge in draft tube of francis turbine," *IOP Conference Series: Earth and Environmental Science*, vol. 240, no. 2, p. 022066, mar 2019. [Online]. Available: https://dx.doi.org/10.1088/1755-1315/240/2/022066

[14] C. Trivedi, B. Gandhi, and C. J. Michel, "Effect of transients on francis turbine runner life: a review," *Journal of Hydraulic Research*, vol. 51, no. 2, pp. 121–132, 2013. [Online]. Available: https://doi.org/10.1080/00221686.2012.732971

[15] A. Adamkowski, "Case study: Lapino powerplant penstock failure," *Journal of Hydraulic Engineering-asce - J HYDRAUL ENG-ASCE*, vol. 127, 07 2001.

[16] M. Dreyer, C. Nicolet, A. Gaspoz, D. Biner, S. Rey-Mermet, C. Saillen, and B. Boulicaut, "Digital clone for penstock fatigue monitoring," in *IOP Conference Series: Earth and Environmental Science*, vol. 405, no. 1. IOP Publishing, 2019, p. 012013.

[17] XFLEX HYDRO Consortium, *XFLEX HYDRO*, 2019. [Online]. Available: https://xflexhydro.net/

[18] E. Bortoni, Z. d. Souza, A. Viana, H. Villa-Nova, Rezek, L. Pinto, R. Siniscalchi, R. Bragança, and J. Bernardes, "The benefits of variable speed operation in hydropower plants driven by francis turbines," *Energies*, vol. 12, no. 19, 2019. [Online]. Available: https://www.mdpi.com/1996-1073/12/19/3719

[19] M. Valavi and A. Nysveen, "Variable-speed operation of hydropower plants: A look at the past, present, and future," *IEEE Industry Applications Magazine*, vol. 24, no. 5, pp. 18–27, 2018.

[20] J. Hell, R. Schürhuber, Lechner, and Vaillant, "Full size converter solutions for pumped-storage plants: a promising new technology," in *Hydro 2012, Bilbao, Spain, 2012*, 2012.

[21] H. Schlunegger, "Pumping efficiency: A 100 mw converter for the grimsel 2 pumped storage plant," pp. 42–47, 01 2014.

[22] C. Nicolet, O. Braun, N. Ruchonnet, and A. Béguin, "Full size frequency converter for fast francis pump-turbine operating mode transition," 2016.

[23] Y. Pannatier, B. Kawkabani, C. Nicolet, J.-J. Simond, A. Schwery, and P. Allenbach, "Investigation of control strategies for variable-speed pump-turbine units by using a simplified model of the converters," *IEEE Transactions on Industrial Electronics*, vol. 57, no. 9, pp. 3039–3049, 2010.

[24] M. Camara, B. Dakyo, C. Nichita, and G. Barakat, "Simulation of a doubly-fed induction generator with hydro turbine for electrical energy production," in *2009 8th International Symposium on Advanced Electromechanical Motion Systems Electric Drives Joint Symposium*, 2009, pp. 1–6.

[25] E. Namor, F. Sossan, R. Cherkaoui, and M. Paolone, "Control of battery storage systems for the simultaneous provision of multiple services," *IEEE Transactions on Smart Grid*, vol. 10, no. 3, pp. 2799–2808, 2019.

[26] F. Sossan, E. Namor, R. Cherkaoui, and M. Paolone, "Achieving the dispatchability of distribution feeders through prosumers data driven forecasting and model predictive control of electrochemical storage," *IEEE Transactions on Sustainable Energy*, vol. 7, no. 4, pp. 1762–1777, 2016.

[27] D. Wu, C. Jin, P. Balducci, and M. Kintner-Meyer, "An energy storage assessment: Using optimal control strategies to capture multiple services," in *2015 IEEE Power Energy Society General Meeting*, 2015, pp. 1–5.

[28] M. Kazemi, H. Zareipour, N. Amjady, W. D. Rosehart, and M. Ehsan, "Operation scheduling of battery storage systems in joint energy and ancillary services markets," *IEEE Transactions on Sustainable Energy*, vol. 8, no. 4, pp. 1726–1735, 2017.

[29] B. Cheng and W. B. Powell, "Co-optimizing battery storage for the frequency regulation and energy arbitrage using multi-scale dynamic programming," *IEEE Transactions on Smart Grid*, vol. 9, no. 3, pp. 1997–2005, 2018.

[30] O. Mégel, J. L. Mathieu, and G. Andersson, "Scheduling distributed energy storage units to provide multiple services under forecast error," *International Journal of Electrical Power Energy Systems*, vol. 72, pp. 48–57, 2015, the Special Issue for 18th Power Systems Computation Conference. [Online]. Available: https://www.sciencedirect.com/science/article/pii/S0142061515000939

[31] Y. Shi, B. Xu, D. Wang, and B. Zhang, "Using battery storage for peak shaving and frequency regulation: Joint optimization for superlinear gains," *IEEE Transactions on Power Systems*, vol. 33, no. 3, pp. 2882–2894, 2018.

[32] F. Gerini, Y. Zuo, R. Gupta, A. Zecchino, Z. Yuan, E. Vagnoni, R. Cherkaoui, and M. Paolone, "Optimal grid-forming control of battery energy storage systems providing multiple services: Modeling and experimental validation," *Electric Power Systems Research*, vol. 212, p. 108567, 2022. [Online]. Available: https://www.sciencedirect.com/science/article/pii/S0378779622006496

[33] F. Soares, L. Carvalho, I. Costa, J. Iria, J.-M. Bodet, G. Jacinto, A. Lecocq, J. Roessner, B. Caillard, and O. Salvi, "The stabalid project: Risk analysis of stationary li-ion batteries for power system applications," *Reliability Engineering System Safety*, vol. 140, pp. 142–175, 2015. [Online]. Available: https://www.sciencedirect.com/science/article/pii/S0951832015001167

[34] B. Diouf and R. Pode, "Potential of lithium-ion batteries in renewable energy," *Renewable Energy*, vol. 76, pp. 375–380, 2015. [Online]. Available: https://www.sciencedirect.com/science/article/pii/S0960148114007885

[35] W. Yang, P. Norrlund, L. Saarinen, J. Yang, W. Guo, and W. Zeng, "Wear and tear on hydro power turbines – influence from primary frequency control," *Renewable Energy*, vol. 87, pp. 88–95, 2016. [Online]. Available: https://www.sciencedirect.com/science/article/pii/S0960148115303621

[36] M. Dreyer, C. Nicolet, A. Gaspoz, N. Gonçalves, S. Rey-Mermet, and B. Boulicaut, "Monitoring 4.0 of penstocks: digital twin for fatigue assessment," *IOP Conference Series: Earth and Environmental Science*, vol. 774, no. 1, p. 012009, jun 2021. [Online]. Available: https://doi.org/10.1088/1755-1315/774/1/012009

[37] S. Cassano and F. Sossan, "Stress-informed control of medium- and high-head hydropower plants to reduce penstock fatigue," *Sustainable Energy, Grids and Networks*, vol. 31, p. 100688, 2022. [Online]. Available: https://www.sciencedirect.com/science/article/pii/S2352467722000443

[38] M. Zhang, D. Valentín, C. Valero, M. Egusquiza, and E. Egusquiza, "Failure investigation of a kaplan turbine blade," *Engineering Failure Analysis*, vol. 97, pp. 690–700, 2019. [Online]. Available: https://www.sciencedirect.com/science/article/pii/S1350630718309191

[39] Y. Luo, Z. Wang, J. Zeng, and J. Lin, "Fatigue of piston rod caused by unsteady, unbalanced, unsynchronized blade torques in a kaplan turbine," *Engineering Failure Analysis*, vol. 17, no. 1, pp. 192–199, 2010, papers presented at the 25th meeting of the Spanish Fracture Group. [Online]. Available: https://www.sciencedirect.com/science/article/pii/S1350630709001472

[40] P. Kundur and N. Balu, *Power System Stability and Control*, ser. EPRI power system engineering series. McGraw-Hill, 1994.

[41] M. Scherer, D. Schlipf, and W. Sattinger, "Test for primary control capability—version 1.1," *Swissgrid Ltd.: Aarau, Switzerland*, 2011.

[42] D. C. Maxime Zeller, "Flexibility within the electrical systems through demand side response by electrolysers: Testing protocols for balancing products in germany, france, and the uk." [Online]. Available: https://ec.europa.eu/research/participants/documents/downloadPublic?documentIds=080166e5b2c00111&appId=PPGMS

[43] T. Mäkinen, A. Leinonen, and M. Ovaskainen, "Modelling and benefits of combined operation of hydropower unit and battery energy storage system on grid primary frequency control," in *2020 IEEE International Conference on Environment and Electrical Engineering and 2020 IEEE Industrial and Commercial Power Systems Europe (EEEIC / ICPS Europe)*, 2020, pp. 1–6.

[44] R. Gawarkiewicz and M. Wasilczuk, "Wear measurements of self-lubricating bearing materials in small oscillatory movement," *Wear*, vol. 263, no. 1, pp. 458–462, 2007, 16th International Conference on Wear of Materials. [Online]. Available: https://www.sciencedirect.com/science/article/pii/S0043164807004231

[45] P.-T. Storli and T. K. Nielsen, "Dynamic load on a francis turbine runner from simulations based on measurements," *IOP Conference Series: Earth and Environmental Science*, vol. 22, no. 3, p. 032056, mar 2014. [Online]. Available: https://doi.org/10.1088/1755-1315/22/3/032056

[46] M. Zhang, D. Valentín, C. Valero, M. Egusquiza, and E. Egusquiza, "Failure investigation of a kaplan turbine blade," *Engineering Failure Analysis*, vol. 97, pp. 690–700, 2019. [Online]. Available: https://www.sciencedirect.com/science/article/pii/S1350630718309191

[47] S. Cassano and F. Sossan, "Stress-informed control of medium- and high-head hydropower plants to reduce penstock fatigue," *Sustainable Energy, Grids and Networks*, vol. 31, p. 100688, 2022.

[48] S. Cassano, C. Nicolet, and F. Sossan, "Reduction of penstock fatigue in a medium-head hydropower plant providing primary frequency control," in *2020 55th UPEC*, 2020.

[49] C. Nicolet, R. Berthod, N. Ruchonnet, and F. Avellan, "Evaluation of possible penstock fatigue resulting from secondary control for the grid," *Proceedings of HYDRO*, 2010.

[50] "Ieee guide for the application of turbine governing systems for hydroelectric generating units - redline," *IEEE Std 1207-2011 (Revision to IEEE Std 1207-2004) - Redline*, pp. 1–139, 2011.

[51] H. An, J. Yang, W. Yang, Y. Cheng, and Y. Peng, "An improved frequency dead zone with feed-forward control for hydropower units: Performance evaluation of primary frequency control," *Energies*, vol. 12, no. 8, 2019. [Online]. Available: https://www.mdpi.com/1996-1073/12/8/1497

[52] W. Yang, P. Norrlund, L. Saarinen, J. Yang, W. Zeng, and U. Lundin, "Wear reduction for hydropower turbines considering frequency quality of power systems: A study on controller filters," *IEEE Transactions on Power Systems*, vol. 32, no. 2, pp. 1191–1201, 2017.

[53] S. Gupta, *Fluid Mechanics and Hydraulic Machines*. Pearson India, 2006. [Online]. Available: https://books.google.fr/books?id=kIlLzQEACAAJ

[54] C. Nicolet, "Hydroacoustic modelling and numerical simulation of unsteady operation of hydroelectric systems," Ph.D. dissertation, EPFL, Lausanne, 2007. [Online]. Available: http://infoscience.epfl.ch/record/98534

[55] A. Sapin, "Logiciel modulaire pour la simulation et l'étude des systèmes d'entraînement et des réseaux électriques," 1995.

[56] W. Zhou, "Modeling, control and optimization of a hydropower plant," 2017.

[57] U. Bolleter, E. Buehlmann, J. Eberl, and A. Stirnemann, "Hydraulic and mechanical interactions of feedpump systems. final report," Electric Power Research Inst., Palo Alto, CA (United States), Tech. Rep., 1992.

[58] L. C. Evans, *Partial differential equations*, ser. Graduate studies in mathematics. Providence, R.I: American Mathematical Society, 1998, no. v. 19.

[59] S. Sarra, "The method of characteristics with applications to conservation laws," *Journal of Online Mathematics and Applications*, vol. 3, 02 2003.

[60] E. Wylie, V. Streeter, and L. Suo, *Fluid Transients in Systems*. Prentice Hall, 1993.

[61] W. G. P. Mover and E. Supply, "Hydraulic turbine and turbine control models for system dynamic studies," *IEEE Transactions on Power Systems*, vol. 7, no. 1, pp. 167–179, 1992.

[62] H. Lewy, K. Friedrichs, and R. Courant, "Über die partiellen differenzengleichungen der mathematischen physik," *Mathematische Annalen*, vol. 100, pp. 32–74, 1928. [Online]. Available: http://eudml.org/doc/159283

[63] R. Knapp, "Complete characteristics . of centrifugal the prediction pumps and their use in of transient behavior," 2014.

[64] H. Mesnage, M. Alamir, N. Perrissin-Fabert, Q. Alloin, and B. Seddik, "Hydraulic-turbine start-up with "s-shaped" characteristic," 07 2015, pp. 2328–2333.

[65] M. MARCHAL, "The calculation of waterhammer problems by means of the digital computer," *Proc. Intern. Symp. Waterhammer Pumped Storage Projects ASME, 1965-11*, 1965. [Online]. Available: https://ci.nii.ac.jp/naid/10018994265/en/

[66] S. Cassano, F. Sossan, C. Landry, and C. Nicolet, "Performance assessment of linear models of hydropower plants," in *2021 IEEE PES Innovative Smart Grid Technologies Europe (ISGT Europe)*, 2021.

[67] H. Cerjak, O. Chene, N. Enzinger, and E. Roos, "Qualification program for the rehabilitation of cleuson-dixence: Requirements and results," 05 2005.

[68] A. Tijsseling and A. Anderson, "The joukowsky equation for fluids and solids," *Journal of Scientific Computing*, 01 2006.

[69] A. Papangelo, R. Guarino, N. Pugno, and M. Ciavarella, "On unified crack propagation laws," *Engineering Fracture Mechanics*, vol. 207, 02 2019.

[70] E. Santecchia, A. M. S. Hamouda, F. Musharavati, E. Zalnezhad, M. Cabibbo, M. El Mehtedi, and S. Spigarelli, "A review on fatigue life prediction methods for metals," *Advances in Materials Science and Engineering*, vol. 2016, p. 9573524, Sep 2016. [Online]. Available: https://doi.org/10.1155/2016/9573524

[71] R. K. Holman and P. K. Liaw, "Methodologies for predicting fatigue life," *JOM*, vol. 49, no. 7, pp. 46–52, Jul 1997. [Online]. Available: https://doi.org/10.1007/BF02914767

[72] L. Cui, I. Frenkel, A. Lisnianski, *Stochastic Models in Reliability Engineering (1st ed.)*. CRC Press, 2020.

[73] F. McBagonluri and W. Soboyejo, "Mechanical properties: Fatigue," in *Encyclopedia of Condensed Matter Physics*, F. Bassani, G. L. Liedl, and P. Wyder, Eds. Oxford: Elsevier, 2005.

[74] A. Adamkowski, M. Lewandowski, and S. Lewandowski, "Fatigue life analysis of hydropower pipelines using the analytical model of stress concentration in welded joints with angular distortions and considering the influence of water hammer damping," *Thin-Walled Structures*, vol. 159, 12 2020.

[75] A. Tijsseling and A. Anderson, "The joukowsky equation for fluids and solids," *Journal of Scientific Computing*, 01 2006.

[76] A. International, "ASTM E1049-85(2005), Standard Practices for Cycle Counting in Fatigue Analysis," Internet Requests for Comments, ASTM International, West Conshohocken, PA,, RFC 1654, 2005. [Online]. Available: http://www.astm.org/cgi-bin/resolver.cgi?E1049

[77] A. Niesłony, "Determination of fragments of multiaxial service loading strongly influencing the fatigue of machine components," *Mechanical Systems and Signal Processing*, vol. 23, no. 8, pp. 2712–2721, Nov. 2009.

[78] Y.-L. Lee and H.-T. Kang, "Chapter 9 - vibration fatigue testing and analysis," in *Metal Fatigue Analysis Handbook*, Y.-L. Lee, M. E. Barkey, and H.-T. Kang, Eds. Boston: Butterworth-Heinemann, 2012, pp. 333–382. [Online]. Available: https://www.sciencedirect.com/science/article/pii/B9780123852045000094

[79] I. Hadley, "Bs 7910:2013 in brief," *International Journal of Pressure Vessels and Piping*, vol. 165, pp. 263 – 269, 2018. [Online]. Available: http://www.sciencedirect.com/science/article/pii/S0308016118302102

[80] M. Pignati, M. Popovic, S. Barreto Andrade, R. Cherkaoui, D. Flores, J.-Y. Le Boudec, M. M. Maaz, M. Paolone, P. Romano, S. Sarri, T. T. Tesfay, D.-C. Tomozei, and L. Zanni, "Real-Time State Estimation of the EPFL-Campus Medium-Voltage Grid by Using PMUs," in *The Sixth Conference on Innovative Smart Grid Technologies (ISGT2015)*, 2014.

[81] K. Pearson, "Note on Regression and Inheritance in the Case of Two Parents," *Proceedings of the Royal Society of London Series I*, vol. 58, pp. 240–242, Jan. 1895.

[82] A. Zecchino, Z. Yuan, F. Sossan, R. Cherkaoui, and M. Paolone, "Optimal provision of concurrent primary frequency and local voltage control from a BESS considering variable capability curves: Modelling and experimental assessment," *Electric Power Systems Research*, vol. 190, p. 106643, 2021.

[83] C. Nicolet, M. Dreyer, A. Beguin, E. Bollaert, S. Torrent, and J. Dayer, "Hydraulic transient survey at cleuson-dixence with real-time hydro-clone monitoring system," in *Proc. of HYDRO 2018 Conference*, 2018.

[84] B. Zine, H. Bia, A. Benmouna, M. Becherif, and M. Iqbal, "Experimentally validated coulomb counting method for battery state-of-charge estimation under variable current profiles," *Energies*, vol. 15, no. 21, 2022. [Online]. Available: https://www.mdpi.com/1996-1073/15/21/8172

[85] A. Nugroho, E. Rijanto, F. D. Wijaya, and P. Nugroho, "Battery state of charge estimation by using a combination of coulomb counting and dynamic model with adjusted gain," in *2015 International Conference on Sustainable Energy Engineering and Application (ICSEEA)*, 2015, pp. 54–58.

[86] M.-K. Tran, M. Mathew, S. Janhunen, S. Panchal, K. Raahemifar, R. Fraser, and M. Fowler, "A comprehensive equivalent circuit model for lithium-ion batteries, incorporating the effects of state of health, state of charge, and temperature on model parameters," *Journal of Energy Storage*, vol. 43, p. 103252, 2021. [Online]. Available: https://www.sciencedirect.com/science/article/pii/S2352152X2100949X

[87] S. S. Madani, E. Schaltz, and S. Knudsen Kær, "An electrical equivalent circuit model of a lithium titanate oxide battery," *Batteries*, vol. 5, no. 1, 2019. [Online]. Available: https://www.mdpi.com/2313-0105/5/1/31

[88] D. U. Sauer, P. Birke, M. Keller, O. Bohlen, and J. B. Gerschler, "Robust algorithms for a reliable battery diagnosis : managing batteries in hybrid electric vehicles," in *Moving to sustainable mobility : EVS 22, the 22nd International Battery, Hybrid and Fuel Cell Electric Vehicle Symposium and Exposition ; proceedings, October 23 - 28, 2006, Yokohama, Japan / Japan Automobile Research Institute*. Tokyo: Japan Automobile Research Institute, 2006, 1 CD-ROM. [Online]. Available: https://publications.rwth-aachen.de/record/112626

[89] X. Liu, Y. Yang, G. Wang, Y. Li, and W. Ma, "Method for estimating the maximum output of a battery for a hybrid electric vehicle," Patent CN101 133 514B, Dec 16, 2009. [Online]. Available: https://patents.google.com/patent/CN101133514B/en

[90] J. P. Christophersen, "Battery test manual for electric vehicles, revision 3." [Online]. Available: https://www.osti.gov/biblio/1186745

[91] G. Plett, "High-performance battery-pack power estimation using a dynamic cell model," *IEEE Transactions on Vehicular Technology*, vol. 53, no. 5, pp. 1586–1593, 2004.

[92] C. Burgos-Mellado, M. E. Orchard, M. Kazerani, R. Cárdenas, and D. Sáez, "Particle-filtering-based estimation of maximum available power state in lithium-ion batteries," *Applied Energy*, vol. 161, pp. 349–363, 2016. [Online]. Available: https://www.sciencedirect.com/science/article/pii/S0306261915012180

[93] P. Malysz, J. Ye, R. Gu, H. Yang, and A. Emadi, "Battery state-of-power peak current calculation and verification using an asymmetric parameter equivalent circuit model," *IEEE Transactions on Vehicular Technology*, vol. 65, no. 6, pp. 4512–4522, 2016.

[94] W. Zhang, W. Shi, and Z. Ma, "Adaptive unscented kalman filter based state of energy and power capability estimation approach for lithium-ion battery," *Journal of Power Sources*, vol. 289, pp. 50–62, 2015. [Online]. Available: https://www.sciencedirect.com/science/article/pii/S0378775315008162

[95] X. Hu, R. Xiong, and B. Egardt, "Model-based dynamic power assessment of lithium-ion batteries considering different operating conditions," *IEEE Transactions on Industrial Informatics*, vol. 10, no. 3, pp. 1948–1959, 2014.

[96] F. Sun, R. Xiong, H. He, W. Li, and J. E. E. Aussems, "Model-based dynamic multi-parameter method for peak power estimation of lithium–ion batteries," *Applied Energy*, vol. 96, pp. 378–386, 2012, smart Grids. [Online]. Available: https://www.sciencedirect.com/science/article/pii/S0306261912001626

[97] M. Bahramipanah, D. Torregrossa, R. Cherkaoui, and M. Paolone, "Enhanced equivalent electrical circuit model of lithium-based batteries accounting for charge redistribution, state-of-health, and temperature effects," *IEEE Transactions on Transportation Electrification*, vol. 3, no. 3, pp. 589–599, 2017.

[98] R. D. Anderson, Y. Zhao, X. Wang, X. G. Yang, and Y. Li, "Real time battery power capability estimation," in *2012 American Control Conference (ACC)*, 2012, pp. 592–597.

[99] M. Bahramipanah, D. Torregrossa, R. Cherkaoui, and M. Paolone, "An adaptive model-based real-time voltage control process for active distribution networks using battery energy storage systems," in *2016 Power Systems Computation Conference (PSCC)*, 2016, pp. 1–8.

[100] B. Jiang, H. Dai, X. Wei, L. Zhu, and Z. Sun, "Online reliable peak charge/discharge power estimation of series-connected lithium-ion battery packs," *Energies*, vol. 10, no. 3, 2017. [Online]. Available: https://www.mdpi.com/1996-1073/10/3/390

[101] B. V. Rajanna and M. Kumar, "Comparison of one and two time constant models for lithium ion battery," *International Journal of Electrical and Computer Engineering*, vol. 10, pp. 670–680, 02 2020.

[102] S. Cassano and F. Sossan, "Model predictive control for a medium-head hydropower plant hybridized with battery energy storage to reduce penstock fatigue," *Electric Power Systems Research*, vol. 213, p. 108545, 2022. [Online]. Available: https://www.sciencedirect.com/science/article/pii/S0378779622006484

[103] E. Maleki, S. Bagherifard, S. Razavi, M. Bandini, A. du Plessis, F. Berto, and M. Guagliano, "On the efficiency of machine learning for fatigue assessment of post-processed additively manufactured alsi10mg," *International Journal of Fatigue*, vol. 160, p. 106841, 2022. [Online]. Available: https://www.sciencedirect.com/science/article/pii/S0142112322001165

[104] C. Gobert, E. W. Reutzel, J. Petrich, A. R. Nassar, and S. Phoha, "Application of supervised machine learning for defect detection during metallic powder bed fusion

additive manufacturing using high resolution imaging." *Additive Manufacturing*, vol. 21, pp. 517–528, 2018. [Online]. Available: https://www.sciencedirect.com/science/article/pii/S2214860417302051

[105] Z. Sedighi Maman, M. A. Alamdar Yazdi, L. A. Cavuoto, and F. M. Megahed, "A data-driven approach to modeling physical fatigue in the workplace using wearable sensors," *Applied Ergonomics*, vol. 65, pp. 515–529, 2017. [Online]. Available: https://www.sciencedirect.com/science/article/pii/S0003687017300261

[106] N. H. Paulson, M. W. Priddy, D. L. McDowell, and S. R. Kalidindi, "Data-driven reduced-order models for rank-ordering the high cycle fatigue performance of polycrystalline microstructures," *Materials Design*, vol. 154, pp. 170–183, 2018. [Online]. Available: https://www.sciencedirect.com/science/article/pii/S0264127518303861

[107] D. Ozturk, S. Kotha, A. L. Pilchak, and S. Ghosh, "Two-way multi-scaling for predicting fatigue crack nucleation in titanium alloys using parametrically homogenized constitutive models," *Journal of the Mechanics and Physics of Solids*, vol. 128, pp. 181–207, 2019. [Online]. Available: https://www.sciencedirect.com/science/article/pii/S0022509618310512

[108] B. Sun, Y.-L. Xu, and Z. Li, "Multi-scale fatigue model and image-based simulation of collective short cracks evolution process," *Computational Materials Science*, vol. 117, pp. 24–32, 2016. [Online]. Available: https://www.sciencedirect.com/science/article/pii/S0927025616000355

[109] X. Hu, S. Li, and H. Peng, "A comparative study of equivalent circuit models for li-ion batteries," *Journal of Power Sources*, vol. 198, pp. 359–367, 2012. [Online]. Available: https://www.sciencedirect.com/science/article/pii/S0378775311019628

[110] H. He, R. Xiong, and J. Fan, "Evaluation of lithium-ion battery equivalent circuit models for state of charge estimation by an experimental approach," *Energies*, vol. 4, no. 4, pp. 582–598, 2011. [Online]. Available: https://www.mdpi.com/1996-1073/4/4/582

[111] H. He, R. Xiong, X. Zhang, F. Sun, and J. Fan, "State-of-charge estimation of the lithium-ion battery using an adaptive extended kalman filter based on an improved thevenin model," *IEEE Transactions on Vehicular Technology*, vol. 60, no. 4, pp. 1461–1469, 2011.

[112] D. Di Domenico, A. Stefanopoulou, and G. Fiengo, "Lithium-ion battery state of charge and critical surface charge estimation using an electrochemical model-based extended kalman filter," *Journal of Dynamic Systems, Measurement, and Control*, vol. 132, no. 6, Oct 2010, 061302. [Online]. Available: https://doi.org/10.1115/1.4002475

[113] Q.-K. Wang, Y.-J. He, J.-N. Shen, X.-S. Hu, and Z.-F. Ma, "State of charge-dependent polynomial equivalent circuit modeling for electrochemical impedance spectroscopy of lithium-ion batteries," *IEEE Transactions on Power Electronics*, vol. 33, no. 10, pp. 8449–8460, 2018.

[114] C. Li, N. Cui, C. Wang, and C. Zhang, "Reduced-order electrochemical model for lithium-ion battery with domain decomposition and polynomial approximation methods," *Energy*, vol. 221, p. 119662, 2021. [Online]. Available: https://www.sciencedirect.com/science/article/pii/S0360544220327699

[115] Y. Shi, B. Xu, Y. Tan, and B. Zhang, "A convex cycle-based degradation model for battery energy storage planning and operation," in *2018 Annual American Control Conference (ACC)*, 2018, pp. 4590–4596.

[116] C. Nicolet, P. Allenbach, J.-J. Simond, and F. Avellan, "Modeling and numerical simulation of a complete hydroelectric production site," in *2007 IEEE Lausanne Power Tech*, 2007, pp. 1044–1048.

[117] C. Nicolet, A. Sapin, J.-J. Simond, J.-E. Prenat, and F. Avellan, "A new tool for the simulation of dynamic behaviour of hydroelectric power plants," 01 2001.

[118] E. De Jaeger, N. Janssens, B. Malfliet, and F. Van De Meulebroeke, "Hydro turbine model for system dynamic studies," *IEEE Transactions on Power Systems*, vol. 9, no. 4, pp. 1709–1715, 1994.

RÉSUMÉ

La transition de la génération conventionnelle vers les ressources renouvelables pose des défis au réseau électrique. La mise hors service des unités de génération conventionnelle nécessite l'identification de nouvelles ressources flexibles pour les services de régulation. En France, les centrales hydroélectriques (HPP) sont essentielles pour produire de l'électricité et fournir des services critiques au réseau. Cependant, une augmentation des niveaux de régulation due à la génération renouvelable peut entraîner des coûts de maintenance plus élevés en raison de l'usure accrue. La proposition consiste à hybrider les HPP avec des systèmes de stockage d'énergie par batteries (BESS) pour accroître leur flexibilité et réduire l'usure des composants hydrauliques. Un défi majeur est de déterminer la stratégie optimale de répartition des points de consigne entre la HPP et la batterie.

Cette thèse de doctorat propose une méthodologie formelle pour contrôler les HPP hybrides, en tenant compte explicitement de la contrainte mécanique et de la réduction de la fatigue. La méthodologie comprend des couches de contrôle en temps réel et de planification, en utilisant des modèles linéarisés traitables des HPP. L'accent est mis sur la réduction de la fatigue des conduites forcées (penstock) dans les HPP à moyenne et haute chute, mais la méthodologie peut être étendue à d'autres types de HPP et d'unités de génération conventionnelles.

MOTS CLÉS

Centrales hydroélectriques hybrides, Système de stockage d'énergie par batteries, Optimisation, Réduction de la fatigue, Model predictive control, Modélisation des centrales hydroélectriques, Penstock

ABSTRACT

The shift from conventional generation to renewable resources challenges the electric power grid. Decommissioning conventional generation units requires identifying new flexible assets for balancing the grid and providing ancillary services. Hydropower Plants (HPPs) are important sources of electricity production and supply critical ancillary services to the grids. However, increased regulation duties to balance the intermittency of renewables (e.g., frequency control and start-stop sequences) may lead to higher wear-and-tear and maintenance costs. Hybridizing HPPs with Battery Energy Storage Systems (BESSs) has been proposed as a possible solution to increase the plants' flexibility and reduce the wear-and-tear of the hydraulic components. A key challenge of operating a hybrid HPP is to design the power set-points for the hydraulic turbine and the BESS (i.e., the power set-point splitting problem). This Ph.D. thesis proposes a formal methodology based on Model Predictive Control (MPC) for controlling hybrid HPPs that models the mechanical stress on the hydraulic components with the objective of accounting for fatigue constraints in the power set-point splitting problem explicitly. The proposed methodology includes a real-time control and a scheduling layer. In order to derive a tractable formulation of the optimization problem underlying the MPC, this thesis also develops linearized models of HPPs. The application of the proposed methodology refers to reducing penstock fatigue in medium- and high-head HPPs and can be extended to other types of HPPs and conventional generation units.

KEYWORDS

Hybrid hydropower plants, Battery Energy Storage System, Optimisation, Fatigue reduction, Model predictive control, Hydropower plant's modelling, Penstock